Confronting realistic MHD simulations of solar eruptions with observed space based data

A Thesis

Submitted for the Degree of

Doctor of Philosophy

in the Faculty of Science

by

Samriddhi Sankar Maity

Department of Physics
Indian Institute of Science
Bangalore – 560 012, INDIA

July 2024

Declaration

I hereby declare that the work reported in this doctoral thesis titled "Confronting Realistic MHD Simulations of Solar Eruptions with Observed Space-Based Data" is entirely original and is the result of investigations carried out by me at the Indian Institute of Astrophysics (IIA) and the Department of Physics, Indian Institute of Science (IISc), Bangalore, under the supervision of Dr. Piyali Chatterjee, Associate Professor, IIA as part of the Joint Astronomy Programme.

I further declare that this work has not formed the basis for the award of any degree, diploma, fellowship, associateship, or similar title of any University or Institution.

Date: July 30, 2024
Place: Bangalore, India

Samriddhi Sankar Maity
Department of Physics
Indian Institute of Science

To my family and mentors

whose unwavering support and encouragement have made this journey possible.

Acknowledgements

The journey of pursuing a PhD has been a transformative experience, marked by moments of results, challenge, and growth. This achievement is not mine alone; it is the culmination of the support, guidance, and encouragement from numerous individuals and institutions. Here is a token of appreciation to them for making this journey memorable.

First and foremost, I would like to express my deepest gratitude to my Ph.D. supervisor, Dr. Piyali Chatterjee, whose wisdom, patience, dedication and unwavering support have been the cornerstone of this research. She always encourages me to think outside the box, constantly pushing for new ideas. She doesn't believe in academic hierarchy and insisted from day one that I call her Piyali-di. Despite her numerous academic and administrative commitments, she is always helpful and consistently finds time to support me. She dedicated an immense amount of time to help me learn everything from the ground up and discuss different aspects of the ongoing and future project. Her willingness to patiently answer my questions and offer crucial insights for solving problem is truly commendable. Her tremendous motivation, work ethic, multi-tasking abilities, and diligent mindset are always evident. I am influenced by her these remarkable qualities. Your insightful feedback and constant encouragement have guided me through the complexities of my research.

I am also profoundly grateful to the co-supervisor Dr. Dipankar Banerjee and nominal supervisor Dr. Rajeev Kumar Jain. They have been incredibly helpful, often guiding me on who to approach for specific expertise and sometimes making the contact themselves. Dr. Jain even offered me his own computational grant when I was under pressure to secure a spot in the job submission queue. Your valuable suggestions and constant source of motivation have greatly improved the quality of my work.

I would like to express my heartfelt gratitude to my collaborators Dr. Nandita Srivastava and Dr. Ranadeep Sarkar, for their unwavering support and invaluable contributions. They always found time for me, helping whenever I needed it without hesitation. Despite being in a different time zone, Dr. Sarkar always demonstrated exceptional commitment, often providing help with analyzing events and manuscript preparation late into the night. Sometimes, he would help me analyze events during his vacation when I faced difficulties was truly commendable. Their dedication and willingness to support me have been instrumental in my journey.

I extend my heartfelt gratitude to the esteemed faculty members of IIA and IISc, including BGS-IIA, Dean-IIA, Director-IIA, Chairman of the Physics Department, DCC Chair, Arnab sir, Nirupam da, Prateek, Chanda ma'am, Tarun sir, Ravindra, Nagaraju, Wageesh, Jayant and Tanmoy da. I also wish to thank Bani-da, Rajaguru, Sampoorna and Nagendra sir for their pivotal role in shaping my foundational knowledge in astrophysics.

I would like to express my sincere appreciation to the distinguished faculty members of IIA and IISc who have played crucial roles in my academic journey. This includes the leadership at IIA - the BGS, Dean, and Director, as well as the Chairman of the Physics Department and the DCC Chair of IISc. I'm particularly grateful to Arnab sir, Nirupam da, Prateek, Chanda ma'am, Tarun sir, Ravindra, Nagaraju, Wageesh, Jayant, and Tanmoy da, Bani da, Sampoorna, Nagendra Sir and Prantika di for their guidance and support. Their expertise and teaching have been invaluable in shaping my understanding of the field. The collective wisdom, mentorship, and support from these esteemed individuals have significantly enriched my academic experience and contributed greatly to my growth as a researcher.

I am also thankful to the IUSSTF group members for their constructive support during my presentations. Special thanks to Dr. Nat Gopalswamy (NASA), Dr. Nikolai Pogorelov (UAH), Dr. Yashiro Seiji (NASA, CUA), and Prasad Subramanian (IISER-Pune). Additionally, I appreciate the support from the pencil-code group members: Axel (Nordita), Phillipe (IGAM), Fredrick (Aalto), Matthias (Aalto), Simon (Univ of Stuttgart), Warnecke (MPS), and Jennifer (EPFL).

A special vote of thanks goes to all the office members, particularly Shankar sir and Vijayalakshmi ma'am from IIA, and Sumithra ma'am and Meena ma'am from the Physics Department at IISc. I also extend my gratitude to Anish and Fayaz from the IIA Data Centre for their continuous support and assistance.

My appreciation also goes to the Indian Institute of Astrophysics, Department of Science and Technology for providing all the financial support for my research. Without their assistance,

this work would not have been possible. In particular, I thank IUSSTF for their generous grants which give me to interact with various faculties, scientists in USA. I would also like to mention GARP funding of IISc and IAU travel funds for attending IAU Symposium and present my work in the Jagiellionian University, Poland.

I'm deeply appreciative of Susmita di and Mahua di for their warm hospitality. Their numerous invitations to lunch and dinner gatherings have been a source of great joy and comfort throughout my academic journey. These social interactions provided valuable respite from academic rigors and contributed significantly to my overall experience.

I'd like to give a heartfelt shout-out to all my friends, batchmates, seniors, and juniors who've been there for me throughout this incredible journey:

A big thanks to Sahel da for his guidance with Paraview, to Prerana for her invaluable assistance with LaTeX table, and to Sankalp for his help with statitistical coorelation coefficients. You guys are lifesavers!

I'm deeply grateful to Talwinder, Sindhuja, Gopal da, Prakriti di, Siddartha da, Suchira di, Debesh, Anshu, Atul, Satabdwa da, Ritesh da, and Manjunath - your expertise in your fields has been invaluable. I couldn't have done this without your help!

To Souvik, my campus wandering buddy - thanks for all those stress-busting walks. Alankar and Ritali, our canteen snack breaks were the best! Saie, your constant encouragement meant the world to me. Sougata, you're a star for helping with those parcels.

I'm greatful to Subhadip and Brijesh for their insightful financial advice.

To all my friends who have made this journey memorable, specifically Mayusree, Md. Rashid, Ashwin, Yashi, Jishnu, Ujjal, Mriganka, Mayank, Rohan, Zenia, Rachana, Avinash, Avishek, Bashundhara di, Sankalp, Saikat, Rahul, Praveen, Kiran, Sandeep, Naveen, Soumyaranjan, Subham, Anjali, Kanika, Payel, Swastik, Sioree, Ijas, Biprajit, Jyotirmoy, Joydeep, Souvik (Int PhD), Ujjal, Ronika, Ketaki, Arpit, Nitin, Ambika, Srinjana, Upasana, Jyoti, and Dibya - you've all played a part in making this journey amazing. Whether it was a quick chat, a helping hand, or just being there - I appreciate each one of you. You all have made this journey not just bearable, but truly enjoyable. A special debt of gratitude is owed to Monalisa, whose patience, and understanding have been my sanctuary during the most challenging times. Your unwavering support and belief in me have been vital in this journey. Thank you for being the awesome people you are!

I owe a profound debt of gratitude to my parents, Baba and Maa, for their love and support have been anchor throughout this journey. Thank you for instilling in me the value of education and the importance of perseverance. Your unwavering belief in my abilities has been a source of strength. To my siblings, Antarleena and Anwesana, thank you for your encouragement and for being a constant source of inspiration. Your support means more to me than words can express.

Finally, I acknowledge the privilege it has been to devote these years to the pursuit of knowledge. I am acutely aware that this opportunity is not available to all, and I pledge to use my position to advocate for greater access to education and research opportunities for underrepresented groups in academia.

As I conclude, I am filled with a sense of both accomplishment and anticipation. The end of this journey marks the beginning of another, and I look forward to the new challenges and discoveries that lie ahead. To all who have been part of this incredible journey, I offer my deepest and most sincere gratitude. Your contributions, both seen and unseen, have made this thesis possible and have shaped me into the researcher and person I am today.

Thank you all for your invaluable support and encouragement.

Synopsis

Solar flares and Coronal Mass Ejections (CMEs) are among the most violent and energetic phenomena observed in the solar atmosphere, resulting from the sudden release of immense amounts of energy. A typical solar flare is characterized by a rapid increase in light emission across a wide range of the electromagnetic spectrum, whereas a CME is defined as the expulsion of vast quantities of plasma and high-energy particles from the Sun into space.

Both solar flares and CMEs play crucial roles in shaping space weather, which can have profound effects on Earth. The intense radiation from solar flares can disrupt satellite communications, navigation systems, and power grids, while CMEs can cause geomagnetic storms that impact Earth's magnetosphere, leading to auroras and potential damage to satellites and other space-based technologies. Understanding these phenomena is vital for both scientific research and technological advancements. Solar flares and CMEs both provide insights into the fundamental processes of energy release and particle acceleration in the Sun's atmosphere and offer a unique perspective on the Sun's magnetic field dynamics. Studying the mechanisms behind these events helps scientists develop models to predict solar activity and mitigate its impacts on space weather. This knowledge is essential for improving space weather forecasting and developing strategies to protect Earth's technological infrastructure from solar disturbances.

In addition to their scientific importance, solar flares and CMEs are also of great interest for space exploration. Understanding the behavior of these solar phenomena is critical for ensuring the safety of astronauts and spacecraft. As human space exploration extends beyond Earth's orbit, predicting and preparing for the effects of solar flares and CMEs will be essential for the success of long-duration missions. Thus continued research into these dynamic solar events will enhance our ability to predict and mitigate their impacts, contributing to the advancement of space science and the protection of Earth's technological systems.

In the thesis, we provide an overview of solar eruptions, alongside a discussion of the numerical equations that govern the magneto-hydrodynamic (MHD) simulations used in our study. We also describe the observational instruments utilized to gather data, allowing us to compare our simulation results with observational insights.

Next we provide our study regarding the photospheric magnetic imprints of solar flares associated with coronal mass ejections (CMEs). Solar flares often leave distinct imprints on the magnetic field at the photosphere, typically observed as abrupt and permanent changes in the downward-directed Lorentz force within localized regions of the active region. Our study aims to differentiate eruptive and confined solar flares by analyzing the variations in the vertical Lorentz force. We focus on 26 eruptive and 11 confined major solar flares, all stronger than the GOES M5 class, observed between 2011 and 2017. For this analysis, we utilize SHARP vector-magnetograms obtained from NASA's Helioseismic and Magnetic Imager (HMI).

In addition to observational data, we incorporate data from two synthetic flares derived from a δ–sunspot simulation as reported by Chatterjee et al. (2016). Our methodology involves estimating changes in the horizontal magnetic field and the total Lorentz force integrated over areas around the polarity inversion line (PIL), which encompasses the flare locations. To achieve this, we developed a semi-automatic contouring algorithm that delineates the region near the Polarity Inversion Line (PIL) where the most significant magnetic changes occur.

Our findings indicate a rapid increase in the horizontal magnetic field along the flaring PIL, coinciding with significant changes in the downward-directed Lorentz force in the same vicinity. A crucial aspect of our results is the identification of a threshold in Lorentz force changes. All confined flares in our study exhibit total Lorentz force changes of less than $1.8 \times 10^{20} dyne$. This threshold proves to be a significant factor in effectively distinguishing between eruptive and confined flares.

Moreover, for eruptive events where the change in Lorentz force is below the threshold, we noticed a significantly higher ribbon distance between the parallel flare ribbons, typically exceeding 15 Mm at the onset time of the flare. This indicates a potential implication between the ribbon separation and the magnitude of the Lorentz force change during eruptive events. Therefore, ribbon separation could serve as an additional factor to consider when studying the magnetic imprints associated with the solar flares. We applied the similar procedure to the B & C class synthetic flare events and noticed a remarkable resemblance in the temporal evolution with the observational data. Our observation indicates that the Lorentz force propagates from the reconnection site towards the photosphere. This provides valuable insights into

understanding the mechanisms of flare-related upward impulse transmission, which is crucial for the associated coronal mass ejection (CME) dynamics. Our study not only enhances the understanding of the magnetic and dynamic characteristics of solar flares but also has significant implications for predicting the potential impact of these solar events on space weather. The ability to distinguish between eruptive and confined flares based on Lorentz force changes could lead to better understanding of the relation between the sunspot topology and the ejective flaring.

Finally, we shed light on the changes in reconnection flux throughout the evolution of CMEs, from their onset to eruption. Additionally, we correlate these reconnection flux changes with the acceleration of the ejected material. Coronal mass ejections (CMEs) are among the most powerful drivers of space weather, with magnetic flux ropes (MFRs) widely considered their primary precursors. However, the three-dimensional variation in reconnection flux during the evolution of MFRs throughout CME eruptions remains insufficiently understood. Here, we present a detailed study utilizing a realistic three-dimensional magneto-hydrodynamic (3D MHD) model to explore the temporal evolution of reconnection flux during MFR evolution. Our approach integrates both numerical simulations and observational data to provide a comprehensive analysis.

We begin our investigation with an initial coronal configuration characterized by an isothermal atmosphere and a potential arcade magnetic field, beneath which an MFR emerges at the lower boundary. Our model incorporates radiative cooling and a coronal heating function. Additionally, we have included field-aligned Spitzer thermal conduction. However, our model does not account for solar wind. As the MFR rises, we observe significant stretching and compression of the overlying magnetic field. This dynamic process leads to the formation of a current sheet, initiating magnetic reconnection. The reconnection process gradually intensifies, eventually resulting in the impulsive expulsion of the flux rope.

Our simulation generates two homologous CME eruptions, each characterized by an impulsive increase in kinetic energy and a corresponding release of magnetic energy. The peak velocities of the CMEs in our simulation are approximately 224 $\mathrm{km\,s^{-1}}$ and 213 $\mathrm{km\,s^{-1}}$. In the first eruption, the magnetic flux rope exhibits only torus instability, while in the second eruption, it demonstrates both torus and kink instabilities. Our analysis focuses on the temporal evolution of reconnection fluxes during these two successive MFR eruptions, with the twisted flux continuously emerging through the lower boundary. To complement our simulations, we perform a parallel analysis using observational data from NASA's Helioseismic and Magnetic

Imager (HMI) and the Atmospheric Imaging Assembly (AIA) along with Solar TErrestrial RElations Observatory (STEREO-A) spacecraft for a specific eruptive event.

Our findings indicate that changes in reconnection flux play a crucial role in determining CME dynamics. Specifically, the acceleration of CMEs are linearly correlated (CC = 0.58 and 0.81) to the amount of the reconnection flux, highlighting the importance of reconnection dynamics in the overall process of CME initiation and propagation.

This nearly realistic simulation of a solar eruption offers significant insights into the complex dynamics of CME initiation and progression. The ability to model and understand the temporal evolution of reconnection flux in three dimensions provides a more accurate and detailed picture of the mechanisms driving CMEs. Consequently, our study enhances the understanding of how the reconnection flux changes over time during the solar eruption processes and demonstrates the vital role of reconnection flux and acceleration of CMEs from the onset to the eruption.

Finally, we provide a brief overview of our future goals. In this thesis, we have presented realistic magneto-hydrodynamic (MHD) simulations of solar eruptions alongside observed space-based data. By comparing the simulation results with observational data from instruments, we aim to enhance our understanding to better represent the solar eruptions and their impacts. Our research not only closes the gap between theoretical models and observational data but also underscores the crucial role of concurrent observation and simulation in understanding solar eruptions. By leveraging both observational data and modeling efforts, this thesis lays the groundwork for further improvements of such lower corona models and techniques to a border range of solar eruptions study and their implications for solar physics.

List of Publications

1. **Maity, S. S.**, Sarkar. R., Chatterjee, P., & Srivastava, N. (2024) Changes in photospheric Lorentz force in eruptive and confined solar flares. The Astrophysical Journal, 962(1), 86. DoI: https://doi.org/10.3847/1538-4357/ad13f0.

2. **Maity, S. S.**, Sarkar. R., Chatterjee, P., & Mytheen I. S. (2024) Evolution of reconnection flux during eruption of magnetic flux ropes. (Submitted to The Astrophysical Journal). DoI: arXiv:2407.18188v2

Table of contents

List of figures

List of tables

1

Introduction

1.1 The Sun

Since ancient times, humans have recognized the Sun's crucial role in supporting life on Earth. Earth's atmosphere is sustained by the energy provided by the Sun in the form of light and heat, influence the it's climate, and sustain life. Without the Sun's continuous energy flow, the existence of plants and animals would be impossible. Nearly every aspect of our planet's habitability depends on the Sun, whether directly or indirectly. From the day-night cycle and ocean tides to global climate and food and energy resources, the Sun is central to life on Earth. Therefore, studying our closest star is essential to understanding the broader universe. The systematic study of the Sun began in the early seventeenth century when Galileo Galilei used a telescope to observe sunspots, although Chinese astronomers had noted these dark patches as early as 165 BCE. Because of its proximity, the Sun has been observed in great detail for a long time, something that is impossible for other stars, even with modern technology. Advances

in instruments and observation techniques have expanded solar physics beyond just visible surface images. Now, multi-wavelength astronomy, magnetic field measurements, and Doppler velocity measurements offer unprecedented spatial, spectral, and temporal resolution. These advancements provide valuable insights into the Sun's complexities and highlight that many solar phenomena remain to be understood. Indeed, the Sun serves as an astrophysical laboratory where fundamental theories related to space physics plasma can be tested and verified. The Sun is a G2-type main-sequence star that formed around 4.5 billion years ago from the gravitational collapse of a large molecular cloud. This collapse reached equilibrium through a balance between the outward pressure from nuclear energy generation and the inward gravitational force. The Sun is expected to stay in its main-sequence phase for another 4.5 billion years before transitioning into a red giant. Currently, the Sun is in hydrostatic equilibrium, with an effective black body temperature of about 5780 K, a mass of approximately 1.98×10^{30} kg, a radius of roughly 6.96×10^{8} meters, and a luminosity of 3.84×10^{26} watts. It holds about 99% of the total mass of the solar system and consists of roughly 73.46% hydrogen, 24.85% helium, and 1.69% heavier elements like oxygen, carbon, neon, and iron. The Sun's activities can disrupt our daily lives by expelling magnetized plasma and charged particles, causing space weather storms that impact Earth's magnetosphere. Phenomena such as the aurora borealis and aurora australis occur when these energetic particles penetrate Earth's atmosphere. These events can affect GPS, communication systems, and power grids, underscoring the critical need for a systematic study of the Sun.

1.2 Solar Interior

The Sun's visible surface, the photosphere, can be observed with the naked eye. However, the deeper layers of the solar photosphere and the Sun's interior cannot be directly observed. Our understanding of the solar interior has been greatly advanced by the Standard Solar Model (SSM) (Bahcall et al., 1982) and helioseismology - the study of solar oscillations (Leibacher et al., 1985). The SSM, developed by solving classical stellar equations and incorporating fundamental physics such as nuclear reactions, photon interactions, and plasma physics, builds a realistic picture of the solar interior by iteratively matching model outputs with real observations. Helioseismology, on the other hand, probes the solar interior by observing waves on the solar surface (Leighton et al., 1962; Ulrich, 1970).

The solar interior is divided into three regions: the core, the radiation zone, and the convection zone.

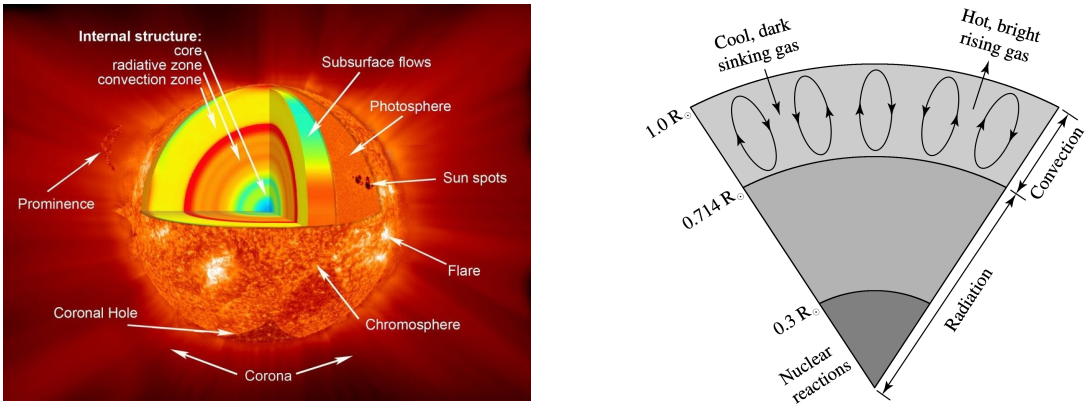

Fig. 1.1 (Left panel) Different layers of solar interiors and atmosphere (Source: NASA). (Right panel) A schematic diagram of solar interiors. In the Sun's interior, energy is initially transported radially outward through radiation. At approximately $0.7R_{\odot}$ convective motions become the dominant means of energy transport to the surface (illustrated from Carroll & Ostlie 1996).

1.2.1 The Core

At the center of the Sun, the core extends out to about 0.25 $R_{\odot}$, containing nearly half the Sun's mass. With a temperature of approximately 15 million K and a density of around 1.6×10^5 $kg\,m^{-3}$, the core acts as a furnace for thermonuclear fusion which is the Sun's energy source (Priest, 2014). This fusion process, primarily following the proton-proton (pp) chains and the carbon-nitrogen-oxygen (CNO) cycle, results in helium nuclei, high-frequency gamma-ray photons (26.2 MeV), and electron neutrinos (0.5 MeV) (Bethe, 1939). While photons lose energy through countless scatterings with dense plasma elements and take about 170,000 years to emerge from the solar surface as blackbody radiation (Mitalas & Sills, 1992), neutrinos escape the core unimpeded, reaching the surface in approximately two seconds and serving as direct diagnostics of core conditions.

1.2.2 The Radiative Zone

Extending from 0.25 to 0.70 $R_\odot$, the radiative zone is characterized by energy transport via radiation. High-energy gamma photons generated in the core are repeatedly absorbed and re-emitted by particles in the radiative zone, moving outward in a random walk. As a result, photons take millions of years to traverse this zone. The density in the radiative zone drops from $2 \times 10^4\ kg\,m^{-3}$ to $2 \times 10^2\ kg\,m^{-3}$, and the temperature falls from 7 million K to 2 million K from the bottom to the top of the zone. Interestingly, if the Sun's core suddenly stopped generating energy, the Sun would continue to shine for millions of years due to the photon travel time through the radiative zone.

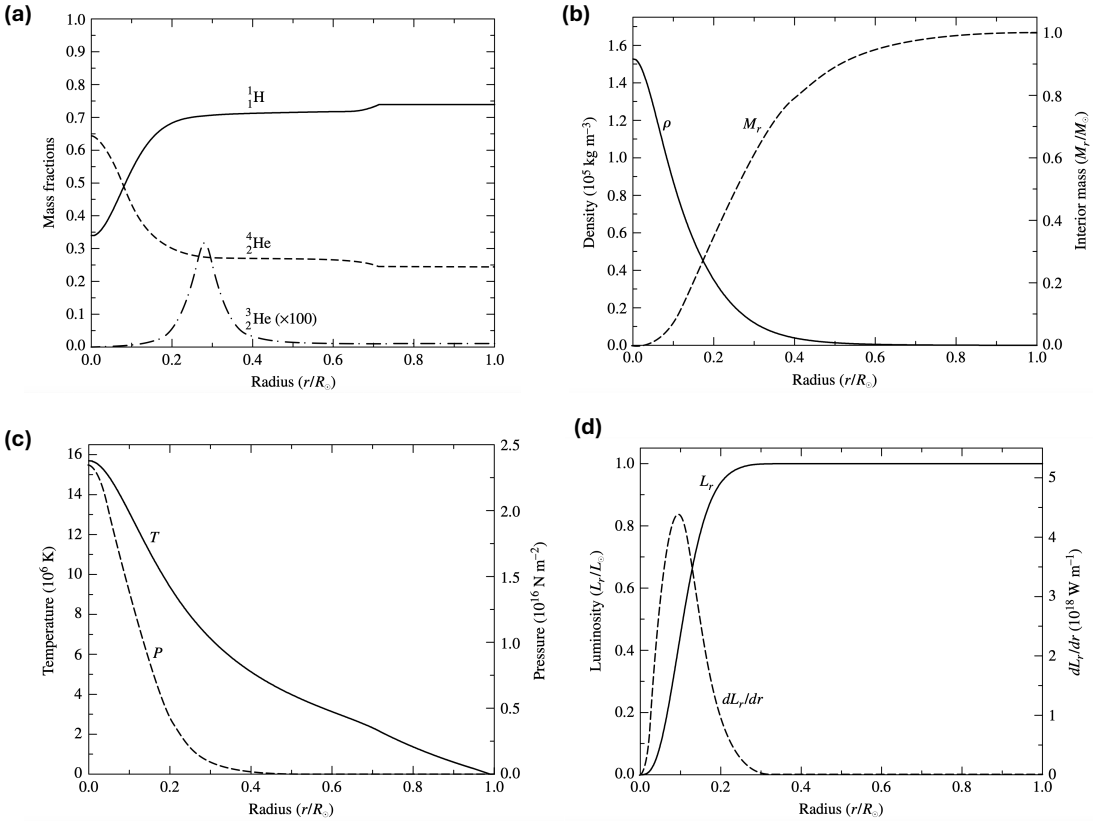

Fig. 1.2 (a) The abundances of elements inside Sun (b) Density profile and the interior mass of the Sun (c) Temperature and pressure profile and (d) Luminosity and derivative of interior luminosity profile as a function of the radius of the Sun (image source Carroll & Ostlie 1996).

1.2.3 The Convection Zone

Above the radiative zone, the increasing opacity creates a high temperature gradient, leading to convective instability. Extending from 0.70 to 1 $R_{\odot}$, the convection zone is where energy is transported by convection rather than radiation. The temperature decreases rapidly with radial distance, reaching around 5700 K at the photosphere. Large convective cells, visible on the photosphere as granules, mediate energy transport. Different convective envelopes within the convection zone rotate differentially. Helioseismic studies reveal a sharp transition between the radiative interior's nearly uniform rotation and the convective envelope's differential rotation at the base of the convection zone, near 0.7 $R_{\odot}$. This transition region, known as the solar tachocline (Priest, 2014), is crucial in heliophysics. The tachocline is believed to play a major role in generating and storing toroidal magnetic flux through the large-scale dynamo mechanism. Due to magnetic buoyancy, this toroidal flux rises from the convection zone's base to the surface, influenced by the Coriolis force during its journey, leading to sunspot pairs with preferential twists in opposite hemispheres. These sunspots, driven by turbulent convective motions, generate a net dipole moment shaping the heliospheric structure. Their distribution varies with solar latitude and follows an eleven-year solar cycle.

At the convection zone's top boundary, radiation finally escapes, making the solar surface visible to us.

1.3 Solar Atmosphere

The Sun's atmosphere consists of several distinct layers of hot plasma and gases, each intertwined with magnetic fields and differing significantly in their physical properties. From the visible solar surface outward, these layers are the photosphere, chromosphere, transition region, and corona.

1.3.1 The Photosphere

The solar photosphere is the visible surface layer of the Sun from which the majority of optical light that we observe emanates. The visible disk of the Sun, often referred to as the "solar surface," marks the base of the photosphere, which is the lowest and most dense part of the solar atmosphere. This layer extends approximately 400 km above the solar interior, with a temperature of about 5800 K and a density of around $10^{-6} g\,cm^3$. As we move outward from the photosphere towards the chromosphere, both temperature and density decrease, reaching a minimum temperature of approximately 4500 K at the uppermost layer of the photosphere.

The photosphere is a thin, highly structured layer of the Sun's atmosphere, about 500 km thick, where radiation decouples from the plasma, rendering the solar surface visible. It can be observed through various optical and near-infrared channels, including Fe I, Fe XI, TiO, G-band, and continuum images (Rutten & Kostik, 1982; Solanki & Stenflo, 1984; Berger & Title, 2001; Wöger et al., 2021). This region is characterized by dynamic phenomena such as sunspots, granules, supergranules, and faculae.

Granules are bright, expanding structures with horizontal dimensions of 1.0 to 2.0 Mm and a lifespan of 5 to 10 minutes (Priest, 2014). They are formed by hot plasma blobs rising from the deep convection zone and appear as part of the turbulent convective cells. These granules are a result of the rapid decrease in density scale height near the photosphere, causing the cell structures to expand (Nordlund et al., 2009). Granules are influenced by p-mode oscillations and exhibit upward and downward vertical velocities, with a correlation between velocity and temperature. After cooling, these plasma blobs descend, creating intergranular lanes.

In addition to granules, supergranules are larger-scale structures with dimensions of 25 to 35 Mm and a typical lifespan of 1 to 2 days (Rieutord & Rincon, 2010). They exhibit a larger horizontal rms velocity (300 to 400 m/s) compared to the vertical velocity (20 to 30 m/s). The exact formation mechanism of supergranules remains unclear, but they are thought to arise from the merging of multiple granules (Rast, 2003).

Magnetic field patterns within the photosphere are varied. Collapsing granules transport magnetic fields, leading to small-scale, strong magnetic concentrations known as magnetic bright points (MBPs), with magnetic strengths up to 1.3 kG and diameters of several hundred kilometers (Beck et al., 2007). Sunspots, the largest structures in this hierarchy, can span up to 60,000 km and appear as dark patches in white light and G-band due to lower plasma temperatures compared to their surroundings (Solanki, 2003). This reduced emission is

maintained by magnetic flux tubes with strengths up to 3.5 kG, which balance the magnetic pressure and the reduced gas pressure inside the tubes.

The photosphere's magnetic field patterns change with the solar cycle. During the solar cycle's rising phase, active regions characterized by sunspot pairs or groups of pairs dominate. As solar activity minimizes, these active regions diminish, leaving behind smaller-scale mixed polarity regions known as Quiet Sun areas. These regions are believed to be influenced by either small-scale dynamo mechanisms or diffuse magnetic fields from larger active regions (Martínez-Sykora et al., 2009). Additionally, unipolar large-scale magnetic fields, known as coronal holes, persist on the solar surface. These regions, appearing as dark patches in X-ray images due to lower plasma density, are characterized by open magnetic fields that allow solar wind to escape into the heliosphere. Coronal holes are predominantly found at higher latitudes.

1.3.2 The Chromosphere

The chromosphere is a layer of the Sun's atmosphere that extends approximately 2500 km above the photosphere. This layer begins where the temperature is about 4500 K, just above the photosphere. The chromosphere is quite faint and becomes increasingly transparent in the continuum spectrum, making it difficult to observe directly. However, it becomes visible during a total solar eclipse when the moon obscures the bright light of the photosphere, revealing a narrow rose-colored band around the Sun's edge—hence its name, which means "color sphere."

The chromosphere is optically thick in certain strong resonance lines. This means it can be observed clearly through these specific wavelengths. Prominent features within the chromosphere include filaments, prominences, spicules, and the chromospheric network found along the boundaries of supergranular cells. Filaments and prominences are essentially the same phenomena observed from different viewpoints. Filaments appear as dark structures in absorption against the bright solar disk, while prominences are bright, glowing features observed in emission at the Sun's limb.

This region is highly dynamic and structured, starting from about 0.5 Mm above the photosphere and extending to about 2 Mm in height. The temperature profile within the chromosphere reaches a minimum of around 4000 K before rising again to between 10,000 and 20,000 K. As the temperature decreases, many ionized atoms become neutral. These neutral atoms interact with the ionized plasma primarily through collisions, as the magnetic field has

little effect on them. The chromosphere can be studied in detail using optically thick lines such as Hα, Ca II, and Mg II, which reveal its complex structure (Pereira et al., 2014).

The chromosphere serves as a crucial boundary where magnetic fields begin to significantly influence the plasma dynamics, outweighing gas pressure effects. This interface causes a portion of the propagating waves to be partially or fully reflected back to the photospheric surface. Moreover, the characteristics of the waves that pass through the chromosphere are altered, making this layer a key region for understanding wave propagation and magnetic field interactions in the Sun's atmosphere.

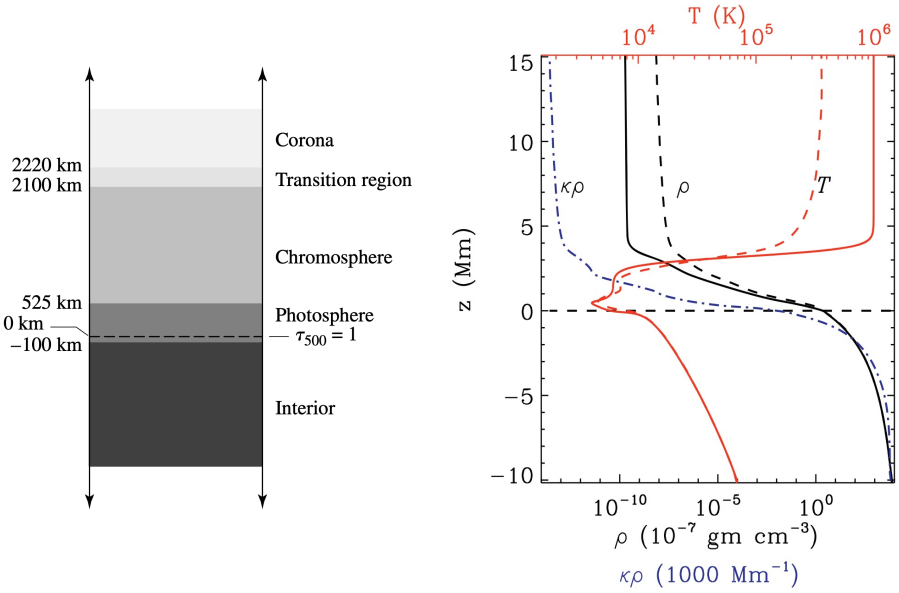

Fig. 1.3 (Left panel) Different layers of Solar atmosphere (illustrated from Carroll & Ostlie 1996). (Right panel) Temperature and Density profile of solar interior as a function of height (image source Chatterjee 2020).

1.3.3 The Transition Region

The transition region is a 100 km thick interface situated between the cooler chromosphere and the million-degree hot solar corona. At the base of this region, the plasma temperature is around 40,000 K. However, within just 100 km, the temperature surges to over a million

Kelvin, while the density drops rapidly. This dramatic and rapid change in temperature and density makes the transition region both a challenging and intriguing subject of study.

The transition region acts as a critical boundary between the relatively cooler chromosphere and the extremely hot corona. In this region, temperature and density undergo significant transformations. Starting from the photosphere, the temperature decreases gradually as one moves down to the bottom of the chromosphere. It then begins to rise slowly within the chromosphere before experiencing a sharp increase in the transition region. Here, temperatures escalate abruptly from around 10,000 K to several million Kelvin.

Conversely, the density undergoes a sudden and significant decrease from the photosphere through the transition region into the corona. Despite its critical role in solar physics, the transition region remains one of the less understood areas of the solar atmosphere. However, observations in ultraviolet lines, such as Si IV and He II, provide valuable insights into this enigmatic layer and the lower corona, helping researchers to unravel the complexities of this interface.

1.3.4 The Corona

The outermost atmospheric layer of the Sun is known as the solar corona. It extends from approximately 2.0 to 2.5 million kilometers above the visible surface. This region was first observed during solar eclipses, which allowed astronomers to glimpse the faint corona obscured by the bright light of the Sun's disk. Due to its extremely low plasma density, the corona is about 10^7 times fainter than the visible solar surface, making direct observation challenging (Zirin, 1988).

During an eclipse, the corona's structure became evident, revealing various features such as streamers, pseudo-streamers, and a continuous outflow of charged particles, known as the solar wind. Eugene Parker introduced the concept of the solar wind in 1958, proposing that it originates continuously from the Sun, overcoming solar gravity, and extends throughout the heliosphere (Parker, 1958). Besides the solar wind, the corona is characterized by several large-scale structures, including streamers, filaments, coronal loops, and coronal mass ejections (CMEs). These features are predominantly influenced by the coronal magnetic field (Withbroe & Noyes, 1977).

To observe the corona regularly, astronomers use coronagraphs—devices that block the Sun's disk to simulate an eclipse and reveal the outer corona. Space-based missions like the Solar Dynamics Observatory (SDO) have provided valuable images of the corona in ultraviolet and X-ray lines, such as Fe XIV and Fe XV (Burgess, 1964). Ground-based observations are limited due to the Earth's atmospheric absorption, which obstructs these high-energy wavelengths.

The temperature of the corona ranges from 0.5 to 2 million Kelvin, a surprising contrast to the Sun's surface temperature, which is only a few thousand Kelvin. This discrepancy is known as the "coronal heating problem," appearing to contradict the second law of thermodynamics. Researchers have suggested that the solution may involve the damping of Magnetohydrodynamic waves or turbulent magnetic reconnection processes, or possibly both (Hudson, 1991).

During periods of high solar activity, the corona is dominated by significant events such as solar flares and CMEs. Flares are intense bursts of electromagnetic radiation resulting from magnetic reconnection, while CMEs involve the ejection of large volumes of magnetized plasma into the heliosphere, accelerating charged particles. When a CME interacts with Earth's magnetosphere, it can disrupt the planet's magnetic shield, posing potential threats to both terrestrial and space-based systems (Fig. 1.5).

Based on the radiation coming from the corona, different spectral regions can be identified.

K-Corona

This visible results from Thomson scattering of photospheric light by free coronal electrons. The K-corona, named after the German word "Kontinuum,". The light from the K-corona is highly polarized and extends from about 1.03 solar radii to 2.5 solar radii. The spectral lines observed in the photosphere are significantly blended due to the large Doppler shifts resulting from the high thermal velocities of the electrons.

The F-corona

This comes from the scattering of photospheric light by dust grains those are much more massive and slower than the electrons. It is dominant beyond 2.5 solar radii, displays Fraunhofer lines

superimposed on the solar spectrum. Together, these components form the white-light corona, which gradually fades into interplanetary space.

E-Corona

In the optical range, the emission corona exhibits numerous lines superimposed on a continuous background. These lines, such as Fe XIV at 5303 Å and Fe X at 6374 Å, are produced by highly ionized atoms, indicating temperatures of around 2 million Kelvin. The low gas density (about 10^6 to $10^8 cm^{-3}$) and high temperature of the corona are evident from these emission lines.

Ultraviolet and X-ray Corona

The high temperatures of the corona cause to emit intensely in the ultraviolet and soft X-ray ranges. Images taken by instruments like the Soft X-ray Telescope (SXT) aboard Yohkoh and the Extreme-Ultraviolet Imaging Telescope (EIT) aboard SoHo show significant differences in brightness due to variations in coronal density and temperature. The intensity of these emissions depends on the plasma's electron density and temperature, enhancing the contrast between different regions of the corona (Fig. 2.5).

1.4 Space Weather and its Drivers

Space weather refers to the disturbances in the Earth's space environment caused due to dynamic activity of the Sun and its atmosphere, that have scientific and technological importance Figure 1.4) (Schwenn, 2006).

As a magnetically active and variable star, the Sun has significant effects on planetary atmospheres. Consequently, near-Earth space is highly susceptible to disturbances caused by explosive solar events, which can lead to extreme space weather conditions. The economic impact of such events can be substantial (Siscoe, 2000). The field of space weather has rapidly advanced, encompassing not only the effects of interactions between the Sun and Earth but also the fundamental physics of astrophysical plasma. More broadly, studying solar variability's

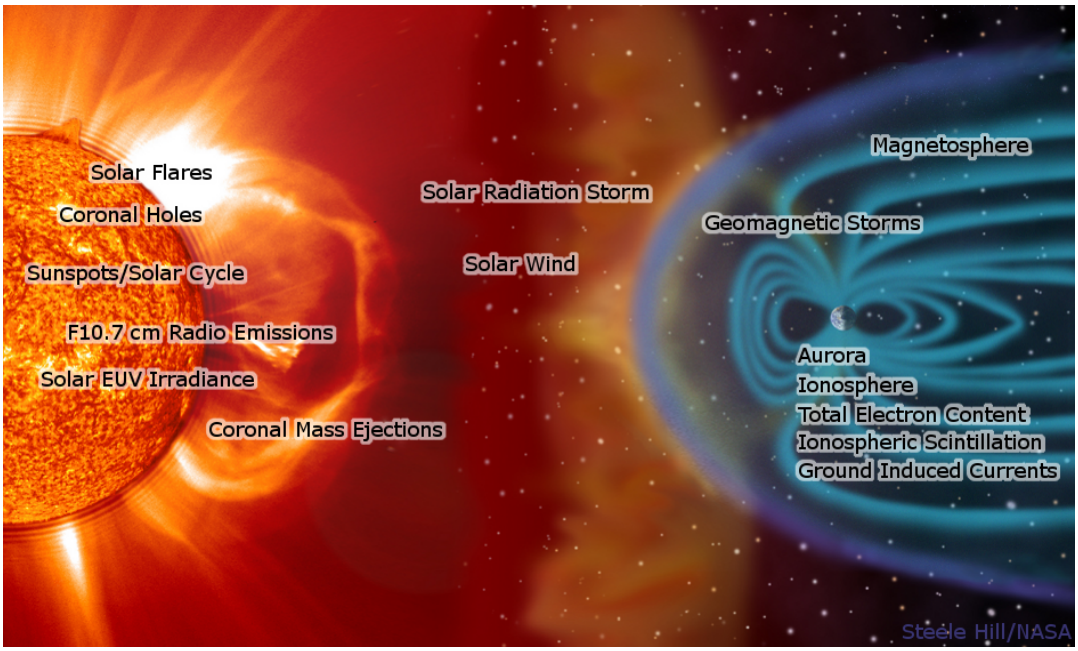

Fig. 1.4 An artistic illustration depicting Sun-Earth interactions that influence space weather.

impact on planetary atmospheres helps us understand the potential for habitability in other solar-like exoplanetary systems.

Violent eruptions in the solar atmosphere, such as solar flares and coronal mass ejections (CMEs), are major causes of severe space weather disturbances (Figure 1.4). Solar flares produce intense bursts of energy that can heat and expand the Earth's atmosphere, increasing atmospheric drag on satellites. This drag can slow satellites down, causing them to fall into lower orbits (Schwenn, 2006). Additionally, the energetic particles released during solar flares can damage satellite systems, leading to failures that disrupt communication and navigation on Earth. These particles also pose health risks to astronauts and airline crews on polar routes. CMEs, on the other hand, are massive clouds of magnetized plasma ejected from the Sun into interplanetary space. When these clouds collide with Earth's magnetosphere after a few hours or days, they can trigger severe geomagnetic storms. Such storms can induce geomagnetically induced currents that interfere with electronic, telecommunication, and power-grid systems on Earth. Therefore, studying the origins and early stages of solar eruptions is crucial for predicting the potential impacts of space weather.

The upcoming sections will provide a brief overview and observational details of these space weather drivers.

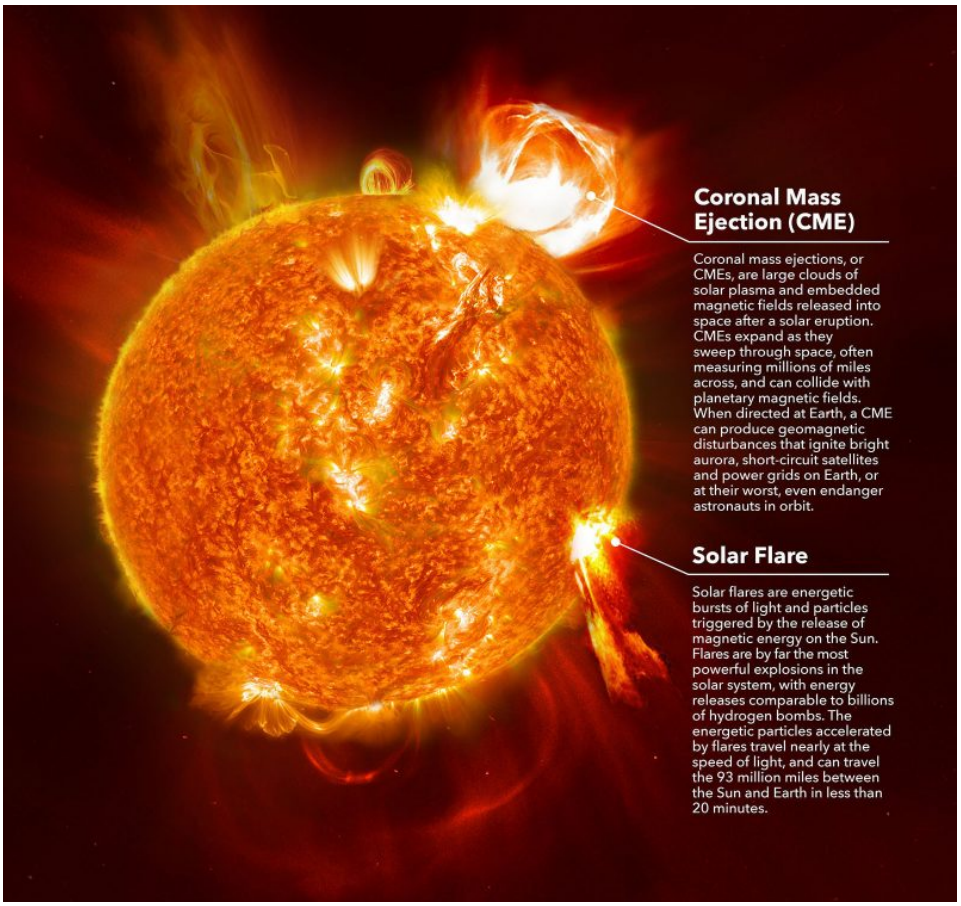

Fig. 1.5 An infographics of major space weather drivers - solar flares and coronal mass ejections. Source: NASA

1.5 Solar Flares

Solar flares are among the most intense explosive events in the solar atmosphere. Observationally, they are characterized by a sudden increase in brightness across the electromagnetic spectrum, releasing energy ranging from 10^{28} to 10^{34} ergs over timescales of seconds to several minutes (Benz, 2008). The first recorded observation of a solar flare was made by R.C. Carrington and R. Hodgson on September 1, 1859. They noted localized, brief brightenings on the solar photosphere in white light, now known as the "Carrington white light flare." This event was linked to a significant space weather impact, as a powerful geomagnetic storm, the largest ever recorded, occurred on September 2, 1859. Following this initial observation, reports of solar flares became more frequent as studies began to focus on the Sun in the Hα line from the solar chromosphere. With advances in space-based technology, we can now capture

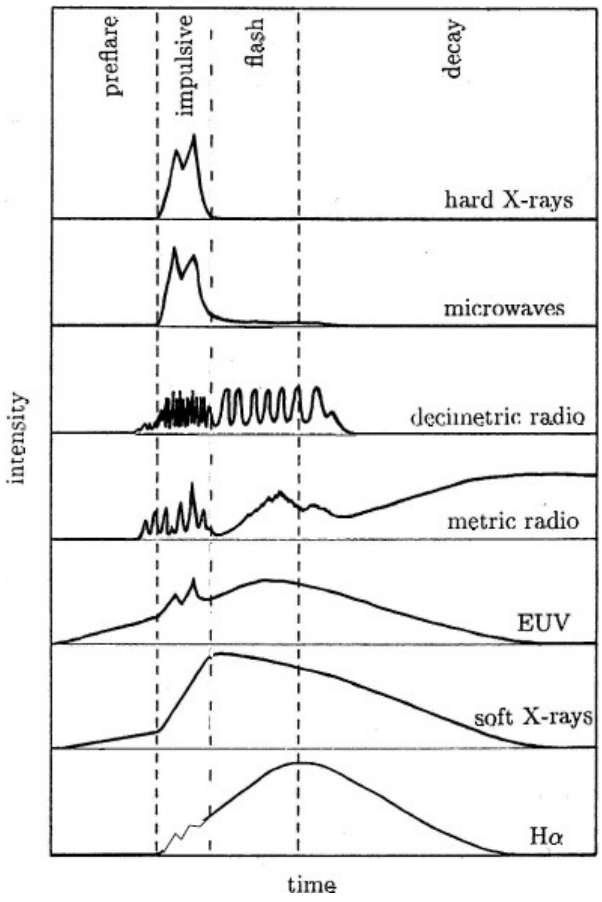

Fig. 1.6 A schematic profile of the temporal evolution of flare intensity in different wavelengths. The vertical dashed lines mark the different phases of solar flare (acquired from Benz 2008)

multi-wavelength images of solar flares with high spatial resolution and temporal cadence Figure 1.7).

The phases of flare energy release are generally categorized into pre-flare, impulsive, flash, and decay phases, as illustrated in Figure 1.6. During the pre-flare phase, the coronal plasma in the flaring region gradually heats up and becomes detectable in soft X-rays and EUV. In this phase, many energetic ions and electrons are accelerated and strike the dense chromosphere, leading to the appearance of hard X-ray footpoint sources at chromospheric altitudes (Hoyng et al., 1981). Additionally, some high-energy particles become trapped in the magnetic field, producing intense emissions in the radio band. The thermal soft X-ray and Hα emissions reach their peak after the impulsive phase, which is marked by a more gradual release of energy. The rapid rise in the Hα light curve, known as the flash phase, often overlaps with the impulsive phase, though Hα emissions may peak later. In the decay phase, the lower coronal plasma mostly returns to its pre-flare state, while in the high corona (beyond 1.2 $R_{\odot}$), particles continue

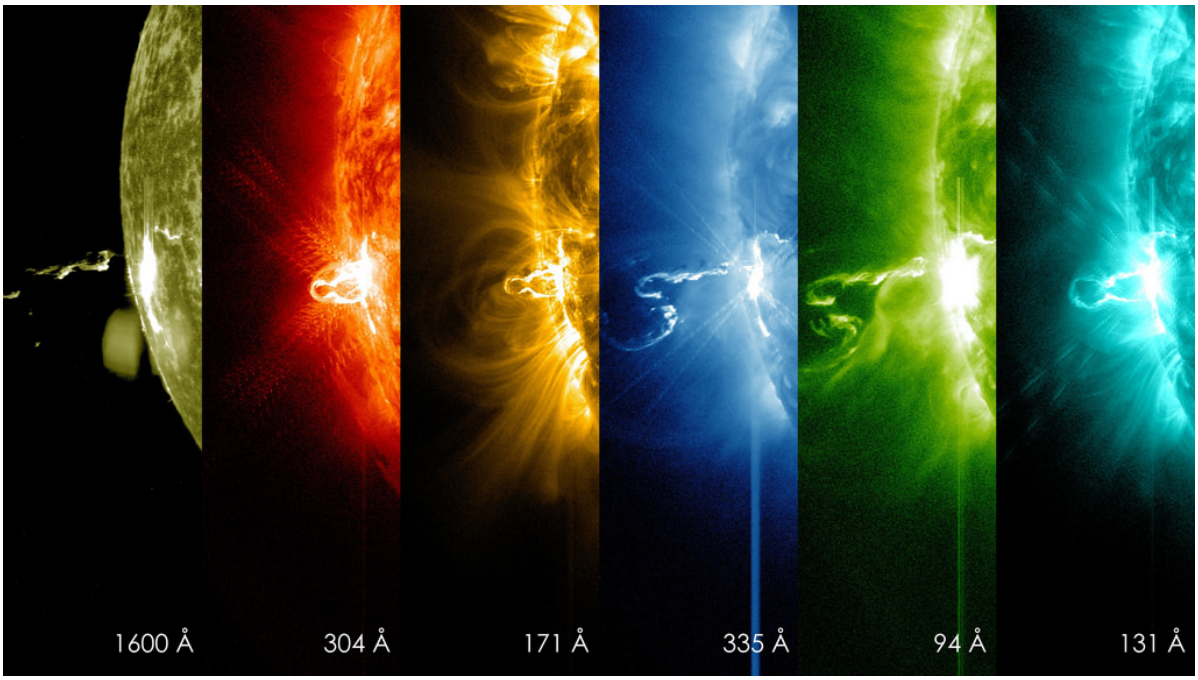

Fig. 1.7 NASA's Solar Dynamics Observatory captured these images of a large flare erupting from the sun Feb. 21, 2014. Credit: NASA/SDO

to accelerate due to plasma ejections and shock waves, leading to meter-wave radio bursts and energetic particle events.

1.6 Coronal Mass Ejections

Coronal mass ejections (CMEs) are massive clouds of magnetized plasma that are ejected from the Sun into the heliosphere and can sometimes cause severe space weather effects on Earth (Tsurutani et al., 1988; Gonzalez et al., 1999; Huttunen et al., 2005; Schwenn, 2006; Yurchyshyn et al., 2005; Gopalswamy et al., 2008). Observations show CMEs as large, transient structures in the solar corona. To detect CMEs, coronagraphs are used, which are equipped with artificial occulting disks to block the intense light from the solar photosphere. This is crucial because the corona is much less dense compared to the photosphere. By blocking this bright light, coronagraphs allow us to see features in the solar corona (Howard, 2011). The light from the solar photosphere is Thomson-scattered by free electrons in the coronal and heliospheric plasma, which can be captured by solar coronagraphs. While CMEs appear

relatively faint against the background corona, they are highly transient, so they are usually detected by subtracting the background.

The first space-based observations of CMEs began in the early 1970s with the OSO-7 coronagraph (Tousey et al., 1973). Subsequently, better quality and longer-term observations were made by Skylab (1973–1974, Gosling et al., 1974), P78-1 (Solwind) (1979–1985, Sheeley et al., 1983), and the Solar Maximum Mission (SMM) (1980; 1984–1989, Hundhausen, 1999). A major advancement came in late 1995 with the launch of SOHO, which continues to provide CME observations with two of its three LASCO coronagraphs (Domingo et al., 1995). Another significant development occurred in late 2006 with the launch of the twin STEREO spacecraft, which provide multi-viewpoint observations of CMEs (Howard et al., 2008). Ground-based observations have also complemented space-based data, including the K-coronameter at the Mauna Loa Solar Observatory (MLSO) (Fisher & Poland, 1981; Koomen et al., 1974) and green line observations from coronagraphs at Sacramento Peak, New Mexico (Demastus et al., 1973) and Norikura, Japan (Hirayama & Nakagomi, 1974). In addition to white-light coronagraphic imaging, CMEs have also been observed using interplanetary radio scintillation (1964–present, Hewish et al., 1964; Vlasov, 1981). However, white-light observations are generally more advantageous than radio, infrared, or ultraviolet observations because Thomson scattering is wavelength-independent and depends only on electron density (Hundhausen, 1993).

When coronal mass ejections (CMEs) travel out into the heliosphere, they become known as interplanetary coronal mass ejections (ICMEs). In-situ observations of ICMEs reveal that their magnetic and plasma properties differ from those of the surrounding solar wind. Key signatures of ICMEs include an increased magnetic field strength and reduced variability compared to the ambient solar wind.

1.6.1 Shape and Geometry

White-light images captured by coronagraphs measures the spatial distribution of scaterred photospheric photons by the free electrons (Thomson scattering) in the corona. Since the corona is optically thin at visual wavelengths, the images captured by coronagraphs represent the true three-dimensional density structures projected onto two dimensions. This projection makes the geometric interpretation of CMEs challenging. In these images, CMEs can display various forms, including three-part structures, narrow jets, and streamer blowouts, which emerge from pre-existing coronal streamers.

There are generally two main appearances of CMEs in common observations: limb CMEs and disk-center CMEs, also known as halos. Limb CMEs originate from the solar limb and propagate perpendicular to the LOS. They are more easily observed and often exhibit a three-part structure (Illing & Hundhausen, 1985; Hundhausen, 1999), which includes a bright front—a dense coronal plasma shell surrounding a dark region and associated with overlying fields swept up by erupting flux ropes (the leading edge)—a cavity associated with the flux rope, and a core representing cooler plasma typically linked to bright prominence material. Figure 1.8, for example, shows a typical three-part structured CME imaged by the LASCO/C3 coronagraph aboard SoHO on February 27, 2000.

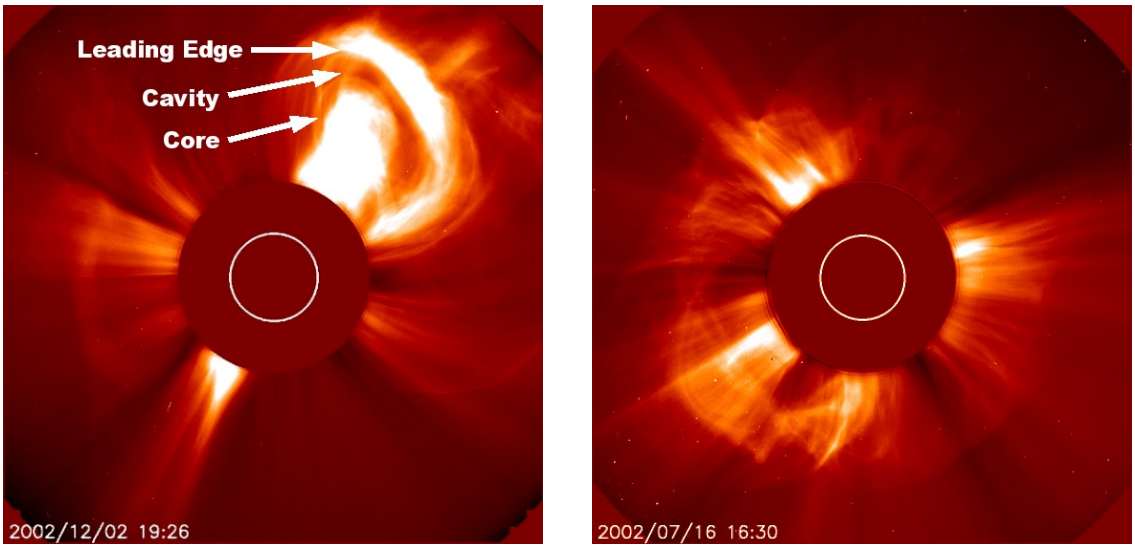

Fig. 1.8 (Left) An example of three part structure of a CME. The leading edge, core and dark cavity are indicated. (Right) Observations of a halo CME as captured by the Solar and Heliospheric Observatory (SOHO).

Conversely, disk-center CMEs, or halos, originate from the disk center and propagate parallel to the LOS. These CMEs appear unstructured in the images, covering the occulter either partially or fully as they move along the LOS, as illustrated in Figure 1.8.

1.6.2 Location, Size and frequency

During solar minimum, CMEs usually appear to be clustered around the equator, but during solar maximum they spread across up tp 60 degrees north and south pf the equator (St. Cyr et al., 2000; Yashiro et al., 2004). Hundhausen (1993) noted that this distribution change is more aligned with streamers and prominences than with active regions or sunspots. This pattern is linked to the global solar magnetic field changes, such as the tilt angle of the heliospheric current sheet (HCS), during the Sun's transition from solar minimum to maximum. This correlation has been confirmed by LASCO data (Gopalswamy, 2004; Gopalswamy et al., 2010b), with a notable decrease in CME and prominence eruptions around 2006 when the HCS flattened below 30° solar latitude.

The angular width of a CME is defined as the angle between the two outer edges of the CME relative to the center of the solar disk. This measurement is well-defined for limb CMEs. However, for halo CMEs, the angular widths are often overestimated because they propagate along the line of sight, covering the coronagraph's field of view either partially or fully. The distribution of CME angular size, as observed in the plane-of-sky, changes throughtout the solar cycle (Yashiro et al., 2004) and peaks around 40 degree (Hundhausen, 1993; Howard et al., 1985). whereas the average width including halo CMEs was around 60 degree. These halo CMEs usually originate from regions within a few tens of degrees of the Sun's center from the observer's perspective (Webb, 2002). Some studies suggest that halo CMEs are faster and more energetic than non-halo CMEs (Gopalswamy et al., 2010a).

The number of CMEs observed daily varies significantly between solar minimum and maximum. Tousey et al. (1974) reported a CME rate of 0.5 per day near solar minimum. Later,Hildner et al. (1976) estimated an average rate of one CME per day. Webb & Howard (1994) conducted a detailed study of CME rates using data from Skylab, SMM, and Solwind, finding a long-term average rate similar to Hildner's estimate. During the early phase of the SoHO mission (1996-1998), corresponding to the rising phase of solar cycle 23, St. Cyr et al. (2000) found that the CME rate based on LASCO data was consistent with earlier observations. However, Gopalswamy et al. (2003) analyzed the complete LASCO dataset from 1996 to 2002 and discovered that the CME rate varied from less than one per day during solar minimum to slightly more than six per day at solar maximum. Their analysis indicated that the CME rate is significantly higher during periods of solar maximum. The rate fluctuates from about one CME per day during solar minimum to around five per day at solar maximum (St. Cyr et al., 2000).

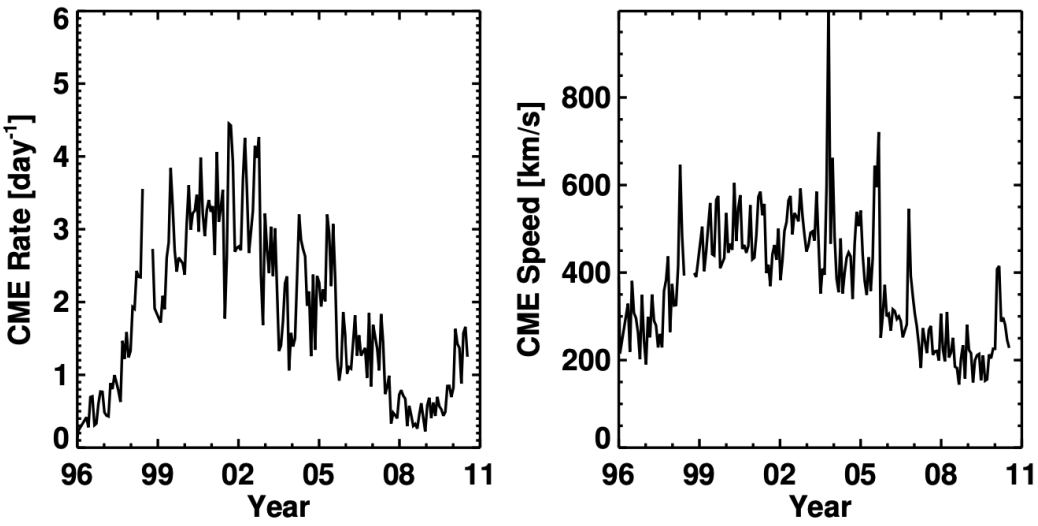

Fig. 1.9 (Left) LASCO CME occurance rate (Right) mean speed from 1996 to 2011 averaged over Carrington rotations. Adpated from Gopalswamy et al. (2010a).

1.6.3 Kinematics

The speed and acceleration of CMEs in the initial solar radii have been studied by various researchers using different space-based instruments (e.g., Gosling et al. (1976); Howard et al. (1985); Hundhausen et al. (1994); St. Cyr et al. (2000); Gopalswamy et al. (2003). CME speeds range widely from 50 to 3000 km s^{-1}, with an average around 400-500 km s^{-1}. In comparison, the slow solar wind in the corona travels at about 300-400 km s^{-1}, while the fast solar wind reaches about 750 km s^{-1}. The sound speed in the corona at typical temperatures of 1.5-2.0 MK is around 175 km s^{-1}, indicating that CMEs travel at both sub-sound and super-Alfvén speeds. Above 2 $R_{\odot}$, CME speeds tend to stabilize, though slower CMEs can accelerate and faster ones may decelerate due to interactions with the solar wind. Most acceleration of CMEs occurs below 2 $R_{\odot}$. Observations from ground-based studies showed that CMEs associated with active regions often have constant speeds, while those linked to prominence eruptions typically show constant acceleration. Studies of flare-associated CMEs revealed a three-phase kinematic profile: a slow rise, rapid acceleration, and a final phase of constant or decreasing speed. Gradually accelerating CMEs often appear balloon-like in coronagraph images, whereas fast CMEs maintain constant speeds up to 30 $R_{\odot}$.

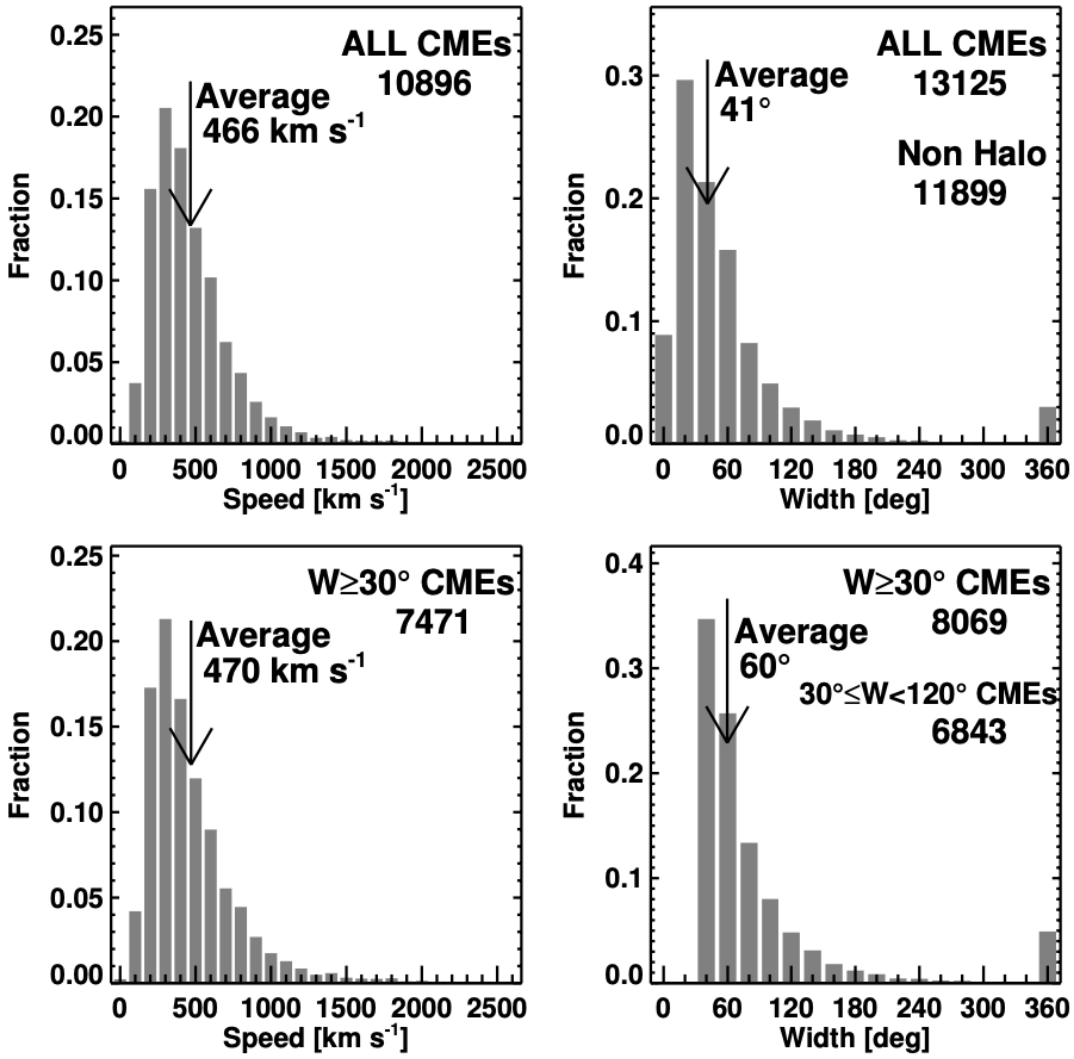

Fig. 1.10 Speed and width distribution of all CMEs (top) and only wider CMEs (bottom). Acquired from Gopalswamy et al. 2010b.

1.7 Signature of CMEs

Since their discovery in the 1970s, understanding the origin and initiation mechanisms of CMEs is essential dentifying the mechanisms that trigger CMEs is challenging, as they are linked to phenomena near the solar surface. CMEs are also related to other forms of solar activity, such as solar flares, and prominence eruptions. These phenomena are typically observed using electromagnetic spectrum instruments, especially EUV and H-α imagers. The following section provides a brief overview of some of these commonly observed signatures of CMEs.

1.7.1 Solar Flares

Throughout the history of detailed solar observation since around 1850, solar flares were believed to be the primary cause of interplanetary disturbances. These disturbances are the cause of significant space weather effects on Earth. When interplanetary shocks were discovered by Mariner 2 in 1964, they were initially thought to be blast waves from solar flares. Similarly, upon the discovery of CMEs in 1973, they were also considered to be flare-driven. However, research in the 1970s and 1980s established that CMEs are distinct phenomena and are primarily responsible for geomagnetic storms and interplanetory shocks. This was conclusively argued by Gosling (1993), although the idea was contested by others, such as Hudson et al. (1995). Today, CMEs and flares are regarded as related but separate phenomena.

Flares and CMEs are distinct phenomena, yet they may share a common root cause: magnetic reconnection. CMEs can occur without accompanying flares, and most flares do not involve coronal mass ejections. However, when they occur together, flares typically precede CMEs, though CMEs carry significantly more energy. A unified model, such as the "Flux Cancellation" or "Catastrophe" model (Shibata et al., 1995; Lin et al., 2004), explains that a stressed magnetic arcade containing a flux rope can rise, leading to magnetic reconnection beneath it. This reconnection heats the plasma within the CME and increases the magnetic flux of the CME, while also producing shock waves and energetic particles that generate flares. If a prominence lifts off slowly, it may not produce detectable surface brightening or flares.

While most flares happen without any dependence of CMEs, the fastest and most energetic CMEs are often associated with bright flares. For instance, nearly all frontside, full halo CMEs are linked to reported flares (Webb, 2002; Gopalswamy et al., 2007). The likelihood of linking a CME to a soft X-ray flare increases with the flare's duration, eventually reaching 100% for flares lasting more than 6 hours (Sheeley et al., 1983). More energetic flares are also more likely to be associated with mass ejection (Yashiro et al., 2005).

The relationship between CMEs and flares has been a major focus in solar physics, with ongoing debates about their cause-effect dynamics due to the lack of high-resolution observations of CMEs in their early phases. The development of models and better observational tools continues to refine our understanding of these solar phenomena and their interconnectedness.

1.7.2 Erupting Prominences

CMEs can also occur in conjunction with solar filament or prominence eruptions. Several studies have investigated the relationship between erupting prominences and CMEs (Munro et al., 1979; Sinha et al., 2019). Prominences consist of cool, dense plasma suspended in the corona, appearing bright at the limb but dark as meandering ribbon-like structures on the solar disk when observed in H-α, where they are called filaments. These solar filaments can remain in a quiescent phase for several hours or even days. The prominence material is believed to be confined by overlying magnetic field and supported within highly sheared magnetic fields or twisted magnetic flux ropes (Martin, 1998; Wang & Muglach, 2007; Gaizauskas, 2008). When these magnetic structures are destabilized, triggering a CME, the associated prominence can also erupt. Figure 1.11 illustrates a fragment of an erupting prominence tied to a CME eruption at the North-East side of the solar limb in an EUV difference image of the Sun.

When a flux rope carrying a filament aligns along the line of sight at the solar limb, it appears as a dark cavity, which is observable in white light (Waldmeier, 1970), soft X-rays (Vaiana et al., 1973), and extreme ultraviolet (EUV) (Schmahl, 1979). During an eruption, the low coronal cavities form a dark cavity structure in white light observations, and the prominence material at the lower end of the cavity becomes the bright core of the CME. This manifests the characteristic three-part structure of CMEs (Gibson & Fan, 2006; Vourlidas et al., 2013; Howard et al., 2017).

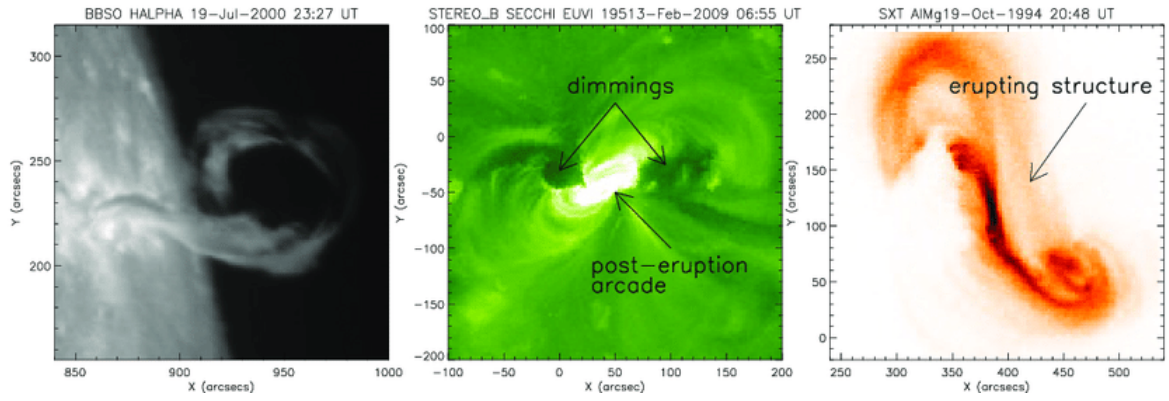

Fig. 1.11 Lower coronal signatures of CME occurrences include various observational manifestations. filament eruptions (left panel), post-eruption arcades and dimming regions (middle panel), and rising EUV/soft X-ray structures (right panel). reproduced from Green et al. 2018

1.7.3 Coronal Dimming

Coronal dimming is characterized by the removal of coronal mass following a CME launch, typically lasting several hours. Studies using X-ray (Rust & Hildner, 1976), EUV (Thompson et al., 2000), and Hα (Jiang et al., 2003) observations have concluded that this dimming results from a reduction in density rather than a temperature change. The structure of coronal dimming closely matches that of CMEs, making it an effective indicator of CME projections on the solar surface (Reinard & Biesecker, 2008). Mandrini et al. (2007) suggest that dimming marks the footpoints of CME flux ropes. An example of a CME-associated dimming region is illustrated in 1.11. Studies indicates there may be two types of dimming: "core" dimmings, which are directly linked with the active region and flare, and "secondary" dimmings, which occur at a distance and believed to be related to the loop motions or evacuation (Attrill et al., 2010; Dissauer et al., 2018; Kazachenko et al., 2022; Afanasyev et al., 2023).

1.7.4 Post eruption arcade

Post-eruption arcades (PEAs) or post-flare loops (PFL) as described by Tripathi et al. (2004), are bright large-scale transient loop like structures observed in the low-coronal region using EUV wavelengths. These structures form occasionally after a CME launch due to magnetic reconnection (Sterling et al., 2000). This reconnection compresses the reconnected field lines towards the Sun, creating an arcade-like shape. The study by Tripathi, Bothmer, and Cremades found significant associations between PEAs and CME footpoints, as illustrated in Figure 1.11. At H-α wavelengths, the footpoints of these loops often appear as ribbons, commonly referred to as two-ribbon flares.

1.7.5 X-Ray & EUV Sigmoids

Sigmoids are S-shaped structures commonly observed on the solar disk, often linked to active regions (Canfield et al., 1999). These sigmoidal forms are thought to arise from twisted magnetic fields. The twisting the magnetic field lines above the magnetic neutral line can create these helical structures, which appear S-shaped in projection. They are frequently seen in soft X-ray and EUV images (Canfield et al., 1999; Sterling et al., 2000). The orientation

of these twisted loops shows a hemispheric preference: forward S-shapes are more common in the southern hemisphere, while reverse S-shapes dominate in the northern hemisphere, regardless of the solar cycle (Rust & Kumar, 1996). Sigmoids are considered observational signatures of azimuthal currents in twisted coronal structures such as loops, arcades, or filaments (Aschwanden, 2004). When the helical twist surpasses a critical threshold, the structure may become unstable, leading to CME (Gibson & Low, 2000). Canfield et al. (1999) found that active regions with a sigmoidal shape are statistically more likely to erupt. During CME an S-shaped region can transform into a set of bright loops (Hudson et al., 1998). The active region evolves from a sheared sigmoid visible in X-rays to a post-eruption arcade (Kahler, 1977; Sterling et al., 2000).

1.7.6 Coronal Waves

"EIT waves" Thompson et al. (1998), often referred as coronal waves, named after the Extreme Ultraviolet Imaging Telescope on the SoHO mission, are large-scale wave disturbances observed in the Sun's lower corona. These waves appear as propagating bright fronts that travel almost isotropically across the visible solar disk, being obstructed by coronal holes and avoiding active regions (Thompson et al., 1998, 1999). The typical speed of these waves is about 250 $\mathrm{km\,s^{-1}}$. They are strongly associated with CMEs, as confirmed by observations from EIT at 195 Å(Plunkett et al., 1998; Biesecker et al., 2002). Behind the front of these waves, a dimming region is usually observed, indicating the evacuation of mass during the CME (Thompson et al., 2000; Zhukov & Auchère, 2004). Harra & Sterling (2001) found blue-shifts in the oxygen five line in a dimming region, supporting the outward ejection of coronal matter.

1.7.7 Shock waves & SEPs

When a CME's speed exceeds the local Alfvén speed, it can create a forward shock. This shock is often linked with Type II radio bursts, which are caused by Langmuir waves generated by plasma movements ahead of the shock. Type IV bursts, particularly moving ones, suggest magnetic plasma ejections and the presence of nonthermal particles due to magnetic reconnection. Observations with SOHO have confirmed that metric Type II bursts are commonly associated with CME-driven shocks, and the relationship between these has been recognized since the

1950s. The Type II burst often correlates with the CME's kinetic energy: metric bursts are linked with high-energy CMEs, decameter-hectometric (DH) bursts with moderate energy, and bursts extending to kilometric wavelengths with the most energetic CMEs.

Detecting shocks in white-light coronagraph images has historically been challenging. Methods such as observing kinks in streamers and changes in Type II dynamic spectra have helped to infer the presence of shocks on CME flanks. Bright rims ahead of fast CMEs observed by LASCO are now thought to indicate shocks. EUV data from SDO-AIA have provided kinematic details of these spherical shocks.

Ultraviolet spectroscopy offers clear observations of coronal shocks by showing increases in emissivity and Doppler dimming of specific lines, such as H I Ly-α and O VI. Although only a few shocks have been reported due to the quick passage of shocked gas through the UVCS slit, broad O VI profiles with temperatures over 10^8 K have been detected. Bemporad & Mancuso (2010) characterized shock parameters using SOHO data, including shock compression ratios and plasma temperatures, and found that magnetic and kinetic energy densities increased significantly across the shock.

CME-driven shocks can accelerate electrons and ions, leading to solar energetic particle (SEP) events. There is a strong link between SEPs and fast CMEs, indicating that these shocks are responsible for SEP acceleration. Early studies suggested a two-stage acceleration process involving both the flare and the CME-driven shock, a theory confirmed by later in-situ data. During the SOHO mission, numerous large SEP events were observed, particularly around solar maximum, and were associated with fast, wide CMEs that often decelerated due to coronal drag. The most energetic SEP events, including ground-level enhancements (GLEs), are linked with the fastest CMEs.

SEP source regions are generally in the Sun's western hemisphere, as particles follow the Parker spiral interplanetary field lines. The distribution of SEP-CME differs from that of CMEs causing geomagnetic storms. As a result, all fast, wide frontside CMEs are considered potentially significant for space weather. Notably, SEPs are often associated with active regions experiencing multiple CMEs, suggesting interactions between CMEs may enhance particle acceleration. The CME's kinetic energy is themost significant part of the eruption's energy budget, with up to 10% potentially contributing to SEP acceleration, highlighting the efficiency of CME-driven shocks in particle acceleration.

1.7.8 Evidance of reconnection and current sheets

Sui & Holman (2003) were the first to report a hard X-ray event with a compact source above a vertical current sheet, indicating magnetic reconnection. Subsequent studies have shown that hard X-ray sources are very hot (around 10^7 to 10^8 K) and are associated with the reconnection X-point. The downward source probably represents hot plasma from newly reconnected arcade loops. The current sheet is limited to a thin surface, as predicted by MHD theory, where magnetic forces compress currents into narrow layers. Observations of CME-associated current sheets have increased with better data. Observations from Yohkoh/SXT and Hinode/XRT have provided evidence of the formation of current sheets. With LASCO, cases of CME-associated rays and Y-shaped structures were reported, and St. Cyr et al. (2000) identified these features in a significant fraction of LASCO CMEs. UVCS observations of CME-associated rays showed high temperatures and densities, indicating active reconnection. For example, the CME of 18 November 2003 had a flux-rope appearance followed by a rapidly brightening ray, with blobs moving along the ray at about 1000 $\mathrm{km\,s^{-1}}$, indicating bursty reconnection.

Ciaravella et al. (2000) were the first to directly measure the density and thickness of current sheets by combining UVCS aand white light data. Bemporad & Mancuso (2010) derived turbulent speeds and their evolution, suggesting that the observed thickness of current sheets exceeds classical predictions, potentially indicating high effective resistivity. These findings are consistent with the Petschek reconnection mechanism and turbulent reconnection models.

1.8 Magnetic Flux Rope as CME Precursor

Large-scale solar eruptions, such as flares and coronal mass ejections (CMEs), can unleash enormous amounts of energy—up and can significantly impact the space environment around Earth. These events are primarily driven by changes in the Sun's magnetic field. These fields are essential for phenomena such as magnetic reconnection and particle acceleration. In the solar corona, where the plasma β (the ratio of gas pressure to magnetic pressure) is typically very low, the magnetic field exerts a dominant influence. The magnetic field in the corona can become highly stressed due to the emergence and movement of photospheric flux, leading

to the accumulation of excess magnetic energy. When this energy is eventually released, it triggers solar eruptions.

Magnetic reconnection is thought to be the primary mechanism behind these eruptions. It transforms magnetic free energy into radiation and accelerates energetic particles. Additionally, magnetic reconnection disrupts the magnetic field connections to the Sun, allowing large quantities of magnetized plasma to be ejected into space as CMEs. Understanding how the magnetic field configuration evolves in the corona is crucial for explaining the nature and causes of these eruptions. Direct measurements of the magnetic field in the corona and chromosphere are challenging due to their low density and high temperatures, which limits our ability to observe these regions directly. This has led to the development of various theoretical models. One such model is the standard CME/flare model, which proposes that a magnetic flux rope (MFR) in the corona is expelled into space. An MFR is essentially a bundle of twisted magnetic field lines situated above the polarity inversion line (PIL) in the photosphere, with its ends anchored in the dense photosphere. Observable features of MFRs include filaments, sigmoids, or hot channels.

As the MFR rises, it stretches and compresses the overlying magnetic field, leading to the formation of an electric current sheet where reconnection occurs. The magnetic energy released during reconnection follows the newly formed field lines down to the chromosphere, resulting in two parallel flare ribbons at the footpoints of these field lines. A key feature of flux ropes is their magnetic twist, which implies the presence of field-aligned electric currents in the low-β coronal environment. Observations and simulations suggest that, twisted fields can be created by photospheric and sub-photospheric flow motions or by the emergence of current-carrying flux tubes into the corona. Coronal flux ropes vary greatly in size. For example, those associated with coronal mass ejections (CMEs) can be as large as the Sun and maintain their structure even as they travel beyond Earth. Mini flux ropes, found in coronal jets, are much smaller, spanning only a few arcseconds. Plasma blobs seen in CME wakes or above helmet streamers are also considered small flux ropes formed through magnetic reconnection. Interplanetary flux ropes, such as magnetic clouds (MCs), have diverse sizes and typically last about a day at Earth's orbit, compared to smaller flux ropes that last from tens of minutes to a few hours.

The nature of the magnetic flux rope (MFR) before a solar eruption remains unclear, and there is ongoing debate about whether an MFR exists before the flare or forms during the flare itself (Forbes, 2000; Moore et al., 2001; Chen, 2011). Resolving this question is crucial for advancing our understanding of solar eruptions. Although there is considerable evidence

suggesting that MFRs could be present before eruptions (Cheng et al., 2017), a consensus on their formation process and location has not yet been reached. One theory proposes that MFRs might emerge from below the photosphere due to buoyancy (Fan, 2001; Magara, 2004; Martínez-Sykora et al., 2008; Archontis et al., 2009). Another theory suggests that MFRs could form directly in the corona through magnetic reconnection before the eruption occurs (van Ballegooijen & Martens, 1989; Amari et al., 2003; Aulanier et al., 2010).

Force	Notation	Source Term
Hoop force (upward)	F_h	$f_h = J_T B_{Pi}$
Strapping froce (downward)	F_s	$f_s = -J_T B_s$
Tension force (downward)	F_t	$f_t = -J_P(B_g + B_{Ti})$

Table 1.1 Different forces acting on the MFR. The fields and currents are shown in right panel of Figure 1.12. J_T and J_P are the toroidal and poloidal current respectively. B_s and B_g are strapping and guide field whereas B_{Pi} and B_{Ti} are internal fields in poloidal and toroidal direction.

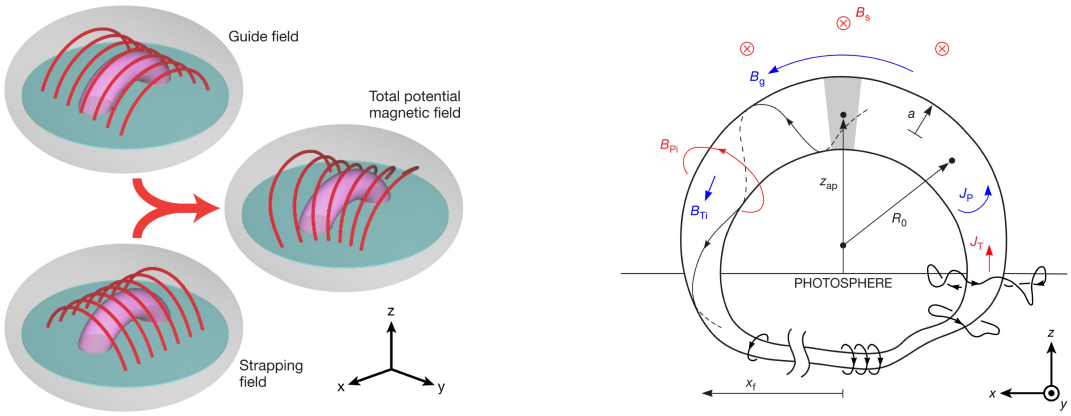

Fig. 1.12 Left panel: Configuration of the potential magnetic field and magnetic flux rope. The strapping field runs poloidally to the flux rope axis and produces strapping force, whose rapid spatial decay can trigger the torus instability. The guide field, runs toroidally along the flux rope axis. It stabilizes the kink instability and creates a confining magnetic tension force. The total potential magnetic field is the combination of the guide field and strapping field which are obliquely aligned to the flux rope. The figure is acquired from Myers et al. (2015) Right Panel: Magnetic fields and currents in an arched, line-tied MFR. The poloidal magnetic field are shown in red while the toroidal fields are shown in blue. The external fields B_s and B_g are generated by the Sun, while the internal fields B_{pi} and B_{Ti} are generated by the currents in the rope. The figure is borrowed from Chen (1989).

1.9 Triggering mechanism of CMEs

Research into the origins of coronal mass ejections (CMEs) has been extensive, but pinpointing their exact initiation mechanism remains a challenging issue in solar physics. Currently, several well-accepted theories attempt to explain how CMEs are triggered. CMEs are rarely isolated events; they often occur alongside other solar phenomena, especially solar flares and prominence eruptions. A solar flare is a sudden release of energy, visible as a bright flash in EUV, X-ray, and H-α wavelengths. Initially, it was believed that flares triggered CMEs. However, it is now understood that not all CMEs are associated with solar flares, and the pressure from a flare alone is insufficient to initiate a CME (Low, 1981; Emslie et al., 2004). Filaments, or prominences when seen at the solar limb, are cooler and denser structures suspended in the corona, appearing dark against the solar disk. Both flares and CMEs are driven by the release of magnetic energy stored in the coronal magnetic field. CME models generally fall into two categories based on their physical processes. Fast CMEs, which accelerate rapidly, are often explained by models involving magnetic reconnection. In these models, the magnetic field's structure changes, converting magnetic energy into thermal and kinetic energy, and can also account for solar flare formation. Slow CMEs, which accelerate more gradually, are typically explained by ideal MHD (magnetohydrodynamic) instabilities. For a comprehensive overview of CME models, see reviews by Forbes et al. (2006) and Howard (2011). Below are descriptions of some resistive models, which involve magnetic reconnection, and ideal MHD models.

1.9.1 Resistive CME Models

Tether cutting

The tether cutting model explains the process leading up to the eruption of a coronal mass ejection (CME). This model, described by Moore & Roumeliotis (1992) and Moore et al. (2001), involves shearing motions along the magnetic neutral line between the two footpoints of a preexisting filament. The less sheared overlying magnetic field lines constrain the sheared structure. Due to the imbalance between the sheared field's pressure and the overlying field's tension, the structure begins to rise. A current sheet forms beneath the filament where reconnection occurs, causing the filament to rise further. This newly formed current sheet

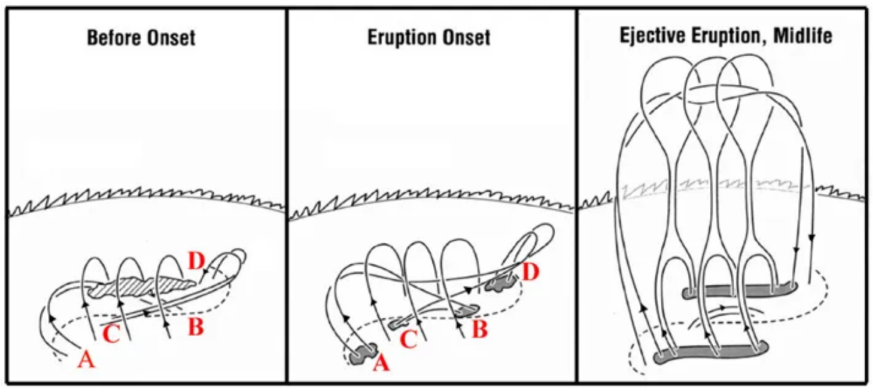

Fig. 1.13 The tether-cutting scenario as the triggering mechanism for CMEs. Left panel: A filament suspended above highly sheared magnetic field lines, such as AB and CD. Before the eruption most filed lines around the filament are in a force-free state, except for those supporting the filament material. Middle panel: As magnetic shear increases, the positive leg of the field line CD moves closer to the negative leg of the field line AB, creating a configuration of anti-parallel field lines that initiate magnetic reconnection. The field lines AB and CD reconnect, forming a long field line AD and a short loop CB. This reconnection process cuts the theaters supporting the filament material, causing the long loop AD to expand upward and the short loop CB to shrink downward. Right panel: As localized reconnection continues, the core field near AD pulls the filament upward, stretching the overlying magnetic field lines and forming an elongated current sheet (acquired from Moore et al. 2001).

accelerates further reconnection, resulting in the filament eruption and the formation of a CME. Figure 1.13 illustrates the process graphically.

Observational signatures supporting the tether-cutting mechanism include filament eruptions and two-ribbon flares, preceded by small H-α brightenings.

1.9.1.1 Flux cancellation

Flux cancellation is similar to the tether-cutting mechanism proposed by van Ballegooijen & Martens (1989). Flux cancellation occurs when magnetic fields of opposite polarity disappear at the neutral line (Martin et al., 1985). Initially linked to solar flares (Livi et al., 1989) and later to coronal mass ejections (CMEs) (Amari et al., 2000; Lin et al., 2004), this process arises near the polarity inversion line of shared arcades compared to the surrounding photospheric region. The surrounding field lines encircle and form helical field lines, and reconnection beneath this structure cancels out the magnetic flux, leading to the formation of a magnetic flux rope (van Ballegooijen & Martens, 1989). Continued flux cancellation increases magnetic

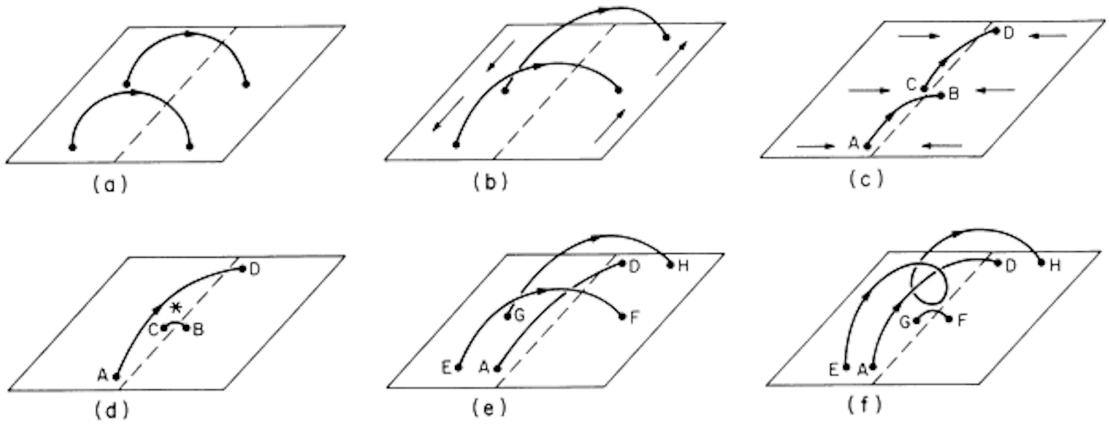

Fig. 1.14 Flux cancellation in a sheared magnetic field. Solar photosphere is represented by the rectangle where as the dashed line is the polarity inversion line (PIL), (a) Initial potential field; (b) sheared magnetic field due to the photospheric motion along the PIL; (c) shear is further increased due to flows toward the PIL; (d) reconnection results long loop AD and a shorter loop CB which subsequently submerges; (e) overlying loops EF and GH are pushed to the PIL; (f) reconnection produces the helical loop EH and a shorter loop GF which also submerges (acquired from van Ballegooijen & Martens 1989).

pressure, causing the flux rope to rise (Forbes & Isenberg, 1991) and eventually erupts. Figure 1.14 illustrates the flux cancellation method graphically While both mechanisms are alike, the primary difference is that flux cancellation describes a more gradual evolution, whereas tether cutting is a more impulsive process.

1.9.1.2 Magnetic breakout

Another resistive model for CME initiation is the magnetic breakout model (e.g., Antiochos et al. (1999); Aulanier et al. (2000); Lynch et al. (2004). Unlike the tether cutting and flux cancellation models, in this model, the initial magnetic configuration involves a quadrupolar topology with a magnetic null point above the central flux system, where reconnection occurs between parts of the flux rope and the field lines of adjacent magnetic flux systems. As shearing motions continue, the increased magnetic pressure causes the central flux system to expand. As the stress rises, overlying magnetic field lines and sections of the flux rope form a current sheet, leading to reconnection ahead of the flux rope. Consequently, the magnetic X-point above the central flux system elongates into a horizontal layer, forming an enhanced electric current. This reconnection removes the upper magnetic loops, triggering the eruption of the core field, such as the filament, erupts subsequently due to reconnection beneath it.

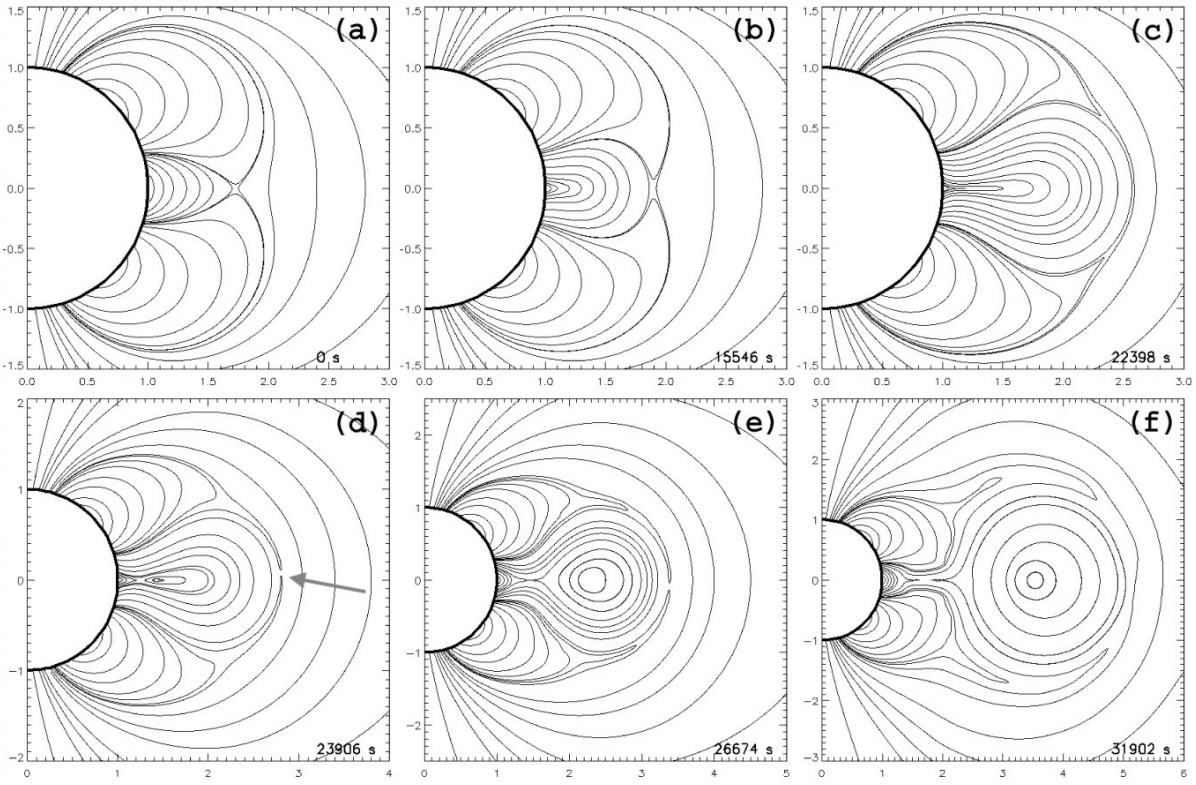

Fig. 1.15 Magnetic field lines during the eruption, as described by the the breakout model. The flux rope system rises and reconnects with the overlying field lines (shown with an arrow). A current sheet forms behind an isolated flux rope and magnetic reconnection subsequently triggers the flux rope's eruption (acquired from Lynch et al. 2004).

Magnetic field lines during an eruption, as described by the breakout model, show the flux rope system rising and reconnecting with the overlying magnetic field lines (indicated by an arrow). A current sheet forms behind the isolated flux rope, and magnetic reconnection subsequently triggers the flux rope's eruption.

1.9.2 Ideal MHD instabilities

Given the lengthy timescale for energy accumulation in the coronal magnetic field compared to the rapid occurrence of flares and filament eruptions, it was suggested that the triggering mechanism for such energy releases is likely related to some form of instability (Gold & Hoyle, 1960). Forbes (2000) outlines various mechanisms behind these instability processes. The evolution of the coronal magnetic field, driven by photospheric motions and flux emergence,

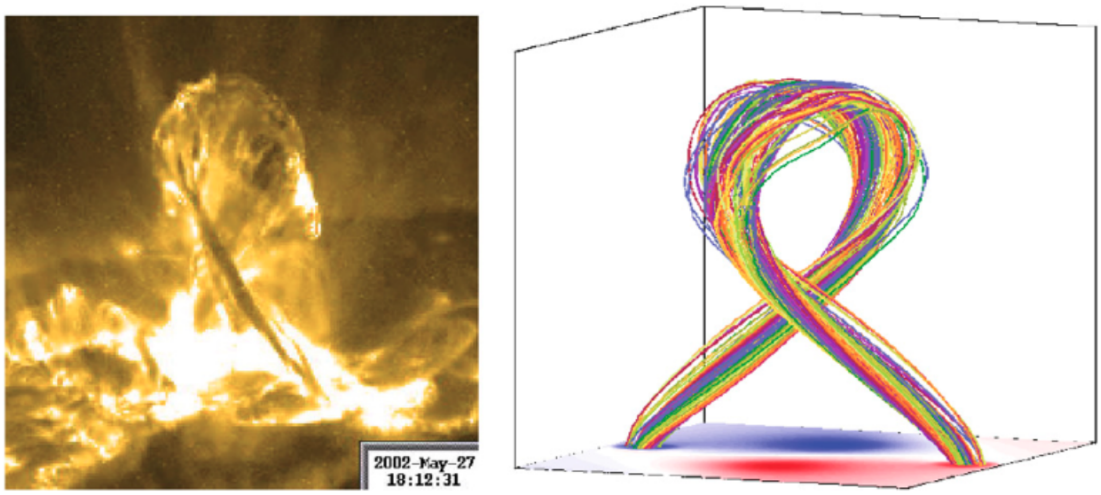

Fig. 1.16 (Left) Observation of a erupting filament by TRACE 195 Å . (Right) Kink unstable flux rope.

occurs in a quasi-static manner until it reaches a critical point where instability begins, leading to an eruption. The primary instability mechanisms thought to play a significant role in CME initiation are described as follows.

Kink instability

Kink instability is one of the ideal magnetohydrodynamic (MHD) instabilities that can develop in a twisted magnetic flux tube, as demonstrated in numerical experiments by Sakurai (1976). Considering the line-tying effect of the solar photosphere, Hood & Priest (1979) identified a critical twist limit (1.25 turns around the central axis) above which the flux tube becomes unstable which triggers the flux rope to erupts. Observations from the Transition Region And Coronal Explorer (TRACE) in the 195 Å band, as shown in the left panel of Figure 1.16, alongside simulations of the kinked magnetic flux rope in the right panel, illustrate this process. A vertical current sheet forms beneath the flux rope, facilitating the eruption of the structure, which may occur with or without magnetic reconnection (Rachmeler et al., 2013).

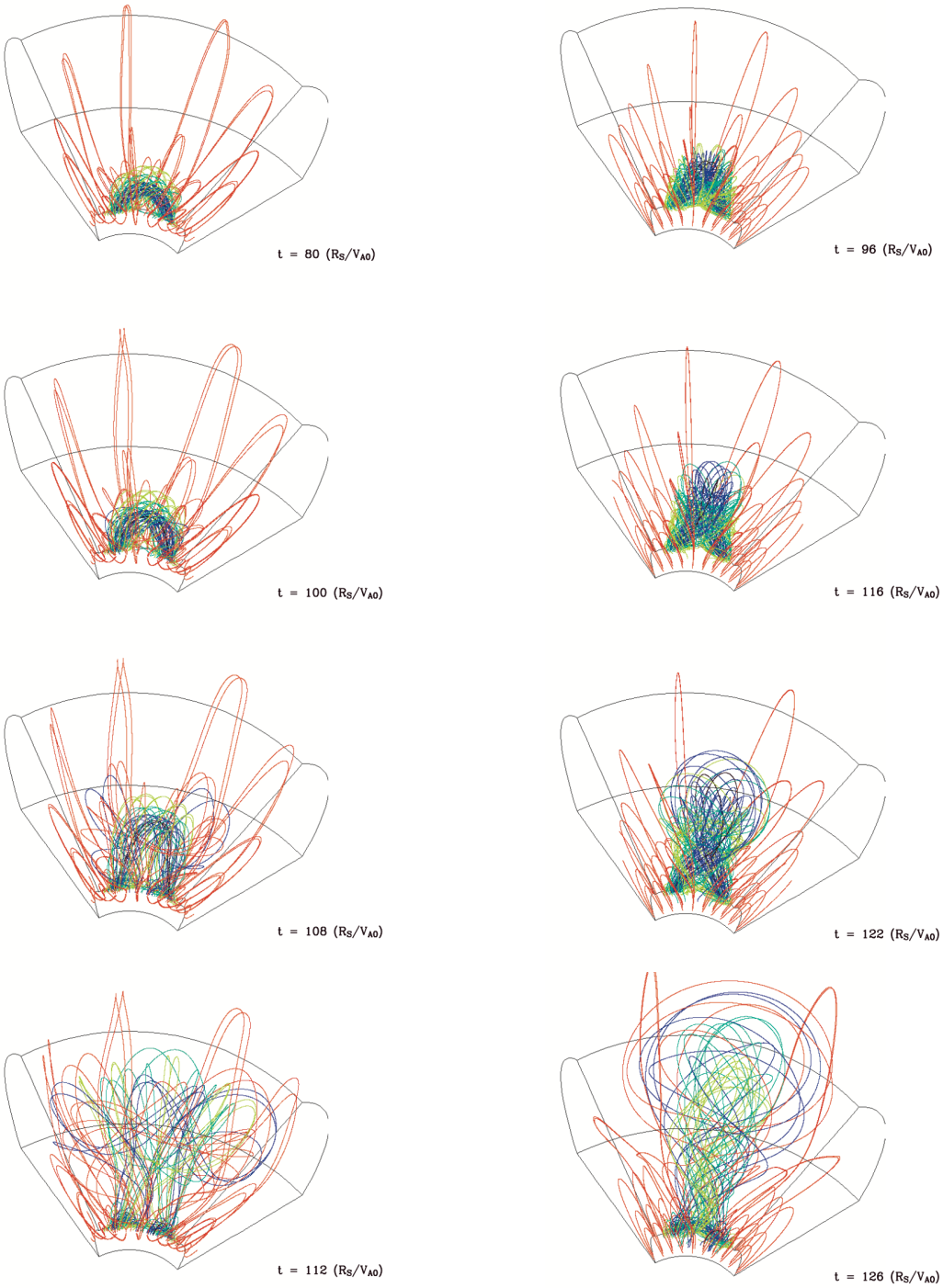

Fig. 1.17 Sanpshot of MFR undergoes (left) torus instability and (right) kink instability (acquired from Fan & Gibson (2007)).

Torus instability

Torus instability is another ideal MHD instability crucial for the initiation of CMEs, as proposed by Kliem & Török (2006). A magnetic flux rope, characterized by its helical magnetic structure, carries an axial current. Numerical experiments have shown that a current-carrying ring becomes unstable and expands if the external potential field decays rapidly with height (Bateman, 1978). Kliem & Török (2006) extended this study and identified a critical parameter known as the decay index, defined as

$$n = -\frac{d \ln B_{\mathrm{ex}}}{d \ln h}$$

where h is the height above the solar photosphere and B_{ex} is the external magnetic field. They found that if the flux rope rises to a height where the decay index reaches a critical value of approximately 1.5, the flux rope system becomes unstable and can lead to a CME eruption.

Fan & Gibson (2007) conducted a 3D MHD simulation to study the emergence of a flux rope from beneath the solar surface into the corona, as depicted in Figure 1.17. Their findings revealed that when the ambient magnetic field decays slowly with height, a highly twisted emerging flux tube can erupt via kink instability, as shown in the top panels. Conversely, if the ambient magnetic field decays rapidly with height, even a weakly twisted flux tube can still erupt due to torus instability.

Despite the advances in understanding the various possible initiation mechanisms for CMEs, it remains unclear whether magnetic reconnection or ideal MHD instability predominantly drives these eruptions.

1.10 Motivation and thesis outline

Understanding the origin and initial evolution of Coronal Mass Ejections (CMEs) is crucial for predicting geomagnetic storms, which have a wide range of space weather effects (Pulkkinen, 2007). Observational studies by Harrison (1990); Subramanian & Dere (2001); Michalek & Yashiro (2013) indicate that solar active regions are the primary sources of CMEs, with the characteristics of these regions determining the nature of the associated eruptions. It is well established that the geo-effectiveness of a CME is influenced by its initial kinematic properties (Srivastava & Venkatakrishnan, 2002). These initial kinematics can vary based on whether

the CME is associated with solar flares. Thus, studying the relationship between flares and CMEs is important, as flare-rich active regions are more likely to produce high-speed CMEs that can lead to severe space weather events (Falconer et al., 2002; Gopalswamy et al., 2010b). However, not all flare-rich active regions produce CMEs, resulting in confined flaring events (Sun et al., 2015; Chen et al., 2015).

Most research to date has focused on the evolution of the photospheric magnetic field to study the characteristics of CME-producing regions associated with flares (Sudol & Harvey, 2005; Wang, 2006; Petrie & Sudol, 2010; Petrie, 2012). To fully understand the CME productivity of flare-rich active regions, similar studies should be conducted for confined flaring events. Although magnetic reconnection is believed to play a crucial role in triggering the eruption of magnetic flux ropes (MFRs), major studies are lacking due to insufficient observational data in the lower corona. Significant challenges include the absence of high-cadence, high-resolution photospheric vector magnetogram data to study CME source regions, gaps in the field-of-view of white-light imagers for capturing CME initiation below 2 solar radii ($R_{\odot}$), and the lack of direct measurements of near-Sun CME magnetic field strength, which is vital for space weather forecasting models.

While Gopalswamy et al. (2018) examined changes in reconnection flux at the moment of eruption, the temporal evolution of CME velocity with reconnection flux during the course of the eruption remains unexplored. Magnetic reconnection is essential in the early stages of CME dynamics. Theoretical models, numerical simulations, and observational analyses indicate the increased CME mass acceleration coincides with an increased rate of magnetic reconnection at the solar source (Lin & Forbes, 2000; Cheng et al., 2003; Deng & Welsch, 2017). Observations by Qiu et al. (2004) demonstrated a temporal correlation between the reconnection rate inferred from two-ribbon flare observations and CME acceleration. Numerious prior studies have found a strong correlation between the total flux reconnected in flare-associated CMEs and the velocity of the CMEs (Qiu & Yurchyshyn, 2005; Gopalswamy et al., 2018).

This thesis aims to investigate the origin and initial evolution of coronal mass ejections (CMEs). The studies conducted to achieve these objectives are organized into several chapters. Chapter 2 and Chapter 3 describe the numerical simulation techniques and the observational data and instruments used, respectively, to provide a comprehensive understanding of the underlying physics. Chapter 4 explores the association between flares and CMEs, identifying thresholds that determine when flares are likely to be associated with CMEs and when they are not. This chapter also examines the role of magnetic topology in active regions. Chapter 5 focuses on the correlation between reconnection flux and the velocity of the magnetic flux

rope from its onset to eruption. It includes simulations of homologous eruptions and compares the results with observations. Finally, Chapter 6 summarizes our findings and outlines future research plans.

2

Governing equations of Magnetohydrodynamics

2.1 Introduction

The Magnetohydrodynamics (MHD) approximation, also known as the single-fluid approximation, is the simplest method to study the solar atmospheric plasma and its interactions with electric and magnetic fields. This theory combines the equations of hydrodynamics with Maxwell's equations of electromagnetism. For this formalism to be valid, two criteria must be met: the number of particles within the Debye volume must be significantly greater than one, and the timescale under consideration must be longer than the inverse of the characteristic frequencies of the system (such as the plasma frequency, collisional frequency, and gyrofrequency). These conditions are satisfied in the Sun's internal regions but begin to break down in the corona due to a significant drop in particle density.

To conduct our three-dimensional numerical simulations, we used the Pencil Code framework. It is a highly modular higher-order finite difference code, well-suited for magnetohydrodynamic (MHD) simulations, providing the capability to model complex solar phenomena with high accuracy. To create a realistic model, we incorporate several non-ideal physics processes, including viscous diffusion, shock dissipation, Ohmic diffusion, and non-adiabatic effects such as thermal conductivity and radiative cooling, to our simulations with solar observations. We solve all dynamic equations using a non-conservative approach and achieve high accuracy with higher-order finite difference schemes. Additionally, we use hyper-diffusivity to reduce numerical instabilities on the grid scale, allowing us to effectively reach high Reynolds number regimes. This chapter briefly describes all the building blocks of the code. We will explore a wide range of parameters in subsequent chapters to understand the overall behavior and coherence among different key components.

2.2 The Equations

The equations addressed by the PENCIL CODE are essentially the standard compressible MHD equations. However, due to its modular structure, variations of the MHD equations can be applied, and certain equations or specific terms (such as those related to magnetism or entropy) can be deactivated as needed. This section presents the equations in their most comprehensive form.

2.2.1 Continuity equation

In our implementation of the Pencil Code, we formulate the continuity equation as:

$$\frac{\mathrm{D}\ln\rho}{\mathrm{D}t} = -\boldsymbol{\nabla}\cdot\mathbf{U} \tag{2.1}$$

Here $\mathbf{U}$ represents the plasma fluid velocity. The operator $\mathrm{D}/\mathrm{D}t \equiv \partial/\partial t + \mathbf{U}\cdot\boldsymbol{\nabla}$ is the Lagrangian derivative.We choose to evolve $\ln(\rho)$ rather than ρ to avoid potential numerical instabilities associated with negative density values.

2.2.2 Equation of motion

We address the velocity field equation, which incorporates several key terms notably, the Lorentz force exerted by the magnetic field (**B**), kinematic viscosity (ν) and shock viscosity (ζ_{shock}). The correction term ($\mathbf{F}_{\text{corr}}$) arising from the semi-relativistic Boris correction (Chatterjee, 2020). The specifics of the semi-relativistic Boris correction will be elaborated upon in a dedicated section 2.7.

In scenarios without magnetic fields, this equation reduces to the standard Navier-Stokes equation for fluid dynamics. It's important to note the highly non-linear nature of this equation, particularly when dealing with large Reynolds numbers, which represent the ratio of inertial forces to viscous forces. In the context of the solar environment, we encounter extremely high Reynolds numbers ($\approx 10^{12}$), due to the immense physical scales involved and the rapid motion of the plasma.

$$\frac{D\mathbf{U}}{Dt} = -\frac{\nabla p}{\rho} + g_r\hat{r} + \frac{\mathbf{J}\times\mathbf{B}}{\rho} + \mathbf{F}_{\text{corr}} + \rho^{-1}\mathbf{F}_{\text{visc}} + \zeta_{\text{shock}}(\nabla\nabla\cdot\mathbf{U}) \tag{2.2}$$

where p is the gas pressure, $\mathbf{J}$ is the current density and g_z is the constant solar gravity. The viscous force is written as

$$\rho^{-1}\mathbf{F}_{\text{visc}} = \nu\left(\nabla^2\mathbf{U} + \frac{1}{3}\nabla\nabla\cdot\mathbf{U} + 2\mathbf{S}\cdot\nabla\ln\rho\right) \tag{2.3}$$

where $\mathbf{S}$ represents the traceless rate-of-strain tensor and ν denotes the kinematic viscosity.

$$\mathrm{S}_{ij} = \frac{1}{2}\left(\frac{\partial \mathrm{U}_i}{\partial x_j} + \frac{\partial \mathrm{U}_j}{\partial x_i} - \frac{2}{3}\delta_{ij}\nabla.\mathbf{U}\right) \tag{2.4}$$

We do not account for the Coriolis force contribution, as the Rossby number at the solar surface is expected to be very large.

2.2.3 Induction equation

In our numerical framework, we model the evolution of magnetic fields, which are integral to the plasma environment, using the magnetic induction equation. This equation is derived from the

combination of Faraday's law and Ohm's law in electrodynamics. Rather than directly solving for the magnetic fields (**B**), our approach involves solving for the magnetic vector potentials **A** using a non-ideal form of the induction equation. This is a distinctive feature of the Pencil Code, which ensures the solenoidal nature of the magnetic field at the limits of computational precision. This method provides significant advantage in computation, as it eliminates the need for additional schemes for divergence cleaning (Powell, 1994; Dedner et al., 2002) required by the induction equation of magnetic fields to prevent numerical inconsistencies.

$$\frac{\partial \mathbf{A}}{\partial t} = \mathbf{U} \times \mathbf{B} - \eta \mu_0 \mathbf{J} + \nabla \Phi \tag{2.5}$$

Here η is the magnetic diffusivity and μ_0 is the permeability in vaccum. In addition to these terms, there is a scalar function, Φ, which arises due to gauge invariance. In our model, we use the Weyl gauge, where Φ is set to zero.

2.2.4 Energy conservation equation

To ensure energy conservation in our model, we incorporate an equation that governs the evolution of plasma temperature (T). This equation tracks how the thermal energy of individual plasma elements changes over time, accounting for various heating and cooling processes in the solar atmosphere. Our temperature evolution equation incorporates several key physical processes, (a) non-ideal heating mechanisms e.g., viscous heating which is proportional to S^2, intrinsic to non-ideal fluids and plasmas, ohmic heating which is proportional to J^2, arising from magnetized plasma flows, shock heating, included as part of viscous heating but modified by a large shock diffusion coefficient ($\zeta_{\rm shock}$) at localized shock fronts, (b) radiative cooling, represented by $\rho^2 \Lambda(T)$, where $\Lambda(T)$ is the temperature dependent cooling function, heating function by $\mathscr{H}$ and (c) thermal conduction ($q_{\rm cond}$).

$$\begin{aligned} \rho c_v T \frac{D \ln T}{Dt} = & -\rho c_v T (\gamma - 1) \boldsymbol{\nabla} \cdot \mathbf{U} + \boldsymbol{\nabla} \cdot q_{\rm cond} + \boldsymbol{\nabla} \cdot (\rho T \chi_t \boldsymbol{\nabla} \ln T) \\ & + 2\rho \nu \mathbf{S}^2 + \rho \zeta_{\rm shock} (\boldsymbol{\nabla} \cdot \mathbf{U})^2 + \mu_0 \eta \mathbf{j}^2 + \mathscr{H} - \rho^2 \Lambda(T) \end{aligned} \tag{2.6}$$

In this equation, γ is the adiabatic gas constant and $c_{\rm v}$ represents the specific heat capacity at constant volume. We will provide a more detailed explanation of the conductive heat flux in section 2.8.

2.2.5 The equation of state

The equation of state establishes a mathematical relationship between the key thermodynamic variables of the system, pressure (p), density (ρ) and temperature (T). In our model we use perfect gas equation where the pressure term can be expressed as

$$\nabla p = \rho c_s^2 \left(\frac{\nabla s}{c_p} + \nabla \ln p \right) \tag{2.7}$$

Here the sound speed when squared, is expressed as

$$c_s^2 = \gamma \frac{p}{\rho} = c_{s0}^2 \exp \left[\gamma \frac{s}{c_p} + (\gamma - 1) \ln \frac{\rho}{\rho_0} \right]$$

and $\gamma = c_p/c_v$ represents the ratio of specific heats, also known as adiabatic index. It is important to note that c_s^2 is directly proportional to the temperature and can be expressed as $c_s^2 = (\gamma - 1) c_p T$.

2.3 Numerical schemes

For solving the non-conservative form of the governing equations with high precision, our approach utilizes a finite difference scheme of the sixth order to perform spatial differentiation, as it is faster to compute and suitable for numerical simulation. The first and second derivative in radial, polar and azimuthal coordinates are denoted by

$$\left. \frac{\partial f}{\partial r} \right|_{r_i} \approx \frac{1}{60 h_r} \left(-fi - 3 + 9 f_{i-2} - 45 f_{i-1} + 45 f_{i+1} - 9 f_{i+2} + f_{i+3} \right) + \mathscr{O}(\delta x^6)$$

$$\left. \frac{\partial^2 f}{\partial r^2} \right|_{r_i} \approx \frac{1}{180 h_r^2} \left(2fi - 3 - 27 f_{i-2} + 270 f_{i-1} - 490 f_i + 270 f_{i+1} - 27 f_{i+2} + 2 f_{i+3} \right) + \mathscr{O}(\delta x^6)$$

$$\left. \frac{\partial f}{\partial \theta} \right|_{\theta_i} \approx \frac{1}{60 h_\theta} \left(-f_{i-3} + 9 f_{i-2} - 45 f_{i-1} + 45 f_{i+1} - 9 f_{i+2} + f_{i+3} \right) + \mathscr{O}(\delta x^6)$$

$$\left.\frac{\partial^2 f}{\partial \theta^2}\right|_{\theta_i} \approx \frac{1}{180h_\theta^2}\left(2f_{i-3}-27f_{i-2}+270f_{i-1}-490f_i+270f_{i+1}-27f_{i+2}+2f_{i+3}\right)+\mathscr{O}(\delta x^6)$$

$$\left.\frac{\partial f}{\partial \phi}\right|_{\phi_i} \approx \frac{1}{60h_\phi}\left(-f_{i-3}+9f_{i-2}-45f_{i-1}+45f_{i+1}-9f_{i+2}+f_{i+3}\right)+\mathscr{O}(\delta x^6)$$

$$\left.\frac{\partial^2 f}{\partial \phi^2}\right|_{\phi_i} \approx \frac{1}{180h_\phi^2}\left(2f_{i-3}-27f_{i-2}+270f_{i-1}-490f_i+270f_{i+1}-27f_{i+2}+2f_{i+3}\right)+\mathscr{O}(\delta x^6)$$

In this context, f_i represents the function value, derivatives are evaluated at the ith point on the respective grid. In our numerical setup $\mathscr{O}$ indicates the order of the error of the numerical method and h_r, h_θ and h_ϕ represents the resolution of the grid along the r, θ and ϕ direction. Higher-order differentiation operations, including second-order and above, are often necessary for accurately calculating the Lorentz force from the magnetic vector potential and to compute physical diffusion terms with precision. To maintain consistency in our approach and ensure a sixth-order truncation error throughout, we consistently apply sixth-order accurate schemes for all higher-order differentiation operations.

In dynamic numerical modeling, a crucial component is determining the effective time step for evolving the model stably. Our model incorporates various time steps associated with different physical mechanisms. The resultant time step is dictated by the shortest time scale associated to the fastest mechanism to resolve all physical processes (Brandenburg et al., 2020). For improved numerical stability, we use a dynamically adaptive time step approach instead of a fixed time step.

$$\delta t = \min\left(c_{\delta t}\frac{\delta x_{\min}}{U_{\max}}, c_{\delta t,\mathrm{U}}\frac{\delta x_{\min}^2}{D_{\max}}, c_{\delta t,\mathrm{s}}\frac{1}{H_{\max}}\right), \tag{2.8}$$

$$U_{\max} \equiv \max\left(|u|+\sqrt{c_s^2+v_\mathrm{A}^2}\right), \tag{2.9}$$

$$D_{\max} = \max(\nu, \gamma\chi, \eta, D), \tag{2.10}$$

$$H_{\max} = \max\left(\frac{2\nu\mathbf{S}^2+\zeta_{\mathrm{shock}}(\boldsymbol{\nabla}\cdot u)^2+\ldots}{c_v T}\right), \tag{2.11}$$

The terms $c_{\delta t}$, $c_{\delta t,\mathrm{U}}$, and $c_{\delta t,\mathrm{s}}$ represent Courant–Friedrichs–Lewy (CFL) coefficients for advection, diffusion, and thermal processes (heating or cooling), respectively. These coefficients

typically fall within the range of 0.10 to 0.25. The variable $D_{\max}$ denotes the highest value among the various diffusion coefficients present in the system.

We employ a 3rd-order explicit Runge-Kutta method with internal sub-steps for integration. This higher-order approach minimizes numerical errors in both the solution's amplitude and phase. While alternatives like super time steps and implicit methods are available, they can be memory-intensive and don't always ensure solution convergence. To optimize memory usage, we implement the $2N$ schemes, which only need to store two sets of variables in memory (Williamson, 1980).

2.4 Shock viscosity

Shocks are frequently observed in solar phenomena, occurring when plasma flows surpass the medium's characteristic speed, such as the sound or Alfvén speed. These shocks can originate from the boundaries between granules where they diverge from each other, MHD waves propagating through the stratified atmospheric layers, or explosive events like coronal mass ejections and magnetic reconnection regions.

In fluids where particle collisions dominate, the shock front's thickness is comparable to the mean free path between particles (Zel'dovich & Raizer, 1967). However, in plasmas where collisions are rare, this thickness can be much smaller (Petschek, 1958; Buneman, 1964). The MHD approximation struggles to capture such fine scales. Studies indicates that viscous diffusion influences the shock front's thickness (Orta et al., 2003). To address this within the MHD framework, we introduce a localized enhanced diffusion through explicit shock viscosity (ζ_{shock}). This approach allows us to detect and resolve the shock front, even when using the MHD approximation (Ballai et al., 2007).

We define shock diffusion, ζ_{shock} as

$$\zeta_{\text{shock}} = c_{\text{shock}} \langle \text{Max3} \left[(-\nabla \cdot \mathbf{U}) + \right] \rangle \min \left(dx^2, dy^2, dz^2 \right) \tag{2.12}$$

where, c_{shock} is a dimensionless parameter representing the strength of the diffusion, and dx, dy, and dz are the grid resolutions in each spatial direction. This explicit shock viscosity not only increases the thickness of the shock front but also reduces numerical oscillations across it. To

maintain consistency, we account for this enhanced diffusion caused by shocks is incorporated into in the mass, momentum, induction, and energy equations.

2.5 Hyperdiffusion

Hyperdiffusion is a numerical technique used to dampen instabilities at the smallest scales of the computational grid. In our model, we incorporate hyperdiffusion coefficients alongside explicit physical diffusion terms in all the dynamical equations. To generalize this approach, we can express the divergence if the flux $\mathbf{J}$ of any physical quantity ψ as

$$\frac{\partial \psi}{\partial t} + \boldsymbol{\nabla} \cdot \mathbf{J} = 0 \tag{2.13}$$

Higher-order diffusion processes, specifically, for a 2n-th order isotropic diffusion, we can express the n-th order current density as

$$\mathbf{J}^{(\mathrm{n})} = (-1)^{\mathrm{n}} D^{(\mathrm{n})} \boldsymbol{\nabla}^{2\mathrm{n}-1} \psi, \tag{2.14}$$

The equation describes diffusion processes of different orders. For n = 3, we obtain a sixth-order hyperdiffusion equation. In both cases, $D^{(\mathrm{n})}$ represents the strength of the diffusion process for the given order. The sixth-order hyperdiffusion (n = 3) is particularly useful in numerical simulations for suppressing small-scale instabilities without significantly affecting larger scales. Thus,

$$\frac{\partial \psi}{\partial t} = D^{(3)} \nabla^6 \psi \tag{2.15}$$

The equation shows that for sixth-order hyperdiffusion. This means hyperdiffusion is most effective at high wavenumbers (k) to smooth out sharp changes in physical quantities. While theoretically any higher order of hyperdiffusion could be used, practical limitations arise from the size of the numerical stencil in the computational domain. In our work we use hyperdiffion related to mesh.

2.6 Hyperviscosity

Hyperviscosity, like hyperdiffusion, is an artificial numerical technique used to suppress instabilities at the smallest grid scales. In our model, we incorporate both hyperviscosity coefficients and explicit physical viscosity terms in all dynamical equations. A key difference from standard viscosity is that the momentum flux due to viscosity is proportional to the rate-of-strain tensor, rather than the velocity gradient.

This restricts the viscous aceleration to the simplified form $\nu\nabla^2\mathbf{U}$ only under the conditions of incomprehensibility and constant dynamic viscosity $\mu = \nu\rho$.

In the most general formulation, the viscous acceleration can be expressed as

$$f_{\text{visc}}^{(hyper)} = \rho^{-1}\nabla\cdot(2\rho\nu\mathbf{S}) \tag{2.16}$$

To implement hyperviscosity, we need to modify the standard viscous force equation by replacing the typical rate-of-strain tensor with a higher-order version

$$f_{\text{visc}}^{(hyper)} = \rho^{-1}\nabla\cdot(2\rho\nu_n\mathbf{S}^{(n)}) \tag{2.17}$$

where the rate of strain tensor of n^{th}-order is

$$\mathbf{S}^{(n)} = (-\nabla^2)^{n-1}\mathbf{S} \tag{2.18}$$

For the $n = 3$ it becomes

$$S_{ij}^{(3)} = \frac{1}{2}\left(\frac{\partial^5 u_j}{\partial x_i^5} + \frac{\partial^4}{\partial x_i^4}\left(\frac{\partial u_i}{\partial x_j}\right) - \frac{1}{3}\frac{\partial^4}{\partial x_i^4}(\nabla\cdot\mathbf{U})\right) \tag{2.19}$$

Plugging it into Equation 2.17, and assuming $\mu_3 = \rho\nu_3 =$ constant we get

$$f_{\text{visc}}^{(hyper)} = \nu_3\left(\nabla^6\mathbf{U} + \frac{1}{3}\nabla^4(\nabla(\nabla\cdot\mathbf{U}))\right) \tag{2.20}$$

For $\nu_3 =$ constant, we have to take derivative of density as well. Thus,

$$f_{\text{visc}}^{(hyper)} = \nu_3\left(\nabla^6\mathbf{U} + \frac{1}{3}\nabla^4(\nabla(\nabla\cdot\mathbf{U})) + 2\mathbf{S}^{(3)}\cdot\nabla\ln\rho\right) \tag{2.21}$$

Here we use hypervisocity in a mesh independent way.

2.7 Semirelativistic Boris correction

The analysis of stellar interiors typically employs non-relativistic MHD, which omits the displacement current (J_d) from Ampére's Law. This simplification is valid because plasma movements in these regions are much slower than light speed. However, in the low-density corona, the Alfvén speed can approach relativistic levels above strong magnetic structures (Chatterjee & Fan, 2013; Rempel, 2016). In these scenarios, we can't ignore the displacement current. To address this, we use a hybrid approach called the Semi-relativistic Boris correction. We include the displacement current which is proportional to the $\partial \mathbf{E}/\partial t$ and treat other terms non-relativistically when calculating the Lorentz force. We artificially decrease the speed of light to avoid the computational challenge of extremely small time steps associated with Alfvén wave crossing, which typically hinder long-term simulations of solar coronal models. We implement this correction as described by Gombosi et al. (2002). Using Faraday's law with the Equation 2.5, we get,

$$\frac{1}{\mu_0 c^2}\mathbf{B}\times\frac{\partial \mathbf{E}}{\partial t} = \rho\left(-\frac{v_A^2}{c^2}\mathbf{I}+\frac{v_A^2}{c^2}\mathbf{bb}\right)\cdot\frac{\partial \mathbf{U}}{\partial t}+\left[\frac{(\nabla\times\mathbf{E})\times\mathbf{U}}{\mu_0\rho c^2}\right]\times\mathbf{B} \tag{2.22}$$

Here $\mathbf{I}$ represents the identity matrix and $\mathbf{b}$ denotes the unit vector aligned $\mathbf{B}$. v_A is the Alfvén speed. After incorporating the modification, which includes the semi-relativistic corrections, the equation becomes

$$\left[\mathbf{I}+\frac{v_A^2}{c^2}(\mathbf{I}-\mathbf{bb})\right]\cdot\frac{\partial \mathbf{U}}{\partial t} = -(\mathbf{U}\cdot\nabla)\mathbf{U}-\frac{\nabla p}{\rho}+\mathbf{g}+\left[\frac{(\nabla\times\mathbf{B})}{\mu_0\rho}+\frac{(\nabla\times\mathbf{E})\times\mathbf{U}}{\mu_0\rho c^2}\right]\times\mathbf{B}. \tag{2.23}$$

The modified equation introduces a new matrix in Equation 2.23 increases the effective inertia of plasma moving perpendicular to $\mathbf{B}$, while it leaves the plasma motion parallel to the $\mathbf{B}$ unchanged. On the right-hand side of the equation, there are two terms within square brackets. By comparing these terms, we find that their ratio is approximately $(|\mathbf{U}|/c)^2$, where $|\mathbf{U}|$ is the magnitude of the velocity and c is the speed of light. Since $|\mathbf{U}|$ is typically smaller than c in our model, this ratio is very small. Therefore, we can safely neglect the term that is second-order in $(|\mathbf{U}|/c)$, as it's significantly smaller than the other terms in the equation.

$$\frac{|(\nabla\times\mathbf{E})\times\mathbf{U}|}{c^2|\nabla\times\mathbf{B}|}\sim\frac{|\mathbf{U}|^2}{c^2}\ll 1. \tag{2.24}$$

We now take the inverse of the "enhanced inertia" matrix and express it after defining $\beta_A = \sqrt{v_A^2/c^2}$

$$\left[\mathbf{I}+\beta_A^2\left(\mathbf{I}-\mathbf{bb}\right)\right]^{-1} = \mathbf{I} - \frac{\beta_A^2}{1+\beta_A^2}\left[\mathbf{I}-\frac{\mathbf{bb}}{1+\beta_A^2}\right]. \tag{2.25}$$

With this correction term of the equation 2.2 becomes

$$\mathbf{F}_{\text{corr}} = \frac{\beta_A^2}{1+\beta_A^2}\left[\mathbf{I}-\frac{\mathbf{bb}}{1+\beta_A^2}\right]\left[\mathbf{U}\cdot\boldsymbol{\nabla}\mathbf{U}+\frac{\boldsymbol{\nabla}p}{\rho}-\mathbf{g}-\frac{(\boldsymbol{\nabla}\times\mathbf{B})\times\mathbf{B}}{\mu_0\rho}\right]. \tag{2.26}$$

If Alfvén speed v_A is much smaller than the speed of light c, such as in the solar convective or photospheric layers, the correction term $\mathbf{F}_{\text{corr}}$ becomes negligible, allowing us to use the original acceleration equation without semi-relativistic effects. However, in solar corona, where v_A is comparable to or greater than c, the correction term becomes significant and influences plasma motion. When this happens, the characteristic Alfvén speed needs to be adjusted to $v_A/\sqrt{1+\beta_A^2}$.

We artificially lower the speed of light to $c = \max[c_s, 5|U|_{\max}]$ in the solar atmosphere, where c_s is the sound speed. This adjustment ensures that the Alfvén speed ratio β_A exceeds unity. This leads to a notable impact of the correction term $\mathbf{F}_{\text{corr}}$ on plasma dynamics. With a reduced speed of light, the effective Alfvén speed decreases, allowing for larger time steps in the integration of motion equations. This approximation has proven stable in various different models and has the advantage of requiring less diffusion, making it possible to use relatively coarse grids while still obtaining stable results.

2.8 Anisotropic thermal conductivity

Energetic solar events, such as solar flares and coronal mass ejections (CMEs), release significant magnetic energy into the solar corona. This energy is partly converted into internal plasma energy through efficient thermal conduction. This process is crucial for energy loss in the corona and for heating the chromosphere. Due to the structured nature of the magnetic fields in the atmosphere, thermal conduction is highly directional. In a plasma environment, heat primarily moves along the magnetic fields because thermal conduction is much greater in this direction compared to perpendicular to the fields, where the heat flux is limited to the scale of the Larmor radius (Braginskii, 1965; Priest, 2014). The parallel thermal conductivity,

denoted as $k_{\parallel}$, is proportional to $T^{5/2}$ as modeled by Spitzer (Spitzer, 1962).

$$\frac{k_{\parallel}}{k_{\rm sp}} = T^{5/2}\left[\frac{\rm erg}{\rm cm\cdot s\cdot K^{7/2}}\right] \tag{2.27}$$

The constant $k_{\rm sp} = 10^{-6}$. The relationship between the parallel ($k_{\parallel}$) and the perpendicular ($k_{\perp}$) component of the Spitzer conductivity relative to the magnetic field can be written as (Priest, 2014),

$$\frac{k_{\perp}}{k_{\parallel}} = 2\times 10^{-45}\frac{n^2}{\rm B^2 T^3} \tag{2.28}$$

Here all the parameters are in cgs unit. In the solar corona, temperatures can reach up to 10^6 K and number densities as low as $10^8 cm^{-3}$. Under these conditions, thermal diffusion which is parallel to the magnetic field becomes extremely high. Consequently, the time scale associated to the diffusion, becomes extremely small. To address the computational challenges posed by these tiny thermal diffusion time scales, several approaches have been developed. In our model, we use the hyperbolic (or non-Fickian) transport equation for heat flux, also used by other models (Rempel, 2016; Fan, 2017; Chatterjee, 2020; Warnecke & Bingert, 2020). This method helps avoid the constraints imposed by the extremely small thermal diffusion time scales on the overall system dynamics.

$$\frac{\partial q_{\rm cond}}{\partial t} = -\frac{q_{\rm cond}-q_{\rm sp}}{\tau_{sp}} + \beta({\rm d}r\cdot\boldsymbol{\nabla})^6 q_{\rm cond} \tag{2.29}$$

where,

$$q_{\rm sp} = k_0 T^{5/2}\hat{b}(\hat{b}\cdot\boldsymbol{\nabla}T),$$

Here $q_{\rm cond}$ represents the solution of the equation 2.29 and $q_{\rm sp}$ denotes the Spitzer heat flux. The unit vector $\hat{b}$ is along $\mathbf{B}$, while the hyperdiffusion parameter β is set at $1{\rm s}^{-1}$. The term dr refers to the grid spacings $[{\rm dx, dy, dz}]$. To prevent excessive diffusion speeds, we apply a factor $f_{\rm sp} = 0.1$ to limit the Spitzer diffusion speed ($u_{\rm sp}$),

$$u_{\rm sp} = \frac{k_{sp}T^{5/2}}{\rho c_V} > f_{\rm sp} c_0 \delta x,$$

where δx represents the maximum grid spacing in the numerical grid. The key advantage of using the hyperbolic transport equation of heat transfer is the significant improvement in temporal resolution over then standard parabolic heat transfer approach.

2.9 Summary

In this chapter, we provide an overview of the Pencil-Code utilized in this thesis. Various initial and boundary conditions are employed for different setups, which are detailed in the respective chapters. The higher-order finite difference scheme is chosen for its computational efficiency and suitability for the numerical problems addressed by this thesis. Additionally, we implement several numerical schemes to ensure the simulations are as physically accurate as possible, such as shock diffusivity, hyperdiffusion, and hyperviscosity. We also employ the semi-relativistic Boris correction and utilize the hyperbolic diffusion equation approach, rather than directly solving the Spitzer conduction equation. To analyze the simulated data from our numerical simulations, we developed several IDL routines and also used Paraview [1] for further visualization.

[1] https://www.paraview.org/

3

Instruments and Observational Data

3.1 Introduction

As described in the introduction, the objective of this thesis is to understand the solar origin of CMEs and its evolution in lower corona. Therefore, we use observational data obtained from different space based observatories which can capture the initiation and evolution close to Sun. This thesis work mostly uses the data obtained from the space based observatories which includes Solar Dynamic Observatory (SDO; Pesnell et al. 2012), Solar Terrestrial Relations Observatory (STEREO; Kaiser et al. 2008) and GOES.

To understand the source region characteristics of CMEs, it is essential to image the different atmospheric layers of the Sun with high temporal and spatial resolution. For this purpose, we use the unprecedented multi-wavelength observations from the Solar Dynamics Observatory (SDO). The source active regions of CMEs consist of complex magnetic structures extending from deep sub-photospheric layers, crossing through the photosphere, and reaching

coronal heights. The velocity flows at the sub-photospheric layers govern the evolution of the photospheric magnetic field, which in turn shapes the dynamics of the solar corona. Therefore, to understand the conditions of photospheric field evolution leading to CME eruptions, we use the high-cadence, high-spatial-resolution observations of the vector magnetic field at photospheric heights obtained from SDO. Observations of the photospheric magnetic field also allow us to characterize the magnetic topology of the source region associated with flares. To capture the lower corona evolution of CMEs, we leverage the multi-vantage point observations of CMEs in white light and their lower coronal signatures in EUV passbands from the twin spacecraft STEREO A and B. Additionally, we use GOES data to understand the start, peak, and end times of flares. In this chapter, we provide a brief description of the aforementioned instruments along with details for the data and techniques.

3.2 The Solar Dynamic Observatory (SDO)

The Solar Dynamic Observatory (SDO; Pesnell et al. 2012) is the inaugural space mission under NASA's Living with a Star (LWS) program. Developed at NASA's Goddard Space Flight Center, SDO was launched on February 11, 2010. Its primary aim is to understand the generation of the Sun's magnetic field and how this energy is transformed and released into the heliosphere and geo-space in the form of solar wind, energetic particles, and variations in solar irradiance. SDO includes three key instruments: the Atmospheric Imaging Assembly (AIA; Lemen et al. 2012), the Helioseismic and Magnetic Imager (HMI; Schou et al. 2012), and the Extreme Ultraviolet Variability Experiment (EVE; Woods et al. 2012). This thesis makes extensive use of data from both the HMI and AIA instruments.

SDO maintains a geosynchronous orbit around Earth, allowing for continuous monitoring of the Sun. The AIA captures high-resolution images of the solar corona across multiple wavelengths, enabling the study of the Sun's outer atmosphere and its dynamic processes. The HMI focuses on the Sun's magnetic field and internal structure through helioseismology, offering insights into solar oscillations and magnetic activities. The EVE measures the Sun's extreme ultraviolet (EUV) spectral irradiance, which affects Earth's ionosphere and thermosphere.

The continuous monitoring by SDO has greatly enhanced our understanding of various solar phenomena, including solar flares, coronal mass ejections (CMEs), and the solar magnetic field.

The data provided by SDO are invaluable for studying the mechanisms behind these events, their origins, and their effects on space weather. One of SDO's most significant contributions is its near-real-time data on solar activity, which is crucial for space weather forecasting and for protecting satellites, power grids, communication systems, and astronauts from the adverse effects of solar storms.

3.2.1 Atmospheric Imaging Assembly (AIA)

The Atmospheric Imaging Assembly (AIA; Lemen et al. 2012) is a crucial instrument aboard NASA's Solar Dynamics Observatory (SDO). It provides continuous, high-resolution, full-disk images of the Sun's atmosphere in multiple wavelengths with unprecedented accuracy. It is capable of producing multiple snapshots of high-resolution full-disk images of the Sun with 0.6" pixel^{-1} spatial sampling and 12-second temporal cadence. The AIA consists of four telescopes that capture images in ten different wavelength channels, each sensitive to various temperatures and heights in the solar atmosphere. Table 3.1 provides a detail of the different observing channels in AIA and the corresponding regions of solar atmosphere with different characteristic temperatures.

In this thesis, we have used the AIA images obtained in 94 Å, 193 Å and 1600 Å passbands. AIA 94 Åimages represent the hot solar corona at a temperature of six million Kelvin (emission from Fe XVIII). AIA 193 Å images capture the solar corona at a temperature of one million Kelvin (emission from Fe XII) as well as the hot material of a solar flare at a temperature of twenty million Kelvin (emission from Fe XXIV).The images serves valuable information for post flare loops. These loops contain hot plasma resulting from chromospheric evaporation (Doschek & Warren, 2005). AIA 1600 Å (emission from C IV) images captures emission from C IV, represents lower chromospheric region. This area is known as the transition region of the solar atmosphere. These images are crucial for identifying the precise locations of the flare ribbons. These ribbons are thought to form when accelerated particles, traveling downward from the reconnection site along the reconnected magnetic field lines, collide with the dense chromosphere, causing plasma heating (Priest & Forbes, 2002).

AIA's multi-wavelength capability allows it to observe a wide range of solar phenomena, including solar flares, coronal mass ejections (CMEs), sunspots, active regions, coronal loops, and plumes. For instance, AIA captures the rapid energy release and heating associated with solar flares, aiding in understanding their formation and evolution. It also monitors the solar

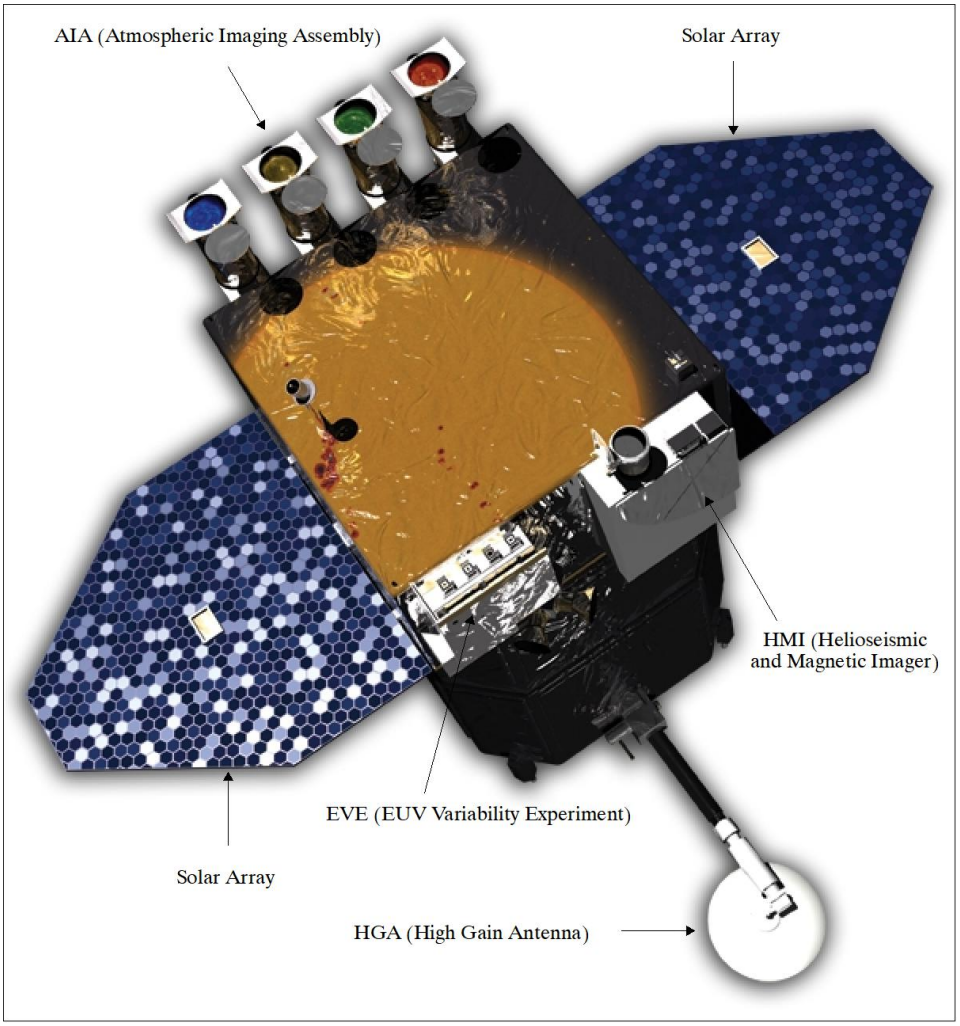

Fig. 3.1 Solar Dynamics Observatory and its different instruments.

corona to track the initiation and propagation of CMEs, which are significant drivers of space weather.

Wavelength	Primary ion(s)	Region of atmosphere	Charcistic log(T)
4500	continum	photopshere	3.7
1700	continum	photosphere	3.7
304	He II	chromosphere, transition region	4.7
1600	C IV + continum	transition region, upper photosphere	5.0
171	Fe IX	quiet corona, upper transition region	5.8
193	Fe XII, XXIV	corona and hot flare plasma	6.2, 7.3
211	Fe XIV	active-region corona	6.3
335	Fe XVI	active-region corona	6.4
94	Fe XVIII	flaring corona	6.8
131	Fe VIII, XXI	transition region, flaring corona	5.6, 7.0

Table 3.1 Different channels of AIA centered on specific lines and corresponding regions of solar atmosphere with different characteristic temperatures (Lemen et al. 2012).

3.2.2 The Helioseismic and Magnetic Imager (HMI)

The Helioseismic and Magnetic Imager (HMI; (Schou et al., 2012)) onboard the SDO is designed to study the oscillations and magnetic field at solar photopshere. HMI provides critical data for understanding solar variability and its effects on the solar system. HMI observed the Sun in the Fe I 6173 Å absorption line with resolution of 1". It provides full-disk observations of Doppler velocity, intensity and both the line-of-sight and vector magnetogram of solar photosphere. HMI comprises of a refracting telescope of 14 cm clear aperture, a polarization selector, an image stabilization system,The equipment consists of a precisely adjustable narrow-band filter, coupled with a pair of high-resolution CCD cameras. Each camera features a 4096 $\times$ 4096 pixel sensor, integrated mechanical shutters, and dedicated control electronics.

Our research extensively utilized the HMI vector magnetogram series from the Space weather HMI Active Region Patches (SHARP) version,(SHARP; Turmon et al. 2010a). This data has a spatial resolution of 0.5 arcseconds per pixel and a temporal cadence of 12 minutes. The Stokes parameters I, Q, U, and V were obtained from filtergrams of six polarization

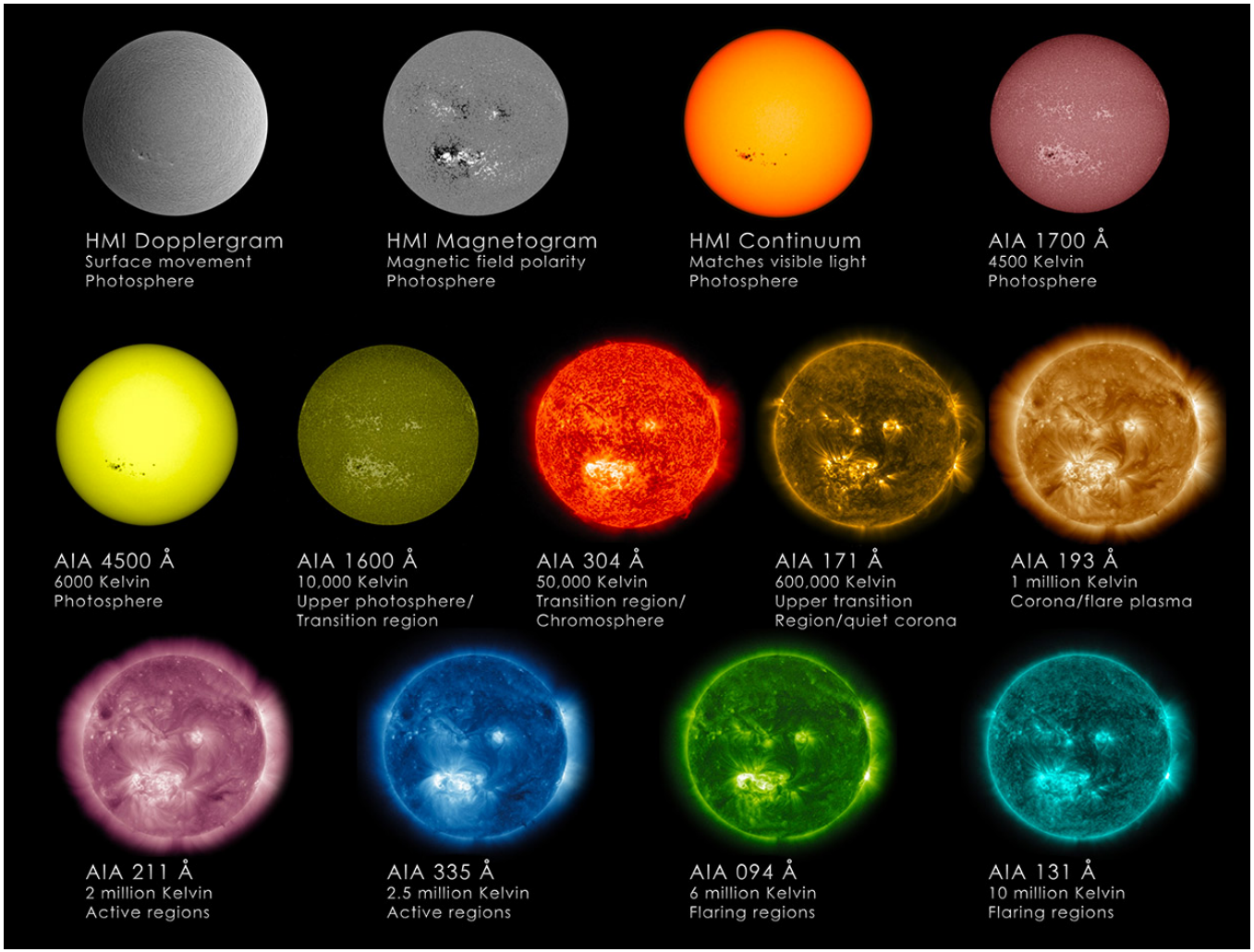

Fig. 3.2 NASA's Solar Dynamics Observatory (SDO) has captured a series of solar images, combined here into a collage. This collection demonstrates how observing the Sun at different wavelengths highlights various aspects of its surface and atmosphere. Additionally, the collage incorporates images from other SDO instruments, which provide data on magnetic fields and Doppler effects associated with the Sun.

states at six wavelengths centered on the Fe I 6173 Å spectral line. These parameters were then inverted using the Very Fast Inversion of the Stokes Algorithm (VFISV) code (Borrero et al., 2011), to derive the vector magnetic-field components in the photosphere. The VFISV is a Milne-Eddington spectral line inversion code used to infer the vector magnetic field of the solar photosphere from HMI Stokes measurements. It employs a Levenberg–Marquardt least-squares minimization to iteratively adjust model parameters, comparing synthetic Stokes profiles to observations until the fit meets convergence criteria. To resolve the inherent 180-degree ambiguity in the azimuthal field component, we applied the minimum energy method (Metcalf, 1994; Leka et al., 2009). Subsequently, we performed a coordinate transformation to remap the vector fields onto the Lambert cylindrical equal area projection. In the final step, we converted the vector fields into heliocentric spherical coordinates.

HMI's primary contributions are mapping magnetic fields associated with sunspots, active regions, and flare formations, aiding in space weather prediction.

3.3 STEREO

The NASA's twin spacecraft STEREO A & B (Kaiser et al., 2008) were launched in 2006 to study the initiation of CMEs and their propagation in the inner heliosphere. STEREO-A (Ahead) and STEREO-B (Behind) satellites are positioned in orbits that lead and trail Earth, respectively, providing unique and simultaneous three-dimensional views of the Sun and its dynamic activity from different vantage points in space. This stereoscopic vision is invaluable for studying the spatial structure and evolution of solar phenomena, offering a more complete understanding of their behavior and potential impact on Earth. Each STEREO spacecraft has identical instruments which provide the remote sensing observations in optical and radio wavelengths as well as measure the in-situ properties of particles and fields. These instruments can be categorized in four different measurement packages which include SECCHI, IMPACT, PLASTIC ands S/Waves. The Suite of instruments in SECCHI (Howard et al., 2008) package comprises of an Extreme Ultra Violet Imager (EUVI), two white light coronagraphs (COR1 and COR2) and two white light heliosphric imagers (HI1 and HI2) which together can image a CME from its eruption in the corona out to 1 AU. A brief description of these instruments are discussed as follows.

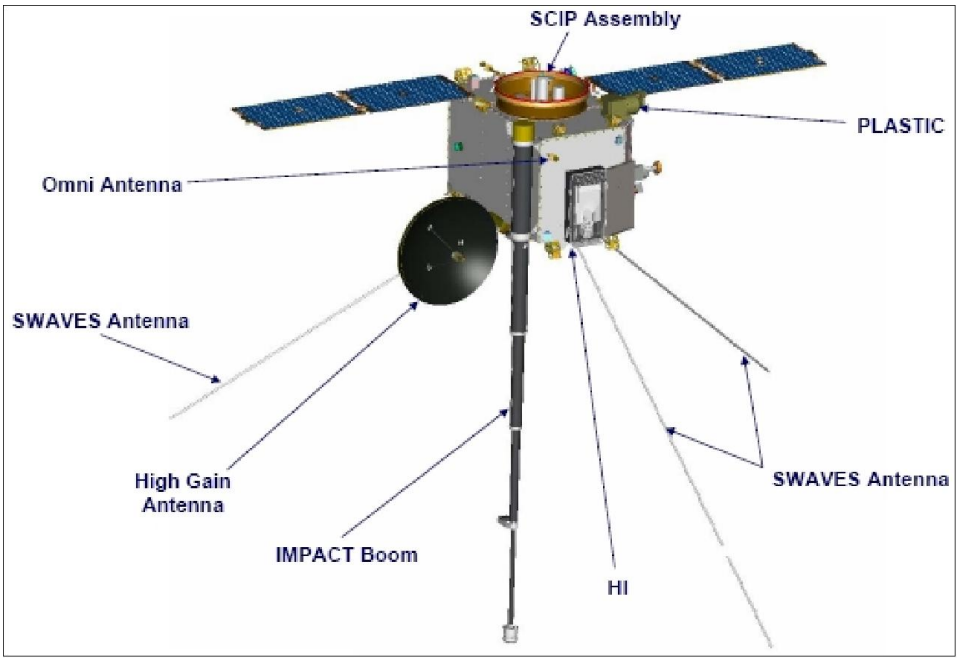

Fig. 3.3 Solar TErrestrial RElations Observatory and its different instruments.

3.3.1 Extreme Ultra Violet Imager (EUVI)

The Extreme Ultraviolet Imager (EUVI) is a key instrument within the Sun-Earth Connection Coronal and Heliospheric Investigation (SECCHI) suite on board the Solar and Terrestrial Relations Observatory (STEREO) spacecraft. EUVI is designed to observe the chromosphere and low corona in extreme ultraviolet (EUV) wavelengths, providing crucial insights into the dynamic processes occurring in the solar corona. It is a small, normal-incidence telescope with thin metal filters, multilayer coated mirrors, and a back-thinned CCD detector. The circular full sun field-of-view of EUVI extends up to $1.7R_{\odot}$ and it images with a spatial sampling of 1.6" pixel^{-1}.

EUVI captures images of the Sun in four different EUV emission lines which include He II 30.4 nm, Fe IX 17.1 nm, Fe XII 19.5 nm, Fe XV 28.4 nm. This multi-wavelength approach allows scientists to study various layers of the corona, from the relatively cool transition region to the hot, outermost parts of the corona. By monitoring these regions, EUVI helps researchers understand the heating mechanisms of the corona, the origins of solar flares, and the initial stages of coronal mass ejections (CMEs).

3.3.2 COR1 Coronagraph

The COR1 instrument is a vital component of the SECCHI suite onboard the STEREO spacecraft. COR1 is developed to image the faint solar corona visible due to the scattered light from the much brighter solar photosphere. The instrument uses an occulting disk to create an artificial eclipse, allowing the outer layers of the Sun to be imaged without the overwhelming glare of the solar disk. COR1 is a classic Lyot internally occulted refractive coronagraph (Lyot, 1939) designed to observe the innermost regions of the Sun's corona, specifically targeting the area from 1.4 to $4R_{\odot}$ in white light. COR1 provides the images with a spatial sampling of 7.5" pixel^{-1} and temporal cadence of 8 min. By blocking the intense light from the Sun's surface, COR1 enables the observation of the fainter coronal structures. This capability is crucial for studying the early stages of CME development and understanding the dynamic processes occurring in the Sun's atmosphere.

3.3.3 COR2 Coronagraph

Unlike COR1, COR2 is white-light coronagraph designed to observe the solar corona, the outermost part of the Sun's atmosphere, in unprecedented detail. COR2 is an extremely occulted Lyot coronagraph which can image the solar corona from 2.5 to $15R_{\odot}$. In an extrememly occulted coronagraph, the objective lens is shielded from direct sunlight which reduces the stray light level as compared to COR1 and makes it possible to observe further distances from the Sun. Cor2 provides the images with temporal cadence of 15 min and spatial sampling of 14.7" pixel^{-1}.

3.4 GOES

The Geostationary Operational Environmental Satellite (GOES) series is a critical component of the United States' weather monitoring and forecasting infrastructure. Operated by the National Oceanic and Atmospheric Administration (NOAA), these satellites provide real-time data on atmospheric, oceanic, and space weather phenomena. Positioned in a geostationary orbit, approximately 35,800 kilometers (22,300 miles) above the equator, each GOES satellite remains fixed over a specific point on Earth's surface, enabling continuous observation of the same region.

The GOES satellites are equipped with advanced instruments that monitor a wide range of environmental variables. These include the Advanced Baseline Imager (ABI) for detailed imaging of weather patterns, the Geostationary Lightning Mapper (GLM) for detecting lightning activity, and space weather sensors that monitor solar activity and its impact on the Earth's magnetosphere. This comprehensive data collection is vital for weather prediction, climate research, and natural disaster response.

GOES satellites have a storied history, beginning with the launch of GOES-1 in 1975. The current series, known as the GOES-R series, includes satellites such as GOES-16 (GOES-East) and GOES-17 (GOES-West), which offer enhanced capabilities compared to their predecessors. These improvements include higher resolution imagery, faster data transmission, and more accurate monitoring of atmospheric conditions.

3.5 Summary

In this chapter, we provide an overview of the data sources utilized in this thesis. To study the evolution of the photospheric magnetic field and its role in solar explosive events like flares and CMEs, we employed vector magnetogram data from HMI/SDO. Observations from AIA/SDO in the 1600 Å bandpass were used to image post-flare loops and flare ribbons. To understand the evolution of CMEs in the lower corona, we utilized multi-vantage point observations from the COR1 and COR2 instruments onboard STEREO A and B, tracking a prominence-associated CME during its evolution in the lower corona. For initial evolution, we combined these EUV observations with white light observations from STEREO A and B. We also used X-ray flux data obtained from the GOES spacecraft. For analyzing the observational data from these space-based observatories, we developed several routines in IDL and utilized available SSW [1] packages.

[1] https://soho.nascom.nasa.gov/solarsoft/

4

Photospheric Lorentz force changes in eruptive and confined solar flares

4.1 Introduction

Solar flares and Coronal Mass Ejections (CMEs) are considered the two most violent and energetic phenomena occurring in the solar atmosphere due to the sudden release of energy. A typical flare is recognized by a quick increase in light emission in a broad range of the electromagnetic spectrum that affects the solar atmosphere, while a CME consists of plasma and high-energy particles that are expelled from the Sun. They are responsible for significant space weather impacts on Earth (Siscoe, 2000; Baker et al., 2004; Chen, 2017; Green et al., 2018). Therefore, understanding the source region characteristics of these energetic solar events has become one of the most important goals of space science research. A solar flare in relation

to CMEs is classified into two types: eruptive and confined (Moore et al., 2001). Eruptive flares are associated with CMEs, while confined flares do not have associated CMEs.

Previous observations have shown that flares and CMEs are different manifestations of the same energy-release process (Harrison, 2003; Zhang et al., 2001). Moreover, Zhang et al. (2001) have shown that the phase of rapid acceleration of CMEs in the inner corona is temporarily correlated with the rise time of the associated soft X-ray flares. In spite of the intrinsic correlation between flares and CMEs, observations have shown that not all flares are associated with CMEs (Andrews, 2003; Yashiro et al., 2005; Yashiro & Gopalswamy, 2009; Webb & Howard, 2012; Youssef, 2012). Active regions (ARs) with complex topology are the primary sources of large flares and most energetic CMEs (Zirin & Liggett, 1987; Sammis et al., 2000; Yang et al., 2017). During a flaring event, the magnetic field reorganizes rapidly in the corona owing to the low Alfvén travel time, leading to the eruption of magnetic flux rope and the subsequent formation of post-flare loops beneath the current sheet, in accordance with the standard flare model (Carmichael, 1964; Hirayama, 1974; Sturrock, 1966; Kopp & Pneuman, 1976; Shibata & Magara, 2011). The flaring process converts the magnetic free energy into kinetic, thermal energy and non-thermal energy that accelerates particles. Although the photosphere is much denser than the corona, the photospheric magnetic field can respond to sudden coronal restructuring during flaring events (Wang & Liu, 2015; Aulanier, 2016; Toriumi & Wang, 2019). Counter-intuitively, observations have shown that the photospheric magnetic field does experience significant changes during flares (Wang & Liu, 2015; Toriumi & Wang, 2019). Since there is no practical or direct method to measure the vector magnetic field in the coronal volume, it is challenging to quantitatively investigate the temporal evolution of non-potential parameters (e.g., magnetic free energy) (Wiegelmann et al., 2014). Therefore, the temporal or spatial evolution of parameters in the source region that can only be estimated from the photospheric (Petrie & Sudol, 2010) and chromospheric (Kleint, 2017) magnetic field (e.g., the change in the net Lorentz force) becomes a major probe to study the changes associated with the flare. Hudson et al. (2008) were the first to suggest that photospheric magnetic fields should become more horizontal after the flare due to the effect of vertical Lorentz forces on the solar surface. Developing this model further, Fisher et al. (2012) gave a practical approach to calculate the net Lorentz force acting on the solar photosphere. They found an increase in the horizontal magnetic field (B_h), particularly around the polarity inversion line (PIL), and an associated large and abrupt downward change in the vertical Lorentz force. Previous studies have also found that large eruptive flares are associated with a sudden downward change in the Lorentz force (Petrie & Sudol, 2010; Petrie, 2012). In contrast to B_h, the vertical magnetic field (B_z) varies much less during the flare without a clear pattern (Sun et al., 2017). On the other hand, the sunspot area weighted horizontal gradient of the vertical magnetic field is found to

follow a distinct pattern before a flare, providing potential predictive capability (Korsós et al., 2015). This behavior of the weighted gradient is also marked by the approaching–receding motion of the barycenters of opposite polarities before the flare. Sarkar & Srivastava (2018) compared the magnitude of changes in the horizontal magnetic field (B_h) and the net vertical Lorentz force associated with eruptive and confined flares occurred in a same active region (AR). They reported that the flare associated changes in magnetic parameters are larger for eruptive flares than for confined ones. Extending the study to large recurrent flares, Sarkar et al. (2019) found that the change in net vertical Lorentz force acts as an excellent proxy to predict the recurrent large flaring events from a same AR. Vasantharaju et al. (2022) reported that the vertical Lorentz force changes during flares near PILs correlate well with the flare strength. However, no clear classification of the association of flares with CMEs has been made to statistically distinguish them by the net change in Lorentz force.

We now have evidence of rapid and permanent changes in the longitudinal and transverse magnetic fields linked to solar flares in the photosphere thanks to the availability of high-cadence photospheric vector magnetograms from the ground- and space-based telescopes (Sudol & Harvey, 2005; Petrie & Sudol, 2010; Wang et al., 2012a; Gosain, 2012; Sun et al., 2017; Castellanos Durán et al., 2018; Petrie, 2019; Liu et al., 2022; Kazachenko et al., 2022; Kazachenko, 2023).

The magnetic implosion conjecture is frequently used to explain observational evidence of the rise in the horizontal component of the magnetic field in the solar atmosphere (Hudson, 2000). It states that in a low plasma β environment, the coronal loops must contract during a transient event, such as a flare or a CME, in order to lower the magnetic energy. According to Hudson et al. (2008) and Fisher et al. (2012), the release of free magnetic energy should be accompanied by a decrease in the magnetic pressure and volume. A MHD wave that propagates downward towards the photosphere and perturbs the field there may also be excited by this abrupt change in the corona which increase the horizontal component of the magnetic field in the photosphere near the polarity inversion line (PIL) (Fletcher & Hudson, 2008; Hudson et al., 2008; Wheatland et al., 2018). Li et al. (2011) discovered that following the flare, the horizontal magnetic field close to the flaring PIL shows a change in both observation and simulation.

In this study, we analyzed the photospheric field variations of 37 events by using the 12-minute cadence vector magnetogram from the Helioseismic and Magnetic Imager (HMI) onboard Solar Dynamics Observatory (SDO). We further augment the event list with the addition of the two of four synthetic flares that occurred in the 3-dimensional magneto-hydrodynamic (MHD) simulation reported in (Chatterjee et al., 2016) and (Korsós et al.,

2018). The primary motivation of this work is to understand the correlation of the change in vertical Lorentz force with the eruptivity of the flares and uniquely classify flares associated with CMEs in terms of the change in Lorentz force. The rest of the paper is structured as follows. In Section 4.2, we describe the data set and methods employed. The results are presented in Section 4.3. Finally, we discuss the results and summarize our conclusions in Section 4.4.

4.2 Data and Methods

4.2.1 Observational data

Based on the event catalog provided by Jing et al. (2018), we selected 37 major solar flares including 15 X- and 22 M-class flares originated from 26 active regions (ARs) located within $\pm 45^{\circ}$ of the solar disk center. The selected events comprise both eruptive and confined flares over a seven-year period from 26 January 2011 to 11 December 2017. For each event, we used the vector magnetograms of the AR during the flaring event obtained by HMI (Schou et al., 2012), on board SDO (Pesnell et al., 2012). In particular, we used the HMI vector magnetogram series from the version of Space Weather HMI Active Region Patches (SHARP, Turmon et al. (2010b) having a spatial resolution of 0.5 arcsecond with a temporal cadence of 12 minutes. HMI measures the Stokes parameters at six wavelengths centered on Fe I 6173 Å absorption line with a bandwidth of 76 Å. Based on these observations, the photospheric vector magnetic field is derived by inverting full set of Stokes parameters using the Milne-Eddington inversion approach (Borrero et al., 2011) to obtain the vector magnetic-field components in the photosphere. As part of the additional data pre-processing steps, a coordinate transformation is performed to remap the vector fields onto the Lambert cylindrical equal area projection. Subsequently, the components of the vector field are converted into Heliocentric spherical coordinates (B_r, B_θ, B_ϕ). Apart from the 12 minutes cadence, HMI also has high cadence vector magnetic field data with temporal cadence of 135 seconds. However, we carried out our analysis using the 12 minutes cadence vector magnetogram data due to its lower noise level than that of the 135 seconds cadence for full disk vector magnetogram data (Sun et al., 2017). Moreover, the flare related field changes are sufficiently captured with the cadence of 12 minutes as studied previously (Sarkar & Srivastava, 2018; Sarkar et al., 2019)

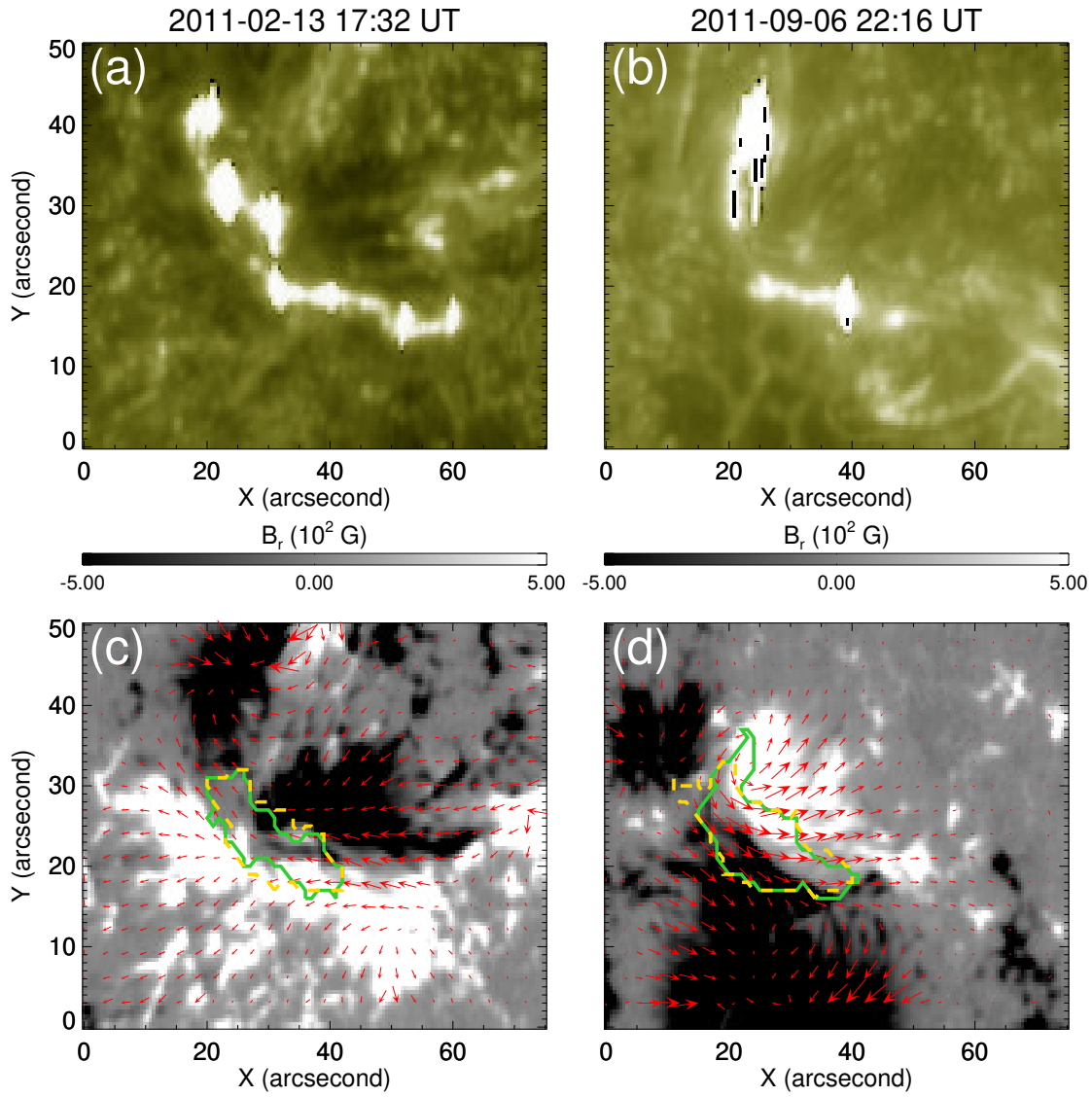

Fig. 4.1 Illustrations of two eruptive events to identify the regions of interest (RoIs) of the magnetic imprints (MIs). The panels a and b are AIA 1600Å images of the two flaring events occurred on 2011 February 13 at 17:38 UT and 2011 September 06 at 22:20 UT respectively. The panels c and d represent the radial magnetic field B_r whose strength is indicated by colorbars. The horizontal component of the magnetic field is shown by the red arrows. The over-plotted contours mark the RoIs selected based on the individual difference maps of the B_h (yellow dashed line) and F_r (solid green lines).

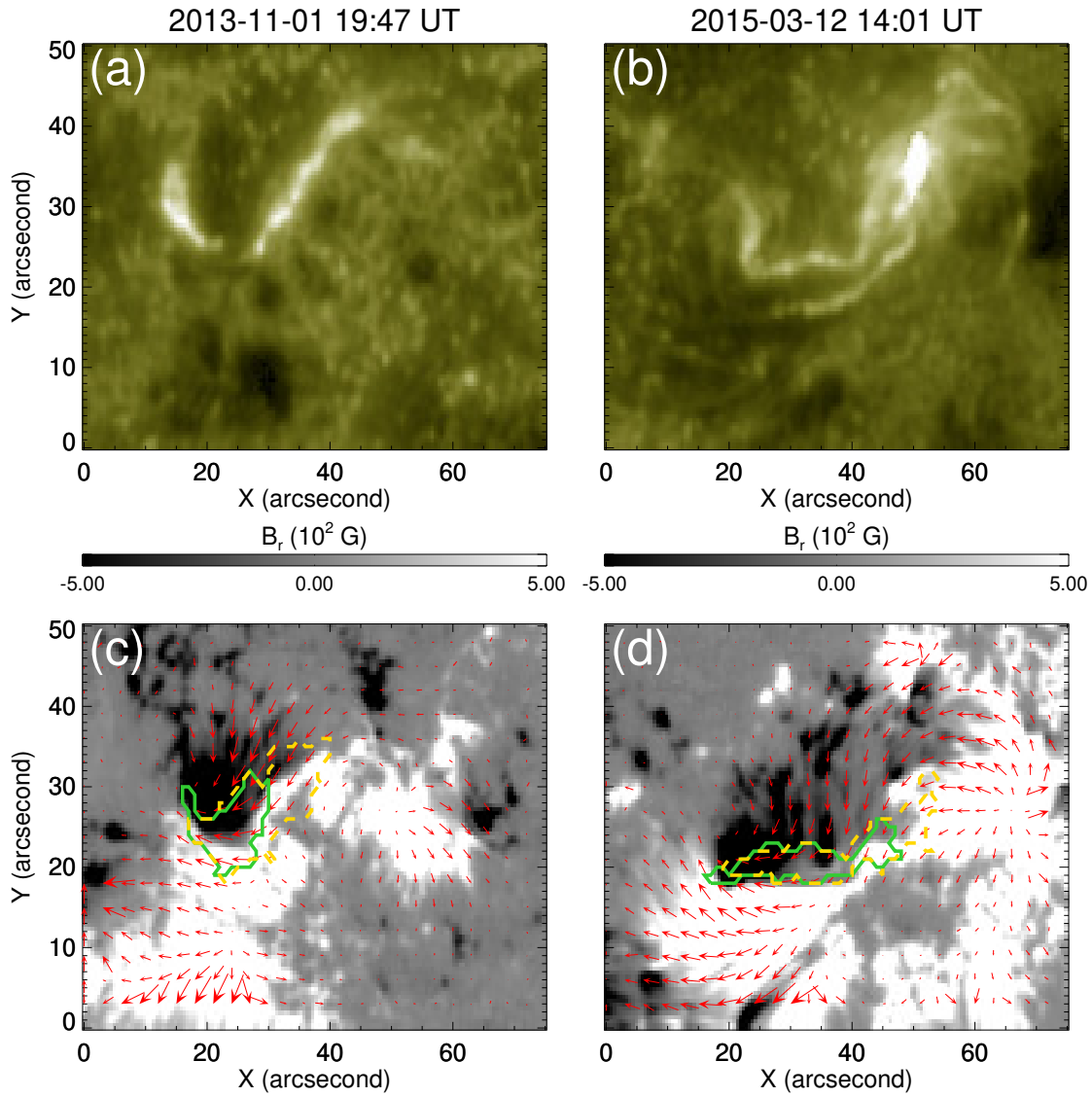

Fig. 4.2 Similar to figure 4.1 but for confined events occurred on (a), (c) 2013 November 01 at 19:53 UT and (b), (d) 2015 March 12 at 14:08 UT.

We have also used the 1600 Å images provided by AIA (Lemen et al., 2012) on board SDO to approximate the location of flare ribbons, which helps identify and select the Region of Interest on the vector magnetograms. In order to characterize and analyze the evolution of magnetic field changes, we chose a 12-hour time-window around the time of the solar flare, encompassing six hours both before and after the peak of the flare. The flare start, peak and end time is determined from the Hinode catalog [1].

4.2.2 Simulation data

In order to compare the observations with simulation, we focus on the numerical case study presented in Chatterjee et al. (2016) for our analysis. We provide a concise overview of the model setup here for completeness. The box-shaped computational domain has horizontal extents of -18 Mm $< x, y <$ 18 Mm and a vertical one of -8.5 Mm $< z <$ 16.5 Mm, with uniformly spaced grid with dx = dy = 96 km and dz = 48 km, rotating with a angular velocity similar to Sun, forming an angle of 30° with the vertical z-direction. A constant gravity, g_z, points in the negative z-direction. For the calculation, authors use the Pencil Code[2] (Pencil Code Collaboration et al., 2021) - a fully compressible higher-order finite difference tool. Beginning from the initial state, the simulation was run for 263 minutes of solar time. The initial subsurface horizontal magnetic sheet breaks up, rises, and emerges through the surface like a newly emerging AR after about 145 minutes. There were four flaring eruptions recognized. The first two flares in the simulation are B and C-class have onset times at 167.5 and 197.2 minutes, respectively and are analyzed for this work. We excluded the other two flares from the analysis due to the presence of numerical artifacts.

The flares reported in the above work released energies of $\approx 2 \times 10^{31}$ ergs commensurate with B- and C-class flares. First of all, note that it is computationally challenging to produce solar flare energies of M and X class in solar MHD simulations with photospheric flux emergence due to requirement of very high magnetic Reynolds number, domain size and the wall clock time for which such simulations can be run. Conversely, analyzing stronger flares proves easier in observations, while changes caused by weaker flares might go undetected by current instruments. Vasantharaju et al. (2022); Kumar & Kumar (2020), incorporated C-class flares in their study, despite the uncertainty in the vector magnetic field data associated with them. Consequently, we decided to forego additional observational analysis of weak

[1] https://hinode.isee.nagoya-u.ac.jp/flare_catalogue/
[2] https://github.com/pencil-code

flares, focusing instead on understanding the magnetic imprint problem through numerical simulation. Our approach involves tackling the issue from two contrasting perspectives of variability. We intend to comprehensively understand the problem by examining minor flares through numerical simulation and major flares through observational data.

4.2.3 Lorentz force and Masking Algorithm

We utilized the formulation proposed by Fisher et al. (2012) to calculate the total changes in the Lorentz force. The variation in the horizontal and vertical component of the Lorentz force within a time interval of δt is computed using the following equations.

$$\delta F_z = \frac{1}{8\pi} \int_{A_{ph}} (\delta B_h^2 - \delta B_z^2)\, dA \tag{4.1}$$

$$\delta F_h = -\frac{1}{4\pi} \int_{A_{ph}} \delta (B_h B_z)\, dA \tag{4.2}$$

Here B_h and B_z represent the horizontal and vertical components of the magnetic field, respectively, and F_h and F_z are the horizontal and vertical components of the Lorentz force calculated over the volume of the Active Region (AR). The domain A_{ph} corresponds to the photospheric area containing the AR, and dA is the elementary surface area on the photosphere. Similar to the approach by Petrie (2012), we have reversed the signs in equations (4.1) and (4.2) in comparison to Equations (9) and (10) of Fisher et al. (2012). This change accounts for considering the equal and opposite forces acting on the above atmosphere from below. Since significant changes in a horizontal magnetic field and Lorentz forces associated with flares are expected near the Polarity Inversion Line (PIL) (Wang, 2006; Petrie & Sudol, 2010; Petrie, 2012; Sarkar & Srivastava, 2018; Sarkar et al., 2019), we focused our analysis on subdomains near the PIL within the flare productive region of each AR. The reason behind this is based on the assumption that the magnetic field on side boundaries enclosing these subdomains remains relatively constant over time. Additionally, we consider the magnetic field strength on the top boundary to be negligible compared to that at the lower boundary of the photosphere. Consequently, in equation (4.1) and (4.2), only changes in the photosphere magnetic field contribute to the surface integrals, allowing us to estimate the net change in the Lorentz force acting on the photosphere from the volume above the atmosphere.

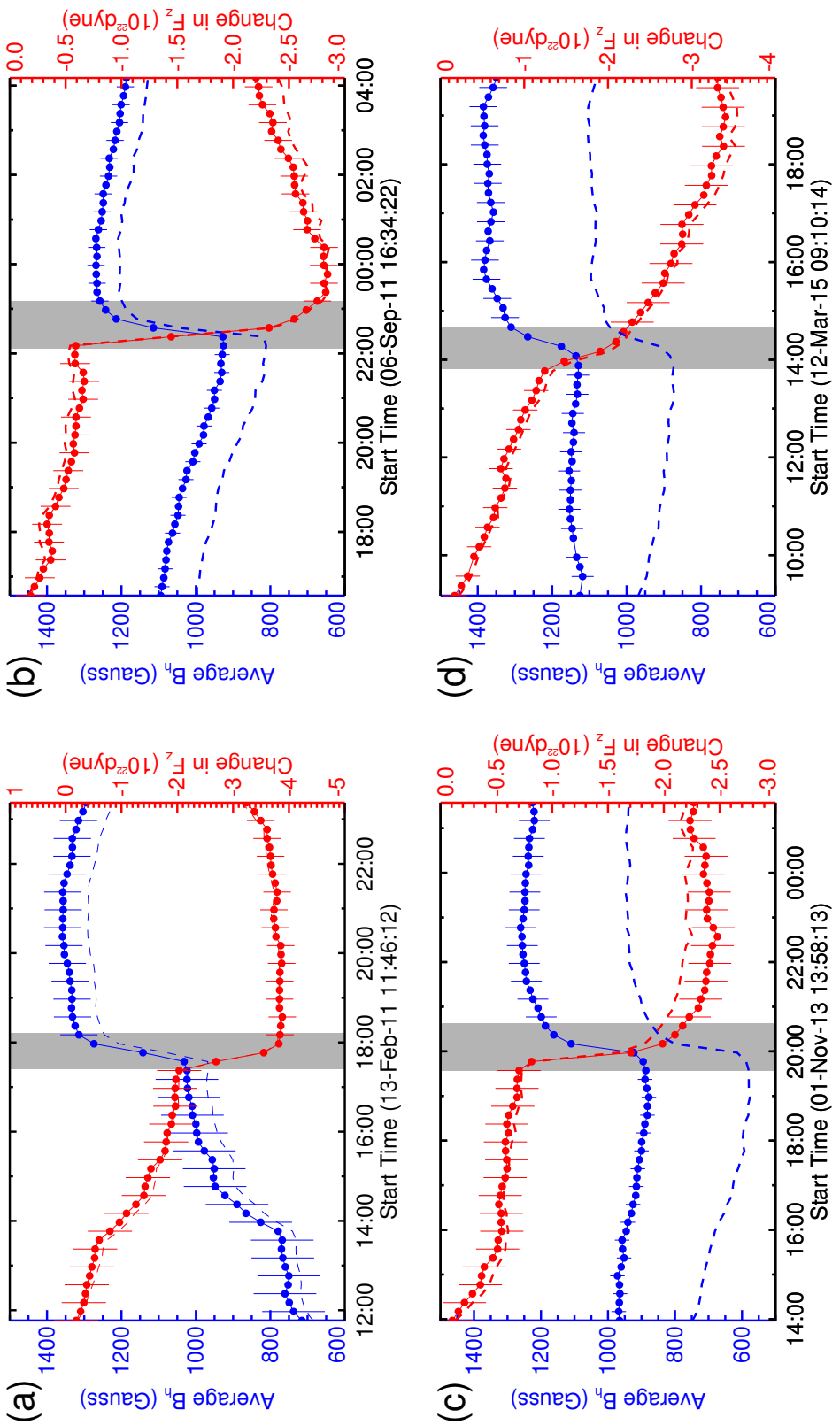

Fig. 4.3 Temporal evolution of average horizontal magnetic fields (blue) and vertical Lorentz force (red) calculated by Lorentz force (solid) and horizontal magnetic field (dashed) contouring method. The panels a and b represent eruptive, whereas the panels c and d represent confined events. The shaded region corresponds to the duration of field change. The vertical error bars represents the fluctuations at a 3σ level in both pre- and post flare states.

We developed a semi-automatic tool to select the sub-region in which we analyzed the flare-associated Lorentz force changes for all the events. As the significant Lorentz force changes are expected to happen very close to the flare peak time, we select time frames approximately 30 minutes before and after the peak phase of the associated flare. Next, we create difference maps of the horizontal magnetic field and vertical Lorentz force estimated at the above-mentioned time frames separately. We use information of both the horizontal magnetic field (B_h) and vertical Lorentz force (F_r) independently to avoid any selection bias in identifying the areas where the most significant changes occurred as discussed in Vasantharaju et al. (2022); Liu et al. (2022); Yadav & Kazachenko (2023); Petrie (2012). To these difference maps, we apply a threshold to select the sub-regions that demarcate the area of positive change (> 100 Gauss) in the horizontal magnetic field or the negative change ($< -10^{19}$ dyne) in the vertical component of the Lorentz force. Applying this method, we find several sub-regions within the AR. In order to find the correct region of interest (RoI), we manually select the sub-region which is in the closest proximity to the flaring location observed in the AIA images. Figure 4.1 and 4.2 illustrates the identified RoIs based on both the B_h and F_r difference maps for the two eruptive and confined events from Table (4.1) respectively.

4.3 Results & Discussion

The characteristic variations in the average horizontal magnetic field and the total downward Lorentz force for two eruptive and two confined flaring events which are observed on February 13, 2011 (Event No 1); September 06, 2011 (Event No 7) and November 1, 2013 (Event No 16) and March 12, 2015 (event No 33) are described here as examples. Then, for all 37 events, we summaries their variations with flare strength.

4.3.1 Evolution of B_h and F_z

After successful identification of the flaring region using two different methods based on the B_h and F_z difference maps, we continue our analysis within that sub-region. We studied the temporal evolution of the average B_h, and the total downward Lorentz force change, F_z, in the selected region near the PIL for each case. As an example, the time variation of average B_h

and downward F_z for the same two eruptive (Event No 1 and 7) and confined events (Event No 16 and 33) are shown in Figure 4.3. The top and bottom panels represent the variation of average B_h and downward F_z over time for each eruptive and confined events, respectively. All flaring events show a abrupt change in both B_h and F_z using both the methods. The shaded region in these plots indicates the field change duration. The error bars depict fluctuations corresponding to a 3σ significance in both pre and post flaring states. These fluctuations are determined through separate linear regression of the temporal changes in B_h and F_z before and after the shaded time interval. The error analysis is performed using a time window of 6 hours and a resolution of 12 minutes in each states. The errors specified in columns 8-11 of Table (4.1) are determined by averaging the errors from the pre-flare and post-flare states.

Within the RoI determined from the F_z difference maps, the average change in B_h and F_z for eruptive events as shown in Figure 4.3 found to be 293.8 Gauss, 1.8×10^{22} dyne for Event ID 1 and 370.4 Gauss, 2.3×10^{22} dyne for Event ID 7. Similarly, for confined events, the average change in B_h and F_z in the RoI given by the Lorentz force change were 338 Gauss, 1.5×10^{22} dyne for Event ID 16 and 243 Gauss, 1.2×10^{22} dyne for Event ID 33.

On the other hand, when the RoI was identified based on the B_h difference map, the average changes in B_h and F_z for eruptive events were 275.1 Gauss, 1.7×10^{22} dyne for Event ID 1 and 361 Gauss and 2.1×10^{22} dyne for Event ID 7, respectively. For confined events, the average changes in B_h and F_z in the RoI given by the change of horizontal magnetic field were 308.3 Gauss, 1.4×10^{22} dyne for Event ID 16 and 217.2 Gauss, 1.3×10^{22} for Event ID 33.

Figure 4.3 shows that the enhancement of average B_h is permanent throughout the post-flare phase (at least within 6 hours of time window after the flare peak time), which agrees with the previous studies (Wang et al., 2012b; Petrie, 2012; Sun et al., 2017; Liu et al., 2022). The total downward F_z is observed to show an abrupt decrease during the flare interval, which is also irreversible. The average changes in B_h and the total change in vertical F_z for all 37 events, analyzed for different RoI identification methods, are tabulated in Table (4.1).

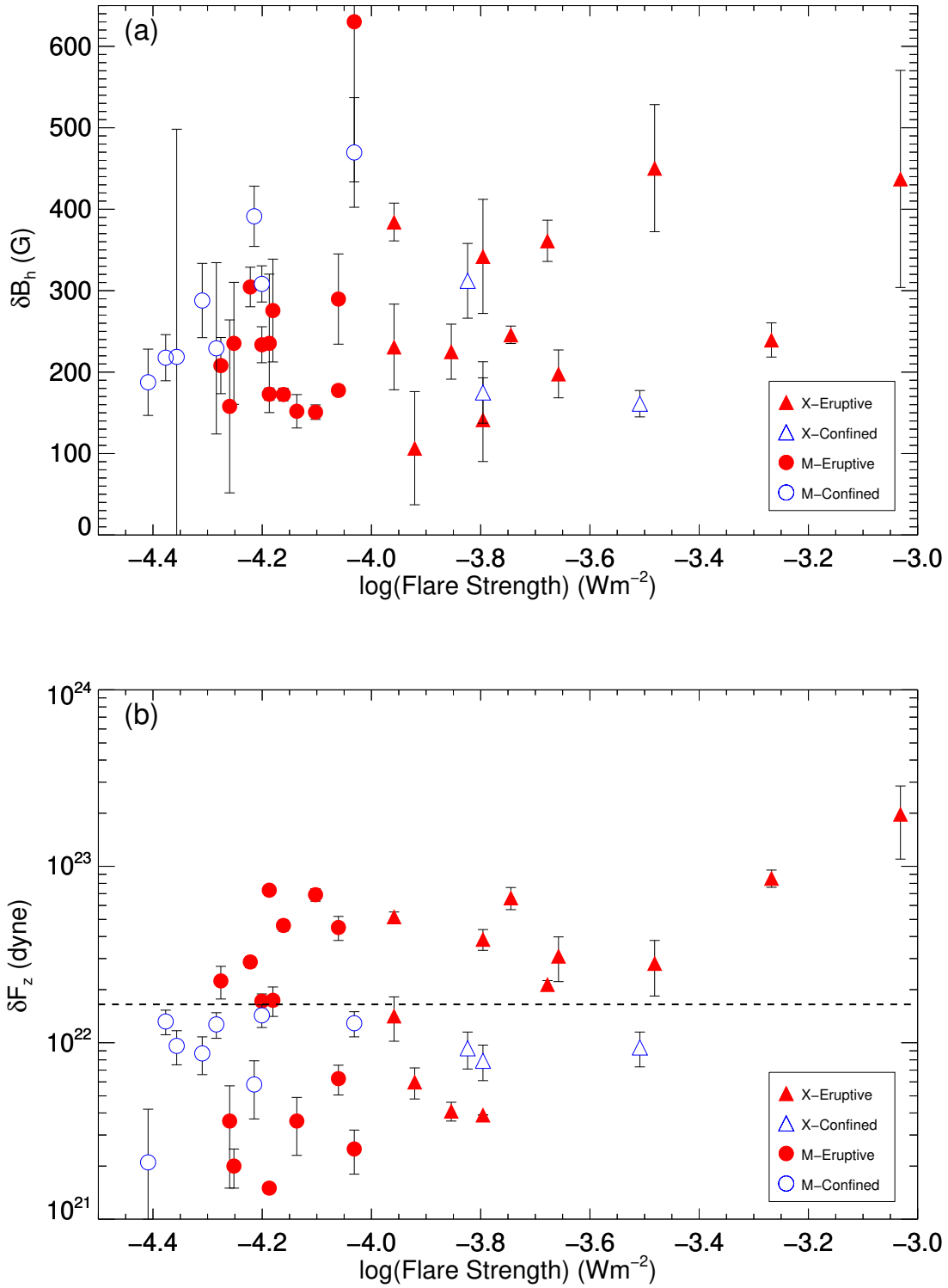

Fig. 4.4 Scatter plot of (a) Average horizontal magnetic field change δB_h vs logarithmic flare strength and (b) Vertical Lorentz force change δF_z vs logarithmic flare strength for RoIs identified based on the difference maps of horizontal magnetic field. Filled and empty symbols correspond to the eruptive and confined flares, respectively. The triangular and circular symbols are for X-class and M-class flares, respectively. The horizontal dashed line indicates the threshold Lorentz force above which no confined flares are observed.

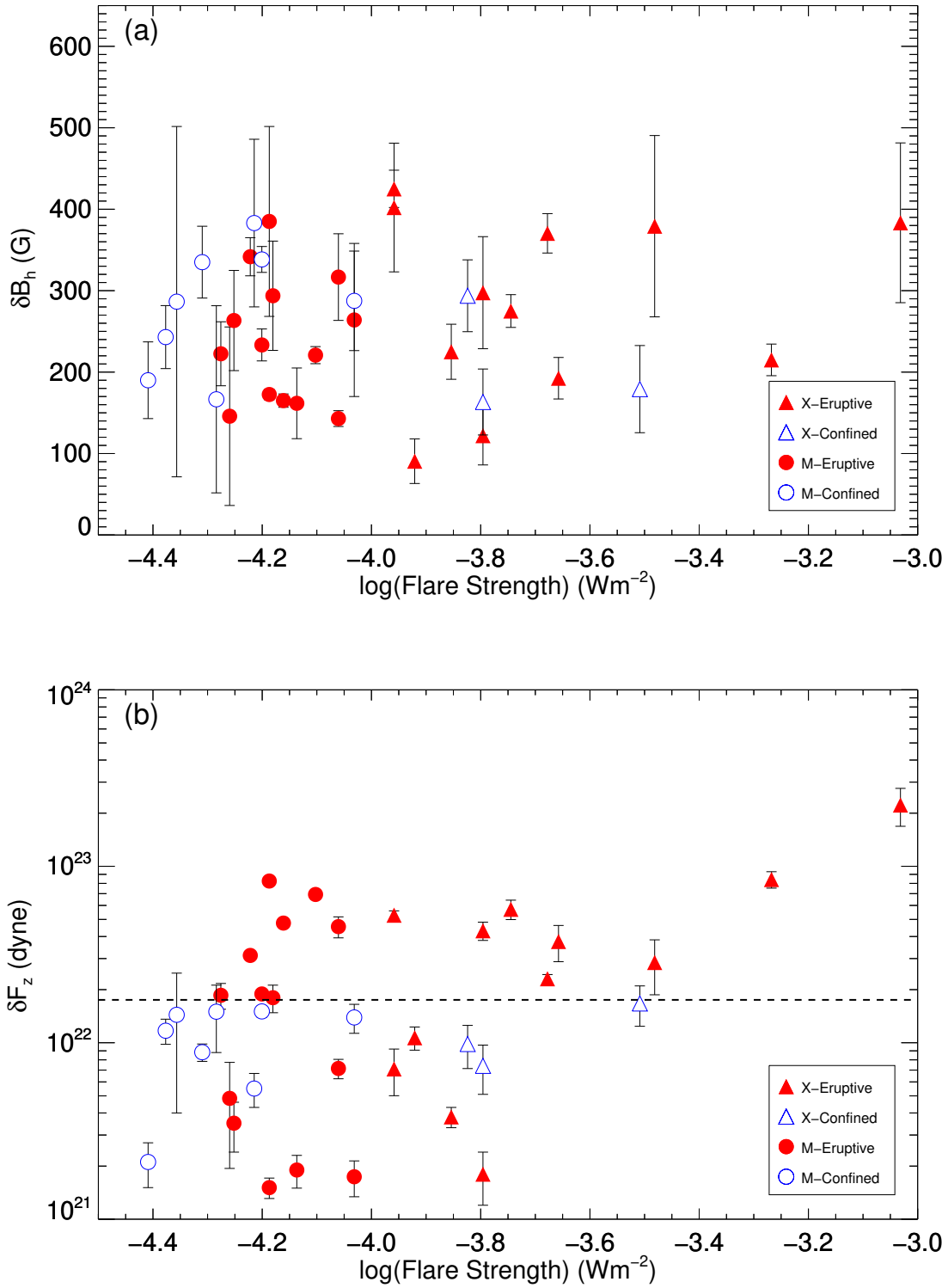

Fig. 4.5 Similar to Figure 4.4 but for RoIs identified based on the difference maps of Lorentz force.

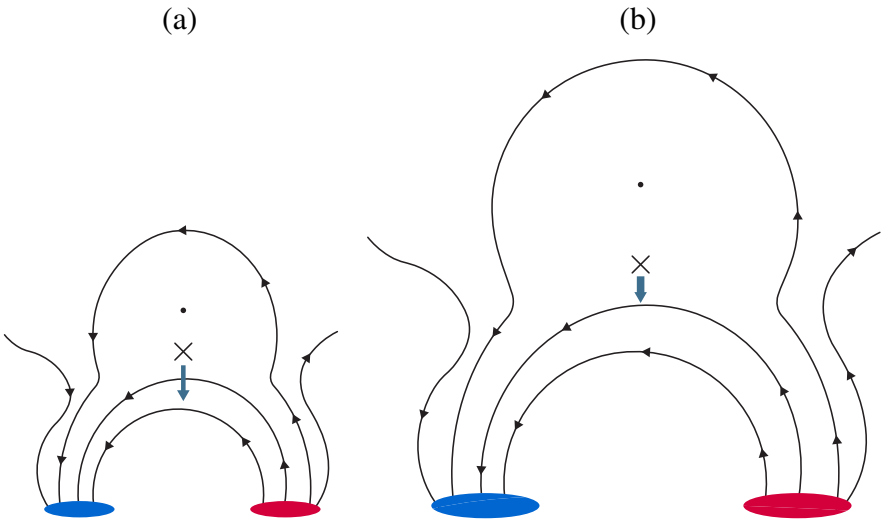

Fig. 4.6 A sketch of the magnetic field configuration of (a) eruptive event with higher Lorentz force change and (b) eruptive event with lower Lorentz force change. Red and blue filled regions are positive and negative polarity regions whereas solid lines refer to the magnetic field lines. The X mark represents the location of the reconnection site and the downward arrow implies the direction of vertical Lorentz force responsible for the increase of horizontal magnetic field.

4.3.2 Statistics of B_h and F_z evolution

In this subsection, we present the statistical properties of the average change δB_h and the δF_z for all the events listed in Table (4.1). The results show that the average δB_h ranges from 15 Gauss to 425 Gauss, while the Lorentz force change varies from 1.5×10^{21} dyne to about 22.3×10^{22} dyne when the RoI was identified based on the change in vertical Lorentz force. Similarly, the average δB_h ranges from 45 Gauss to 630 Gauss, while the Lorentz force change varies from 1.5×10^{21} dyne to about 19.8×10^{22} dyne when the RoI was identified based on the change in horizontal magnetic field. The data variations result from the adoption of different methods to identify the Region of Interest (RoI). This approach was employed to prevent any potential bias in the analysis. However, it is important to note that the results do not show significant differences and remain within the error limits.

Figure 4.4, 4.5 illustrates the change in average B_h and total downward F_z plotted against the flare strength for B_h and F_z contouring method respectively. The change in average B_h does not exhibit statistically significant differences between eruptive and confined events, which is

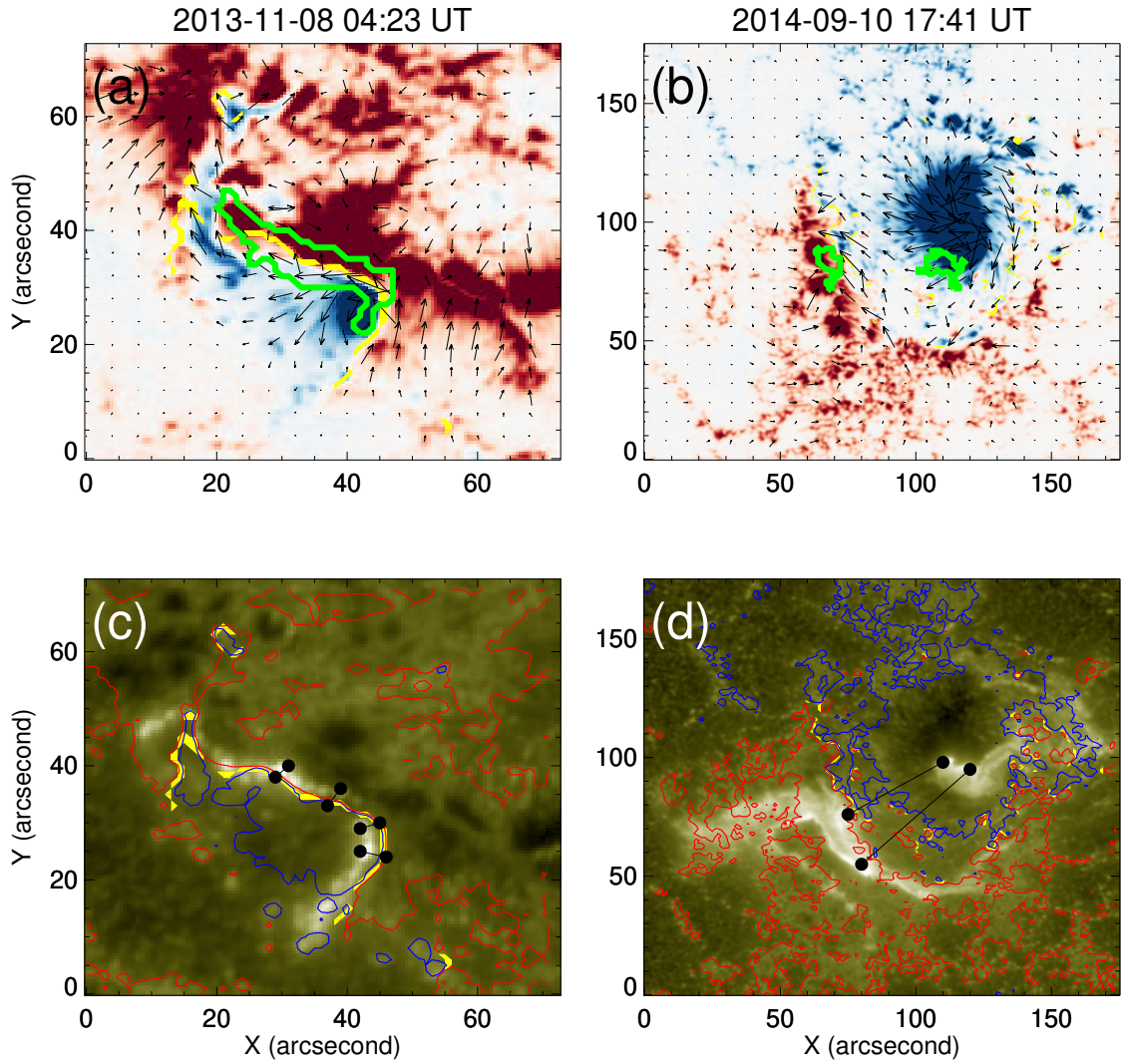

Fig. 4.7 Illustrations demonstrating the calculation of ribbon distances for two events. Panels a and b represent the photospheric magnetic field maps for the two events occurred on 2013-11-08 04:23 UT and 2014-09-10 17:41 UT respectively. The red/blue colors represent the positive/negative polarities of B_r plotted within a range of $\pm$500 Gauss. The yellow line is indicative of the polarity inversion line (PIL) and the green contour signifies the region where the significant change in Lorentz force is observed. The black arrows represent the horizontal magnetic field lines. Panels c and d shows the flare ribbons as observed in the AIA 1600 Åchannels. The blue and red contours represent the overlaid positive and negative polarities of B_r at levels *pm* 100 Gauss. The solid black lines represent the ribbon distances.

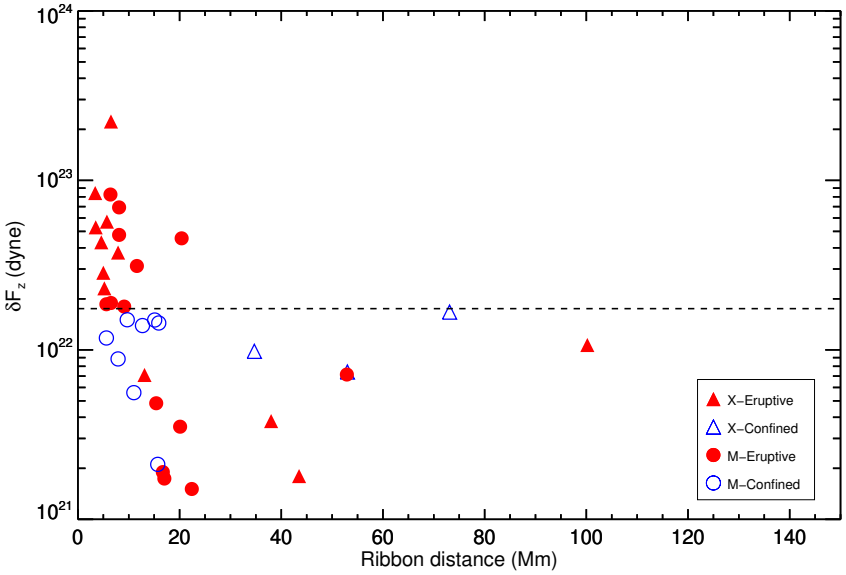

Fig. 4.8 Scatter plot of vertical Lorentz force change vs ribbon distance. The values of Lorentz force change shown in the figure are estimated using the method based on the Lorentz force difference maps. Filled and empty symbols correspond to the eruptive and confined flares, respectively. The triangular and circular symbols imply X-class and M-class flares, respectively. The horizontal dashed line is drawn to illustrate the threshold value of change in Lorentz force. Few data points overlap each other.

consistent with the findings of Liu et al. (2022) and Yadav & Kazachenko (2023). Although the change in B_h and the respective change in F_z doesn't have any specific direct connection.

However, the change in F_z with flare strength clearly distinguishes between the two types of events. All confined flares have $\delta F_z < 1.8 \times 10^{22}$ dyne, whereas most eruptive flares show higher δF_z values than the above mentioned limit. This suggests that the strength of flare associated δF_z depends on whether the flare is eruptive or confined. The threshold limit can serve as a criterion for determining the presence of the associated CMEs based on these calculations. This reveals that while the change in average B_h does not discriminate between eruptive and confined events, the change in total downward Lorentz force provides a clear distinction, indicating that magnetic imprints on the photosphere can be indicative of flare eruptivity.

It is worth noting that out of the 26 eruptive events, 9 of them exhibit a change of F_z below the previously mentioned threshold limit. We present one such event in Figure 4.7(b) & (d). In Figure (b), the two green contours represent the regions where the most significant change

in Lorentz force is observed. Interestingly, in this event, the strong (>100 Gauss) opposite polarity regions are not in close proximity to each other. This spatial arrangement seems to have an impact on the magnetic field dynamics. On the other hand, the rest of the 17 eruptive flares associated with δF_z greater than the threshold value, are observed to occur where the regions of strong opposing polarities are close to each other (see an example of such event in Figure 4.7(a) & (c)).

This indicates that the morphology of the active region may be a contributing factor for the relatively smaller change in F_z in our investigation. The spatial distribution of magnetic polarities within the active region appears to play a role in shaping the observed changes in magnetic fields and Lorentz forces during eruptive events.

This can be better understood with the help of a cartoon, as shown in the Figure 4.6. The cartoon illustrates how the spatial distribution and arrangement of opposite polarity regions within an active region can influence the observed changes in magnetic fields and Lorentz force during flaring events. The solar flares are usually observed with two parallel ribbons, lying both sides of the PIL. If the two flare ribbons are thought of connected via newly reconnected semi-circular magnetic loops, then the distance between the two parallel ribbons would be proportional to the length of the loop and the reconnection height (Toriumi et al., 2017; Reep & Toriumi, 2017). Thus, a shorter ribbon distance would corresponds to smaller loop, whereas a longer ribbon distance corresponds to a larger loop in the solar atmosphere. For those events where the opposite polarity regions are in close proximity, the distance between the two parallel ribbons during the flare onset time is much shorter, as they form nearer to the PIL. This suggests that, in such cases, reconnection initiates at a lower altitude, resulting in a more significant impact on the photosphere characterized by larger changes in the Lorentz force (Liu et al., 2022; Yadav & Kazachenko, 2023). However, if the strong opposite polarity regions are not in close proximity to each other, the flare ribbons start a bit away from the PIL indicating that the reconnection begins at a higher height. As a result, the impact on the solar photosphere is less in this situation, which justifies a smaller change in Lorentz force that we observed.

This explanation is well consistent with the results shown in Figure 4.7 (c) & (d), where the ribbon distance (d_{ribbon}) is estimated during the onset of the associated flares. As the flare ribbons mark the footpoints of the reconnecting magnetic loops, half of the distance ($d_{ribbon}/2$) between the two flare ribbons estimated during the onset time of the flare serves a proxy for the initial reconnection height in the solar corona. We use the observations from AIA 1600 Å channel to identify the flare ribbons as shown in Figure 4.7.

The method utilized for estimating the ribbon distance (d_{ribbon}) is presented with the example of two flares from our event list as depicted in Figure 4.7. The first one was the X1.1 eruptive flare that occurred on 8 November 2013 (event-19) and the second one was X1.6 eruptive flare occurred on 10 September 2014 (event-25). Although both the flaring events were eruptive in nature, the change in Lorentz force associated with event-19 surpasses the critical threshold, whereas for event-25, it falls below the critical threshold. In order to understand the distinct morphological differences between this two events, we first identify the proximity of the polarity inversion line (PIL) by super-imposing the contours of B_r at levels $\pm$ 100 Gauss onto the AIA1600 Å images. Additionally, we apply the automated algorithm to identify the PIL (indicated by the yellow lines) as developed in Sarkar & Srivastava (2018). Figure 4.7 (c) depicts that the flare ribbons during the onset time of the flare for event-19, form very close to the PIL. Moreover, the associated HMI observations show that the opposite polarity regions of strong B_r are closely located, forming a compact field region near the flaring PIL. As the flare ribbons at the either side of the PIL for event-19 does not form parallel to each other, we manually selected multiple points on the PIL from which we measured the shortest distance to the ribbon. Furthermore, taking an average of those multiple measurements and multiplying the mean distance with a factor of 2, we estimate the distance d_{ribbon}. In contrast to the event-19, the flare ribbons in event-25 form much away from the PIL and the opposite polarity regions of strong B_r also locate away from the PIL, forming a dispersed field region at the flaring location (see Figure 4.7 (b) & (d)). As the flare ribbons in event-25 form parallel to each other, we select points along the ribbons located either side of the PIL to estimate the average distance (d_{ribbon}) between the two ribbons. We apply the above mentioned method to all the events and list the estimated d_{ribbon} in Table 4.1.

The change in Lorentz force is plotted in Figure 4.8 against d_{ribbon}. It is evident from the plot that the majority of eruptive events exhibit a ribbon separation smaller than 9 Mm.

In contrast, those eruptive events that show a smaller change in the Lorentz force tend to have higher ribbon distances, typically exceeding 15 Mm. This indicates a potential implication between the ribbon separation and the magnitude of the change in Lorentz force during eruptive events. Thus the ribbon separation could serve as an additional factor to consider when studying the magnetic imprints associated with the solar flares. Overall, this helps to visualize how the specific morphology of the active region plays a crucial role in determining the magnitude of changes in the total downward Lorentz force (F_z), and this may be one of the factors contributing to the observed variations during such events.

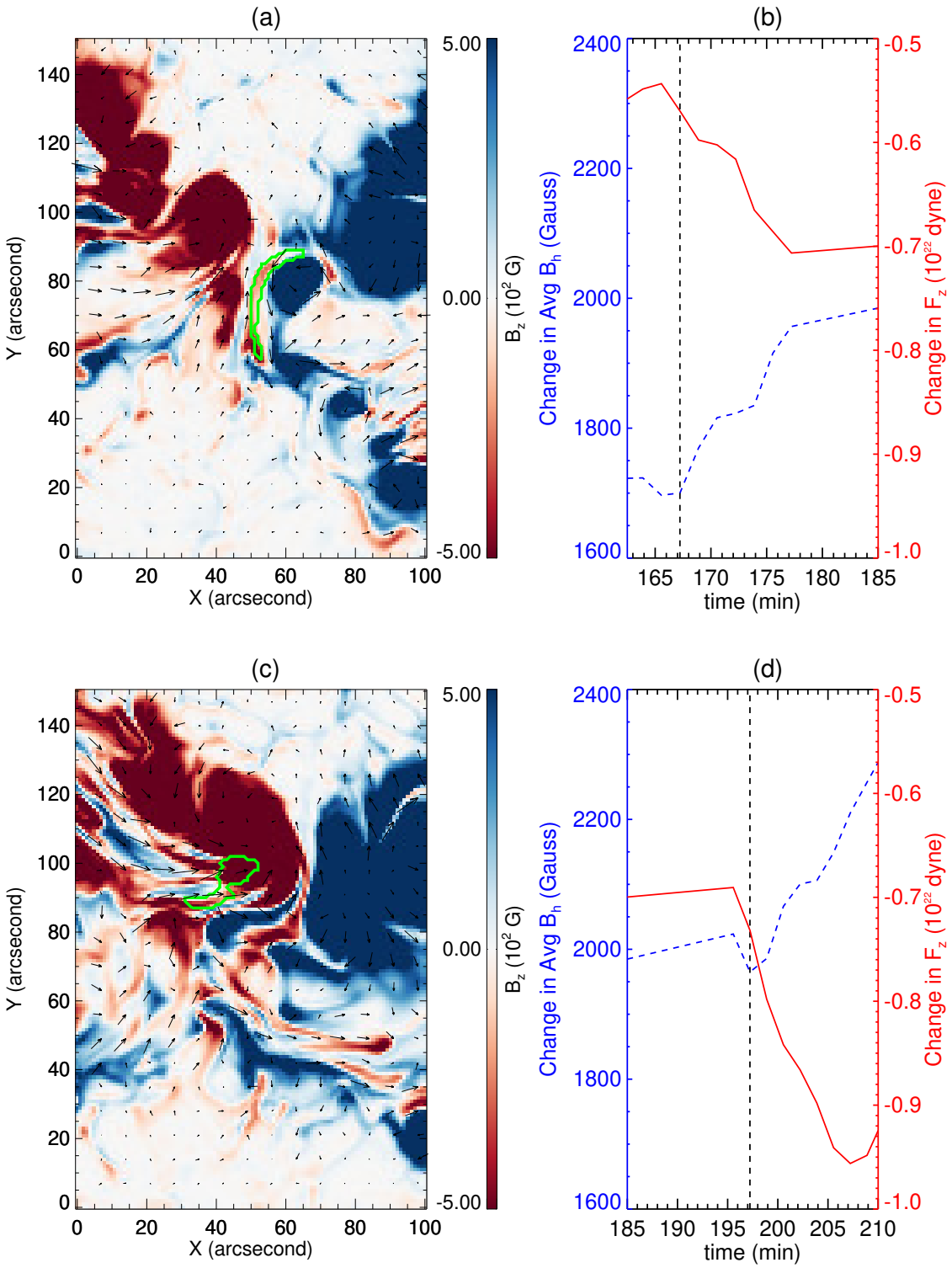

Fig. 4.9 (a) Illustration of the vertical magnetic field B_z for the B-class synthetic flare events and (b) the corresponding temporal evolution of average horizontal magnetic fields (blue) and vertical Lorentz force (red). (c) and (d) Same as (a) and (b) but for the synthetic C-class flare. The green contours in (a) and (c) mark the region where significant change in Lorentz force occurs. The strength of the vertical magnetic field is represented by the colorbar. The dashed vertical black lines represent the flare time.

4.3.3 Downward propagation of the Lorentz force

We applied the same procedure as in observational data analysis to the B & C class synthetic flare events and the similar profile of B_h and F_z are observed. Figure 4.9 presents the results of our analysis performed on the simulation data. Utilizing our semi-automatic code, we are able to select the RoIs accurately (see the green contours in Figure 4.9 [a] and [c]), which agrees with the flaring region identified by Korsós et al. (2018) based on the temperature anomaly. The dashed vertical lines in panels [b] and [d], represent the onset time of B and C-class flare. The change of B_h in B and C-class flare is 60 Gauss and 400 Gauss, respectively, whereas, the change in F_z is 0.15×10^{22} dyne and 0.27×10^{22} dyne respectively.

We have noticed a remarkable resemblance in the temporal evolution in the simulation with the observational data for the changes in horizontal magnetic field and vertical Lorentz force. While we cannot directly compare the simulation results to our observational data due to differences in flare class and size of active regions involved, the fact that both the horizontal magnetic field and Lorentz force display similar variations indicates that the underlying physics governing the changes in magnetic properties remains consistent across different flare classes.

Our simulation allows us to calculate the total Lorentz force, defined by $\mathbf{J} \times \mathbf{B}$, in a 3D setup. In contrast to observational data, where magnetic field components are only available at the solar surface, our simulation provides all physical variables defined at all heights from the photosphere to the corona. We plotted the height time plot of Lorentz force averaged over the horizontal plane for the two synthetic events as shown in Figure 4.10 which agrees with the eruption time mentioned in Korsós et al. (2018). This comes out to be of the order of 10^2 dyne whereas the volume integral of average $\mathbf{J} \times \mathbf{B}$ over the domain comes out to the order of 10^{22} dyne which agrees with the observational results. We observed that the Lorentz force propagates towards the photosphere from the reconnection site similar to Barczynski et al. (2019). The average propagation speed is $2.4\,\mathrm{km}s^{-1}$ and $2.3\,\mathrm{km}s^{-1}$ for simulated B and C-class flares, respectively. Therefore, we argue that the Lorentz force from the reconnection site (marked 'X' in Figure 4.6) propagates downward towards the photosphere, resulting in changes of F_z and B_h as estimated from the HMI magnetogram.

Our analysis of the synthetic flare events provides further support for the importance of the downward propagation of the Lorentz force and its influence on the photosphere, which is consistent with both previous simulation studies and the observational data.

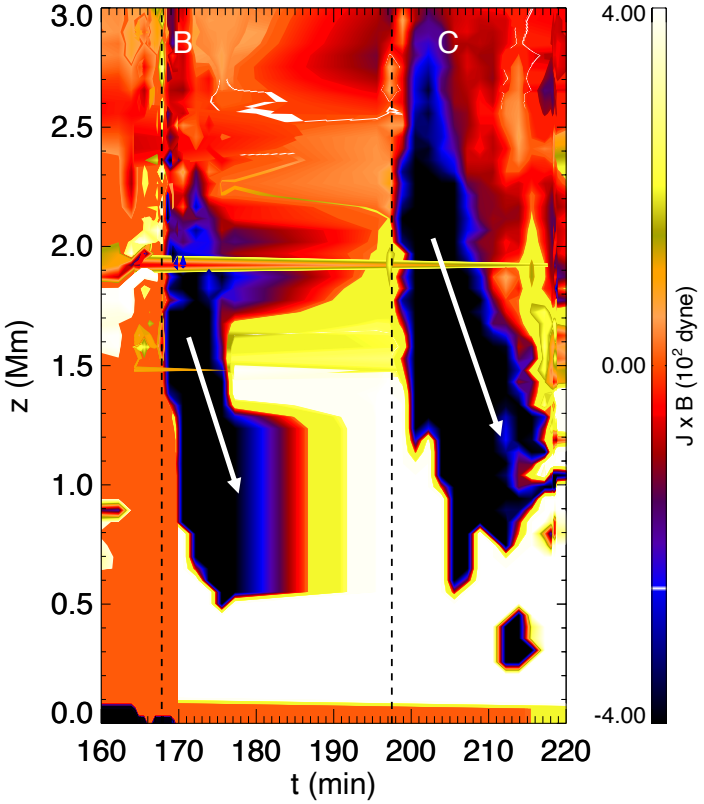

Fig. 4.10 Height–time diagram of Lorentz force from the 3D MHD simulation to show its downward propagation. The dashed vertical lines represent the time of the two synthetic flares. The arrow is for guiding the eye towards the propagation direction of the Lorentz force.

4.4 Summary

We present a statistical analysis of the flare-associated changes in the photospheric magnetic field close to the neutral line of the flaring region during the 37 flare events stronger than GOES M5 class flare from 26 different ARs. We used a semi-automatic technique to pick the sub-region close to the polarity inversion line where the significant changes in Lorentz force occur during the flare. We investigate whether the flare associated changes in Lorentz force and the photospheric magnetic field have any dependency on the confined or eruptive nature of a flare.

We have found a consistent pattern in the variation of the change in horizontal photospheric magnetic field (B_h) and change in vertical Lorentz force (F_z) for each event using two different

methods to identify the most significant field change. The mean B_h appears to increase in every case, showing abrupt enhancement in the temporal evolution. The observed increase in the horizontal magnetic field, B_h, can be attributed to the coronal implosion conjecture, as proposed by Hudson (2000) or reconnection-driven contraction in post-flare loops, as shown by Barczynski et al. (2019) using a zero-β approximation MHD simulation.

We also observed a significant, abrupt, permanent downward change in vertical Lorentz force during each flare, demonstrating an abrupt change in the temporal evolution, which is a common feature in large flares (Sun et al., 2012; Wang et al., 2012a). To understand the behavior, we compared the results of the MHD simulation of a solar flare and found that, the Lorentz force $(J \times B)$ propagates downward towards the photosphere over time, leading to the observed change in vertical Lorentz force. We observed similar temporal evolution profiles for the average δB_h and the total δF_z for both of these synthetic flares. This consistency in the temporal evolution patterns of δB_h and δF_z further supports the robustness and validity of our analysis method for studying flares, both in observational data and in simulated events.

Our conclusion regarding the distinction between eruptive and confined flares is based on a comparison of the δF_z (change in vertical Lorentz force) for both types of flares. Eruptive flares were found to leave a significant magnetic imprint on the solar photosphere. Conversely, confined flares exhibited comparatively smaller changes in the photospheric magnetic field (Sun et al., 2012; Sarkar & Srivastava, 2018). This observation is in agreement with the flare-related momentum balance condition, which suggests that the Lorentz-force impulse is directly related to the associated CME momentum (Fisher et al., 2012; Wang et al., 2012b). This is strongly supported by our findings from the analysis of the selected 26 eruptive and 11 non-eruptive flares in this work. The significant change in the photospheric magnetic field for eruptive flares and the comparatively smaller change for confined flares support the notion that the Lorentz-force impulse is linked to the presence and strength of associated CMEs.

However, to distinguish between the two types of flares, our analysis offers an upper threshold value of vertical Lorentz force change. Despite nine eruptive events having Lorentz force change below our threshold, we did not witness any confined events with Lorentz force larger than 1.8×10^{22} dyne. Using 21 flaring episodes, between August 2010 and November 2015, Vasantharaju et al. (2022) suggested that the strength of the magnetic imprint is independent of whether the flare is eruptive or not. On the contrary, our findings indicate that the mean B_h change makes no distinction, whereas the change in vertical Lorentz force provides a clear differentiation between confined and eruptive flares. This difference is likely due to the inclusion of the term δB_z^2 when computing δF_z, identifying the RoI using an improved

algorithm and inclusion of larger sample of flaring events in our study with energies equal to or exceeding those of M-class flares.

For eruptive events with Lorentz force change below the threshold, we noticed a significantly higher separation distance between the parallel flare ribbons when they form during the onset time of the flare. The source location of those events also displays distinct morphology, as the distance between the two strongly opposing magnetic-polarity regions at the flaring location is observed to be comparatively larger. This larger separation is due to a higher reconnection height at the start of the flare as compared to the other eruptive events, leading to weaker Lorentz force change in the photosphere. Overall, our analysis reveals that the change in the vertical Lorentz force plays a crucial role in distinguishing confined and eruptive flares. The observed differences are influenced by factors such as the CME association and the separation distance of the parallel flare ribbons at the time of flare onset.

In this paper, we have examined the effects of major flares on fields near neutral lines. The present analysis is a step forward to distinguish the eruptive and confined flares in terms of the change in the vertical Lorentz force. Although a clear distinction between confined and eruptive events has been seen in this sample, it will be instructive to look at a larger sample of events and their corresponding vector field measurements from HMI and their associations with the CMEs.

No	Date	Peak Time	NOAA AR	Position	Flare Class	Type	Fz Contour		Bh Contour		Ribbon Distance
							B_h (G)	F_z (dyn)	B_h (G)	F_z (dyn)	(Mm)
1	2011-02-13	17:38:00	11158	S20E04	M6.6	E	293.7 ± 67.1	1.80 ± 0.32	275.6 ± 63.1	1.74 ± 0.33	9.1
2	2011-02-15	1:56:00	11158	S20W10	X2.2	E	192.5 ± 25.5	3.75 ± 0.87	197.8 ± 29.4	3.10 ± 0.88	7.9
3	2011-03-09	23:23:00	11166	N08W09	X1.5	C	293.7 ± 44.1	0.98 ± 0.27	312.1 ± 45.9	0.93 ± 0.22	34.7
4	2011-07-30	2:09:00	11261	S20W10	M9.3	C	287.5 ± 61.1	1.39 ± 0.26	469.7 ± 67.3	1.29 ± 0.19	12.7
5	2011-08-03	13:48:00	11261	N16W30	M6.0	E	341.6 ± 23.4	3.12 ± 0.18	304.5 ± 24.3	2.87 ± 0.21	11.6
6	2011-09-06	1:50:00	11283	N14W07	M5.3	E	222.5 ± 39.3	1.85 ± 0.31	208.0 ± 34.5	2.24 ± 0.47	5.6
7	2011-09-06	22:20:00	11283	N14W18	X2.1	E	370.4 ± 24.2	2.30 ± 0.13	361.2 ± 25.3	2.14 ± 0.11	5.2
8	2011-10-02	0:50:00	11305	N12W26	M3.9	C	190.0 ± 47.1	0.21 ± 0.06	187.5 ± 40.7	0.21 ± 0.10	15.7
9	2012-01-23	3:59:00	11402	N28W21	M8.7	E	316.6 ± 53.2	0.71 ± 0.09	289.7 ± 55.4	0.62 ± 0.12	52.9
10	2012-03-07	0:24:00	11429	N17E31	X5.4	E	215.0 ± 19.4	8.42 ± 0.90	239.5 ± 21.0	8.56 ± 0.96	3.4
11	2012-03-09	3:53:00	11429	N15W03	M6.3	E	233.3 ± 19.6	1.89 ± 0.09	233.6 ± 22.1	1.72 ± 0.17	6.5
12	2012-07-02	10:52:00	11515	S17E08	M5.6	E	263.3 ± 61.5	0.35 ± 0.11	235.2 ± 74.9	0.20 ± 0.05	20.1
13	2012-07-12	16:49:00	11520	S15W01	X1.4	E	225.0 ± 33.8	0.38 ± 0.05	225.1 ± 33.8	0.41 ± 0.05	38.0
14	2013-04-11	7:16:00	11719	N09E12	M6.5	E	385.0 ± 116.6	0.15 ± 0.02	235.3 ± 85.0	0.15 ± 0.01	22.4
15	2013-10-24	0:30:00	11877	S09E10	M9.3	E	264.0 ± 94.0	0.17 ± 0.04	630.2 ± 196.7	0.25 ± 0.07	17.0
16	2013-11-01	19:53:00	11884	S12E01	M6.3	C	338.3 ± 15.9	1.50 ± 0.11	308.3 ± 22.2	1.43 ± 0.14	9.7
17	2013-11-03	5:22:00	11884	S12W17	M4.9	C	335.0 ± 44.1	0.88 ± 0.10	287.9 ± 45.6	0.87 ± 0.20	7.9
18	2013-11-05	22:12:00	11890	S12E44	X3.3	E	379.1 ± 111.3	2.85 ± 0.98	450.4 ± 78.0	2.82 ± 0.98	5.0
19	2013-11-08	4:26:00	11890	S12E13	X1.1	E	425.0 ± 22.9	5.28 ± 0.31	384.3 ± 23.2	5.18 ± 0.33	3.5
20	2014-01-07	18:32:00	11944	S15W11	X1.2	E	90.6 ± 27.4	1.06 ± 0.16	106.6 ± 69.5	0.6 ± 0.12	100.2
21	2014-02-02	9:31:00	11967	S10E13	M4.4	C	286.5 ± 215.1	1.44 ± 1.04	218.7 ± 279.5	0.96 ± 0.48	15.9

Table 4.1 List of 37 flare events from 27 active regions and their associated magnetic properties

No	Date	Peak Time	NOAA AR	Position	Flare Class	Type	Fz Contour		Bh Contour		Ribbon Distance (Mm)
							B_h (G)	F_z (dyn)	B_h (G)	F_z (dyn)	
22	2014-02-04	4:00:00	11967	S14W06	M5.2	C	166.6 ± 114.9	1.50 ± 0.62	229.2 ± 105.2	1.27 ± 0.32	15.1
23	2014-03-29	17:48:00	12017	N10W32	X1.1	E	402.0 ± 79.0	0.71 ± 0.21	230.9 ± 52.6	1.42 ± 0.40	13.1
24	2014-04-18	13:03:00	12036	S20W34	M7.3	E	161.6 ± 43.4	0.19 ± 0.04	151.9 ± 20.5	0.36 ± 0.13	16.7
25	2014-09-10	17:45:00	12158	N11E05	X1.6	E	122.0 ± 36.0	0.18 ± 0.06	141.6 ± 51.4	0.19 ± 0.06	43.5
26	2014-10-22	14:28:00	12192	S14E13	X1.6	C	163.3 ± 40.5	0.74 ± 0.23	175.0 ± 37.7	0.79 ± 0.18	53.0
27	2014-10-24	21:41:00	12192	S22W21	X3.1	C	179.1 ± 53.5	1.67 ± 0.43	161.2 ± 16.2	0.94 ± 0.21	73.1
28	2014-11-07	17:26:00	12205	N17E40	X1.6	E	297.5 ± 68.8	4.31 ± 0.51	342.1 ± 70.1	3.86 ± 0.52	4.6
29	2014-12-04	18:25:00	12222	S20W31	M6.1	C	383.0 ± 102.9	0.55 ± 0.12	391.3 ± 37.0	0.58 ± 0.06	11.0
30	2014-12-17	4:51:00	12242	S18E08	M8.7	E	142.9 ± 9.7	4.55 ± 0.62	177.5 ± 6.4	4.50 ± 0.70	20.4
31	2014-12-18	21:58:00	12241	S11E15	M6.9	E	165.0 ± 8.2	4.76 ± 0.26	172.5 ± 7.8	4.62 ± 0.33	8.1
32	2014-12-20	0:28:00	12242	S19W29	X1.8	E	275.0 ± 20.1	5.70 ± 0.72	245.8 ± 10.7	6.63 ± 0.95	5.7
33	2015-03-12	14:08:00	12297	S15E06	M4.2	C	243.0 ± 38.7	1.17 ± 0.19	217.7 ± 28.3	1.32 ± 0.23	5.6
34	2015-06-22	18:23:00	12371	N13W06	M6.5	E	172.5 ± 6.6	8.25 ± 0.43	172.9 ± 7.6	7.32 ± 0.44	6.4
35	2015-06-25	8:16:00	12371	N12W40	M7.9	E	220.8 ± 10.5	6.92 ± 0.44	150.8 ± 8.9	6.90 ± 0.56	8.1
36	2017-09-04	20:33:00	12673	S10W11	M5.5	E	145.8 ± 109.6	0.48 ± 0.29	157.9 ± 106.2	0.36 ± 0.21	15.4
37	2017-09-06	12:02:00	12673	S09W34	X9.3	E	383.3 ± 98.19	22.25 ± 5.39	437.2 ± 133.3	19.75 ± 8.77	6.5

Table 4.1 Table continued.

5

Evolution of reconnection flux during eruption of magnetic flux ropes

5.1 Introduction

Coronal Mass Ejections (CMEs) are composed of clouds of magnetized plasma that are expelled from the Sun into the heliosphere due to sudden release of free magnetic energy stored in the twisted coronal magnetic field (Chen, 2017). They are of interest due to scientific and technological reasons since CMEs can drive interplanetary shocks that energize solar particles and cause significant space weather effects in the geospace. In-situ data obtained by satellites passing through the interplanetary CMEs (ICMEs) have established that typical ICMEs have the structure of highly twisted MFR (Wang et al., 2016; Hu, 2017). Many CME models therefore incorporate a magnetic flux rope– consisting of helical field lines twisting about a central axis in the corona as the basic underlying magnetic field structure for CME precursors (Titov &

Démoulin, 1999; Gibson & Fan, 2006; Duan et al., 2019; Liu, 2020; Chen, 2017). Therefore, understanding their evolution in early phase is crucial for CME studies.

Although is it widely accepted that MFRs constitute the core structure of the CMEs, it remains unknown wheather MFRs exist in the solar corona before CME initiation or forms during the eruption (Chen, 2011; Patsourakos et al., 2020). Some opine that the MFR could exist prior to eruptions (Cheng et al., 2011), although there is no consensus on how and where an MFR might form. An alternate hypothesis is that the MFRs can bodily emerge from the below the photosphere (Fan, 2001; Martínez-Sykora et al., 2008; Magara, 2004; Archontis et al., 2009). Yet another proposition is that the MFRs can be built directly in the corona via shearing of magnetic footpoints and reconnection prior to the eruption (van Ballegooijen & Martens, 1989; Amari et al., 2003; Aulanier et al., 2010; Chatterjee et al., 2016). Most eruptions, particularly those originating from solar active regions (ARs), occur along magnetic polarity inversion lines (PILs) within strong field regions. Furthermore, some flare-productive ARs exhibit relatively short time interval between successive eruptions, while displaying very similar structure in the flare emissions and CME morphology. Such kind of event has been known as homologous eruptions (Zhang & Wang, 2002). Observations indicate that the evolution of the source regions of homologous events is often characterized by continuous shearing motion (Li et al., 2010; Romano et al., 2015, 2018; Sarkar et al., 2019), sunspot rotation (Régnier & Canfield, 2006; Zhang et al., 2008), and flux emergence (Nitta & Hudson, 2001; Sterling & Moore, 2001; Ranns et al., 2000; Dun et al., 2007; Xu et al., 2017).

There exists several models to explain the slow build up and abrupt release of energy in solar eruptions (Forbes et al., 2006; Shibata & Magara, 2011; Chen, 2011; Schmieder et al., 2013; Aulanier, 2014; Janvier et al., 2015). The two models widely used for homologous eruptions using magnetohydrodynamics (MHD) simulations are - the breakout reconnection models (DeVore & Antiochos, 2008) and the tether cutting (Fan, 2010). The breakout model invokes a multipolar magnetic configuration with a null point located above a central flux system which is sheared by photospheric motion. As the shearing increases, the magnetic reconnection begins at the null point above the newly forming flux rope. This reconnection process acts as a trigger for an eruption, When the eruption occurs, it removes the overlying magnetic field above the core that was previously restraining the core. After the eruption, the original magnetic structure is restored (Antiochos et al., 1999; Wyper et al., 2017; Lynch et al., 2008). Continuous shearing motions can result in the repetition of such mechanisms and give rise to multiple eruptions, which otherwise tend to be confined DeVore & Antiochos (2008). On the other hand, the tether-cutting model suggests that once a coronal flux rope is formed in the corona, its slow rise is governed by reconnection between the field lines of the twisted flux

rope and the ambient field lines of the corona (Chen & Shibata, 2000; Archontis & Hood, 2008; Fan, 2010). The reconnection site usually lies below the rising flux rope. Chatterjee & Fan (2013) demonstrated repeated CMEs caused by a highly twisted flux tube emerging into the solar corona. In their simulation, a coronal flux rope partially erupted and reformed multiple times aided by partial internal reconnection between the legs of the flux rope. However, the time between eruptions was too short for the magnetic field to fully stabilize before the next eruption occurred.

Although magnetic reconnection can only be indirectly observed, it is a critical process in the solar corona that forms closed loops and energizes the plasma and particles leading to impulsively enhanced flare radiation. The observed correlation between the evolution of the CME kinematics and that of the flare X-ray fluxes suggests that the CME eruption is related to the reconnection (Zhang et al., 2001; Bein et al., 2012; Patsourakos et al., 2013), consistent with CME initiation models (Chen, 2011). Magnetic reconnection almost always occurs during a CME eruption yet it remains unclear whether reconnection initiates the eruption or a consequence. The morphological evolution of flare emission in the lower atmosphere has also been used to infer the reconnection process in the corona (Forbes & Priest, 1984; Kopp & Poletto, 1986). Due to the difficulty in observing CME evolution and measuring CME acceleration in the low corona, many studies instead compare the CME velocity measured at a few solar radii after the peak acceleration phase and the magnetic flux reconnected during the flare. Note that most of the studies have focused on an instant after the peak phase (Qiu & Yurchyshyn, 2005; Pal et al., 2018; Gopalswamy et al., 2018) and it is unclear whether the reconnection flux is related to the speed during the CME evolution. Numerical MHD simulations have proven to be powerful tools for reproducing the time-dependent, nonlinear evolution of 3D magnetic configurations and investigating the temporal changes in flux during the early phases of magnetic flux rope (MFR) eruptions. A key property characterizing solar flares is the amount of magnetic flux passing through the reconnection sheet beneath the MFR, commonly referred to as the reconnection flux (Gopalswamy et al., 2017). While the reconnected flux cannot be measured directly from observations of the corona, a quantitative relationship between the reconnection flux in the corona is the magnetic flux swept by the flare ribbon or the foot points of the magnetic flux rope (Kazachenko et al., 2017; Qiu et al., 2004).

In this paper, we conduct a 3-dimensional compressible MHD simulation to study the time evolution of the reconnection flux and find the correlation with the acceleration of the magnetic flux rope during its early evolution. Next we aim at verifying the signatures in observations. While, an ideal event required to estimate the reconnection flux correctly should be an on-disk event, the perfect event to calculate the ejection speed of the CME is instead a limb event. With

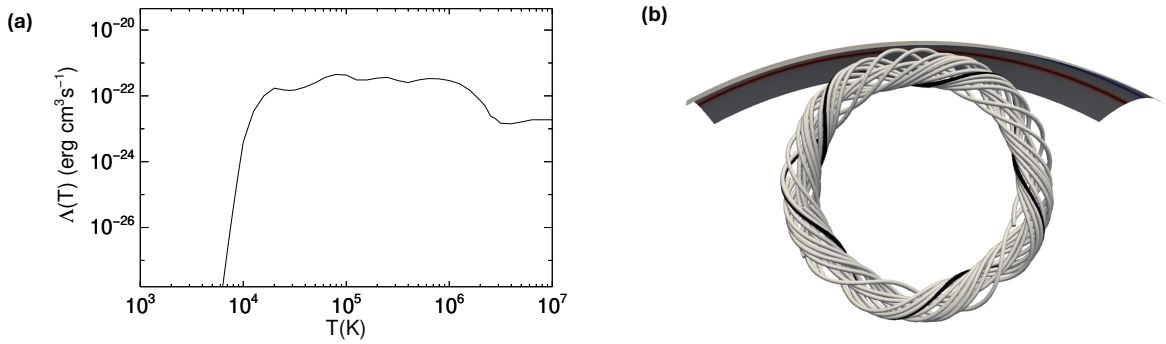

Fig. 5.1 (a) The radiative cooling function in used in this work is a modified version of Cook et al. (1989). (b) The twisted torus before emerging through the bottom boundary at $r = R_\odot$. The number of turns of one of the field lines is shown in black.

the availability of multiple vantage points due to Stereo-A and SDO spacecraft provides an opportunity to check for particular events captured simultaneously by both spacecrafts. We analyse one of such rare events using coronagraph data from stero-A and EUV data from AIA instrument of SDO. The observational data and methods are described in § 2, the numerical setup is presented in § 3. The results are presented in § 4 and finally we summarize our work.

5.2 Numerical Model

We numerically solve the complete magneto-hydrodynamic equations in three-dimensional spherical coordinates to investigate the early evolution of magnetic flux ropes in the solar corona. For this, we employ the Pencil Code (Pencil Code Collaboration et al., 2021), an open-source, highly modular, and MPI-parallelized code designed for compressible MHD flows [1]. Utilizing a sixth-order finite difference scheme and a third-order Runge-Kutta time-stepping method—among various other options provided by the Pencil Code—we solve the following set of compressible MHD equations.

$$\frac{\mathrm{D}\ln\rho}{\mathrm{D}t} = -\nabla\cdot\mathbf{U} \tag{5.1}$$

[1] http://pencil-code.nordita.org

$$\frac{\mathrm{D}\mathbf{U}}{\mathrm{D}t} = -\frac{\nabla p}{\rho} + \frac{GM_{\odot}}{r^2}\hat{\mathbf{r}} + \frac{\mathbf{J}\times\mathbf{B}}{\rho} + \mathbf{F}_{\mathrm{corr}} + \rho^{-1}\mathbf{F}_{\mathrm{visc}} \tag{5.2}$$

$$\frac{\partial \mathbf{A}}{\partial t} = \mathbf{U}\times\mathbf{B} - \eta\mu_0\mathbf{J} \tag{5.3}$$

$$\begin{aligned}\rho c_v T\frac{\mathrm{D}\ln T}{\mathrm{D}t} &= -\rho c_v T(\gamma-1)\nabla\cdot\mathbf{U} + \eta\mu_0\mathbf{J}^2 + 2\rho\nu\mathrm{S}_{ij}^2 \\ &\quad +\nabla\cdot\mathbf{q}_{\mathrm{cond}} - \rho^2\Lambda(T) + \mathscr{H} + \rho\zeta_{\mathrm{shock}}(\nabla\cdot\mathbf{U})^2\end{aligned} \tag{5.4}$$

In the above, **U** is the velocity field; **B** is the magnetic field; **A** is the magnetic potential; **J** is the current density; ρ, p and T are, respectively, the plasma density, pressure and temperature of the system; c_v is the specific heat at constant volume. The viscous force is modelled as

$$\rho^{-1}\mathrm{F}_{\mathrm{visc}} = \nabla\cdot(2\rho\nu\mathbf{S}) + \nabla(\rho\zeta_{shock}\nabla\cdot\mathbf{U}) \tag{5.5}$$

where ν is kinematic viscosity and S is the traceless rate-of-strain tensor. The coefficients ζ_{shock}, represents shock viscosity which is given by

$$\zeta_{shock} = \nu_{shock}\langle max_3[(-\nabla\cdot\mathbf{U})_+]\rangle$$

where $\langle max_3[(-\nabla\cdot\mathbf{U})_+]\rangle$ means that at each grid point, a value is assigned corresponding to the maximum positive flow convergence ($-\nabla\cdot\mathbf{U} > 0$) within three neighboring grid points along each spatial dimension. The resulting values are then smoothed using a running mean over three neighboring grid points in each coordinate direction.

Additionally, we incorporate a semi-relativistic Boris correction F_{corr} into the classical MHD momentum equation to reduce numerical diffusion and avoid the need for excessively small time steps in MHD simulations, achieved by using an artificially reduced speed of light (Chatterjee, 2020).

We include radiative cooling in our model, represented in equation (5.4), where $\Lambda(T)$ denotes the radiative loss function as described by (Cook et al., 1989). It was derived from spectroscopic analysis of emission from different elements (e.g., Mg, H, Si, He, C, S, N, O, Fe, Ne, Ca, Ni) present in solar corona and adding their individual contribution, Λ_i, to the radiative power, P, such that $P(\mathrm{ergs\,cm^{-3}\,s^{-1}})$=$n_e(\mathrm{cm^{-3}})n_{\mathrm{H}}(\mathrm{cm^{-3}})\sum_i\Lambda_i(\mathrm{ergs\,cm^3\,s^{-1}})$. Here, n_e and n_{H} are the number density of the electrons and Hydrogen atoms. The cooling function is plotted in left panel of Figure (5.1). Furthermore, we use a simplified coronal heating function, $\mathscr{H}$, that

varies only with height, following an exponential decay.

$$\mathscr{H} = \frac{F}{L_H}\frac{R_\odot^2}{r^2}\exp\{-(r-R_\odot)/L_H\} \tag{5.6}$$

where the input energy flux density is $F = 9.74\times10^5\,\mathrm{erg\,cm^{-2}\,s^{-1}}$ and the decay length is $L_H = 1.948\times10^{10}\,\mathrm{cm}$.

We have also included field-aligned Spitzer thermal conduction in our model. Here we have used the hyperbolic diffusion equation approach instead of directly including Spitzer conduction in equation (5.4), similar to Chatterjee (2020).

Let $\mathbf{q}_{\rm cond}$ represents the solution of the non-Fickian transport equation and $\mathbf{q}_{\rm sp}$ denotes the conduction flux according to the Spitzer model. We solve the following equation for the heat flux $\mathbf{q}_{\rm cond}$.

$$\frac{\partial \mathbf{q}_{\rm cond}}{\partial t} = -\frac{\mathbf{q}_{\rm cond}-\mathbf{q}_{\rm sp}}{\tau_{sp}} + \beta(dr\cdot\nabla)^6\mathbf{q}_{\rm cond} \tag{5.7}$$

where $\mathbf{q}_{\rm sp} = K_{sp}T^{5/2}\hat{\mathbf{b}}(\hat{\mathbf{b}}\cdot\nabla T)$, $\hat{\mathbf{b}}$ denotes the unit vector along the field direction and $K_{sp} = 10^{-6}\ \mathrm{erg\,K^{-7/2}\,cm^{-1}\,s^{-1}}$. τ_{sp} represents a finite timescale for $\mathbf{q}_{\rm cond}$ to evolve toward the Spitzer heat flux and is set to 0.1 s. Our time step varies between 0.1 - 0.3 ms. While our setup includes most of the relevant physics, solar wind is not included at the moment.

The computational domain consists of a spherical wedge with an extent $R_\odot < r < 6R_\odot$, $5\pi/12 < \theta < 7\pi/12$ and $-\pi/9.6 < \phi < \pi/9.6$. It is resolved by a grid of $512\times288\times160$, which is non uniform in r but uniform in θ and ϕ. The grid spacing in r is $dr = 0.002R_\odot$ at the lower boundary which gradually increases in a logarithmic manner reaching $dr = 0.003R_\odot$ at the upper boundary. Although the lower boundary in our setup is set at $R_\odot$, it does not represent the photosphere; instead, it serves as the lower coronal boundary.

We consider a high-temperature coronal plasma as an ideal gas with an adiabatic constant of $\gamma = 1.66$. Initially, the domain is assumed to be in the state of a hydrostatic equilibrium at a uniform temperature of $T_0 = 10^6\,\mathrm{K}$ with a density stratification given by

$$\rho = \rho_0\exp\left\{-\frac{R_\odot}{H_{p_0}}(1-\frac{R_\odot}{r})\right\} \tag{5.8}$$

Here, $\rho_0 = 1.0 \times 10^{-15}$ g cm^{-3} is the initial density and the initial pressure scale height is given by $H_{p_0} = c_{s_0}^2/g_r$, where c_{s_0} denotes the initial sound speed and g_r represents the gravitational acceleration at the solar surface. The initial atmosphere consists of a pre-existing potential field with arcade like geometry as given in Fan (2012) (see their Equation 12 and 13).

At the lower boundary, we impose an electromotive force given by

$$\mathbf{E}\,|_{r=R_\odot} = -\frac{1}{c}\mathbf{v}_0 \times \mathbf{B}_{\text{torus}}(R_\odot, \theta, \phi, t)$$

which bodily transports the twisted torus radially into the domain. The major and minor radius of the torus are $0.25R_\odot$ and $0.042R_\odot$ respectively and with a field line twist rate of

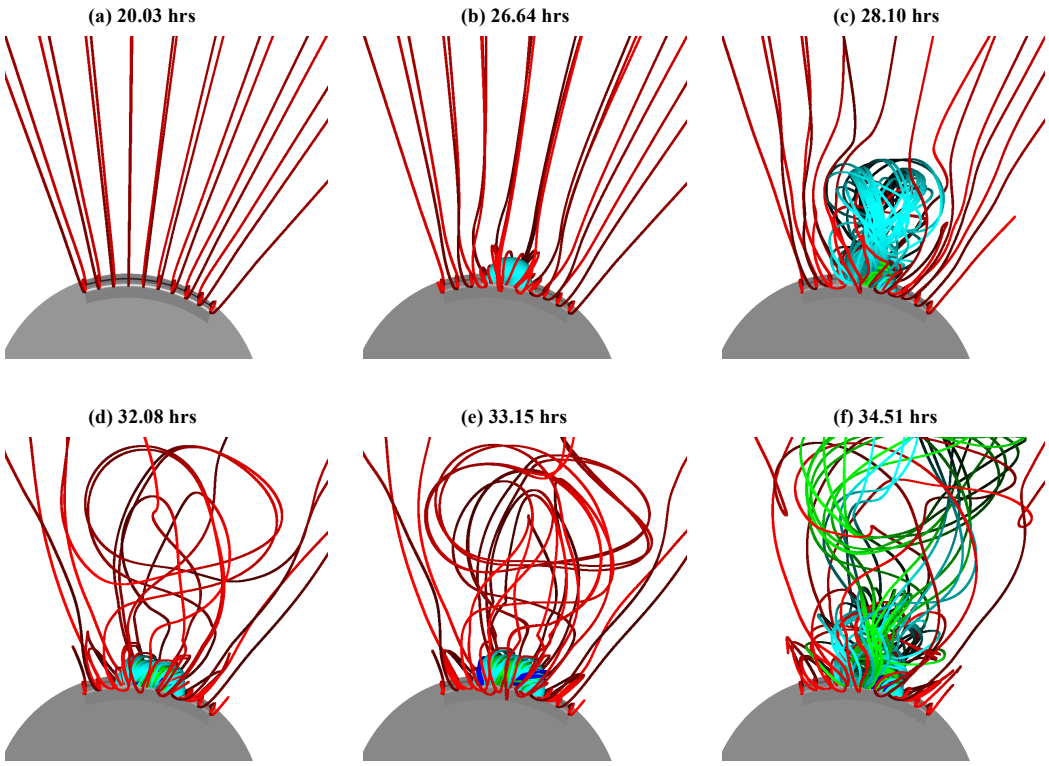

Fig. 5.2 The 3D evolution of the magnetic field of the twisted flux rope emerging into the corona at the specified times (in hours). Red field lines have footpoints in the ambient arcade, while blue, green, and cyan field lines originate from the emerging flux region. An animation of this evolution is available in the online journal with a running time of 36 s. The period covered by the animation (in solar hours) spans from $t = 19.65$ hrs to $t = 40.25$ hrs from the start of the simulation. The flux rope starts emerging into the corona at $t = 20.3$ hrs.

$0.068\,\mathrm{rad\,Mm^{-1}}$. The twist rate indicates the field line winds around the tube axis per unit length along the axis. The flux tube is initially located at $r_0 = 0.705R_\odot$, thus the torus is initially entirely below the surface and moves bodily upward toward the lower boundary at constant speed, until it reaches a height r_{stop} when the emergence is stopped and a part of the torus is still inside of the computational domain. The velocity field at the lower boundary is specified to be uniform in the region where the emerging torus intersects the lower boundary and its zero everywhere else. The imposed emergence speed, $v_0 = 2\,\mathrm{km\,s^{-1}}$, which is much smaller than the Alfven speed $v_A = 1.69\,\mathrm{Mm\,s^{-1}}$ to ensure that the emerging flux rope is allowed to evolve quasi-statically during the flux emergence phase at the lower boundary. The method for introducing a twisted torus structure into the domain quasi-statically from the lower boundary using an electromotive force is well-known and has been used by Fan (2009, 2010, 2012, 2017) and Chatterjee & Fan (2013). It is a technique that gradually introduces the flux rope into the corona. The corona is expected to be in a force-free equilibrium state at all times. We avoid adding the flux rope suddenly into the corona as that may lead to numerical perturbations that disturb the existing equilibrium and perhaps trigger an unphysical eruption. It is desirable to discourage this possibility and to be sure that the loss of equilibrium is indeed due to MHD instabilities like torus and helical kink rather than numerical. When the emergence is stopped, the velocity at the lower boundary is set to zero, with no inflows or outflows and footpoints are rigidly anchored. For the θ boundaries, we assume a non-penetrating stress-free boundary for the velocity field and perfectly electrically conducting walls for the magnetic field. The ϕ boundaries are periodic. For the top boundary, we use a simple outward extrapolating boundary condition that allows plasma and magnetic field to flow through.

In this simulation, we drive the emergence of the torus until the center reaches $r_{\mathrm{stop}} = 0.85R_\odot$ from $r_{\mathrm{start}} = 0.707R_\odot$ to study the reconnection flux during the evolution of the twisted flux rope in the corona which produces homologous CMEs.

5.3 Results

Our simulation produces two homologous CME eruptions; each of the eruption characterized by an impulsive increase of the kinetic energy and corresponding release of the magnetic energy. We first briefly discussed the initiation and evolution of the eruptions and then analyze the velocity and reconnection flux of different CME eruptions in the simulation. Note that the magnetic reconnection in our model using MHD approximation is of numerical origin, we

cannot resolve length scales smaller than the Larmor radius of the proton or the mean free path. However, our goal here is to find a relation (if any exists) between the reconnection flux and the speed of the ejecta in our simulations.

5.3.1 Synthetic eruptions

The simulation begins with a magnetic flux rope (MFR) emerging from the lower boundary and pushing into a pre-existing coronal potential arcade field. The normal magnetic flux distributions at the lower boundary are represented by bipolar bands $B_r(R_\odot, \theta, \phi) = B_s(\theta)$ where the $B_s(\theta)$ denotes the potential arcade field at the lower boundary, as shown in Figure (5.2). The emergence process is halted once a specified amount of twisted flux is driven into the corona. Although the imposed emergence of a twisted flux rope through the lower boundary may not perfectly reflect real-world conditions, it serves as a means to achieve a sequence of near-force-free coronal flux rope equilibria with increasing amounts of locally detached, twisted flux. In all cases, we observe the development of current layers with a sigmoid morphology beneath the flux rope. Magnetic reconnection within these current layers continues to add flux

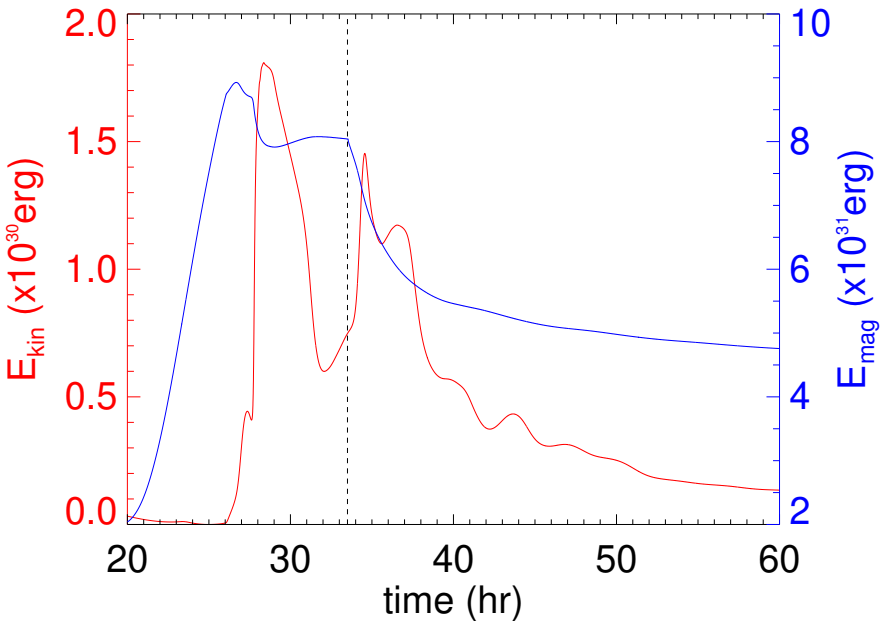

Fig. 5.3 Total kinetic energy E_{kin} (red) and total magnetic energy E_{mag} (blue) as a function of time. The dashed vertical line represents the time when the flux emergence stops.

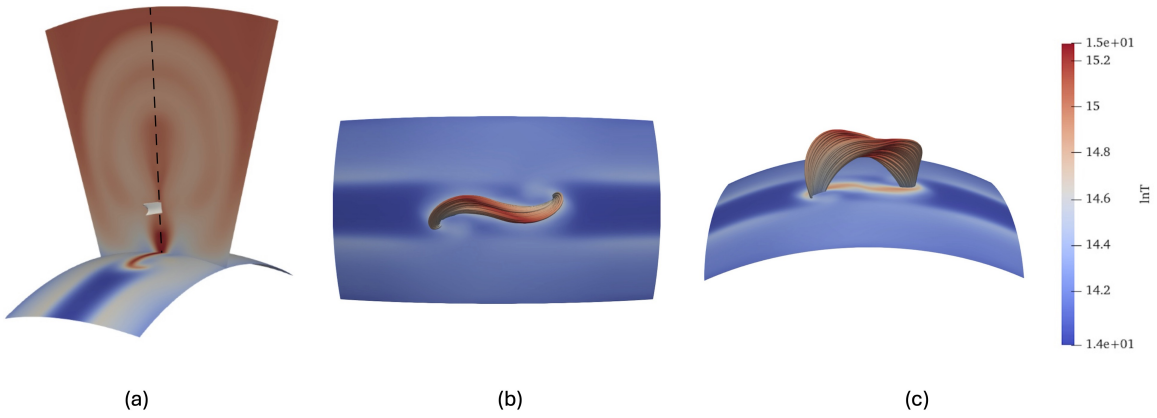

Fig. 5.4 Identification of current sheet and field lines of the flux rope from different viewing angles. The current sheet (in white) traced from the temperature isosurface with a value $\log_{10} T = 6.6$ shown in panel (a). The height of the current sheet iso-surface (white) is about $1.4 R_{\odot}$. The field lines passing through such sheets gives the reconnection flux. The sigmoid fieldlines are shown in panels (b) and (c). The time in all these panels are taken at $t = 27.32$ hours.

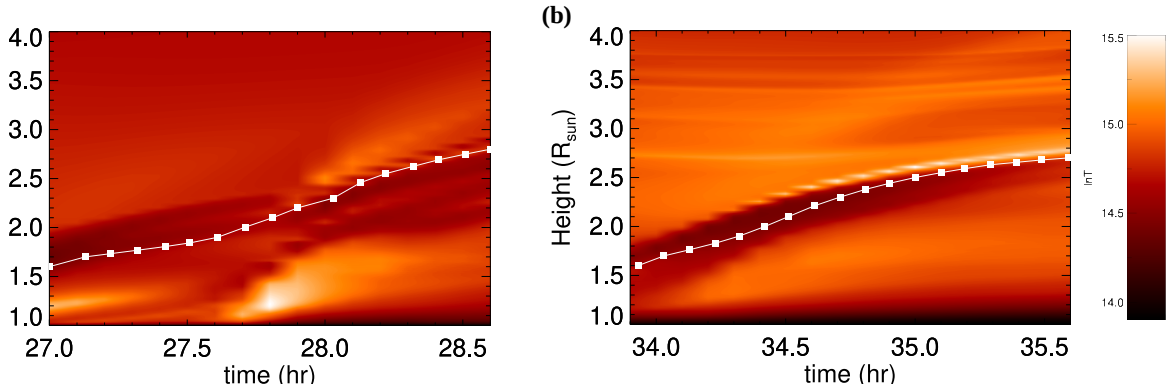

Fig. 5.5 (a) Height time profile of the core of the flux rope before and after the first eruption at $t = 27.9$ hours. The height is calculated by tracking the dark region (flux rope) in the temperature profile. (b) Same as (a), but for the second eruption at $t = 34.7$ hours.

to the flux rope, even though the total magnetic energy gradually decreases due to reconnections. This continuous addition of flux facilitates successive eruptions.

The first eruption is triggered when the twist of the winding of the flux rope field lines about the torus axis reaches approximately 1 wind between the anchored foot points. We stopped the emergence of the twisted torus tube at 33.5 hours when the extent of the flux rope

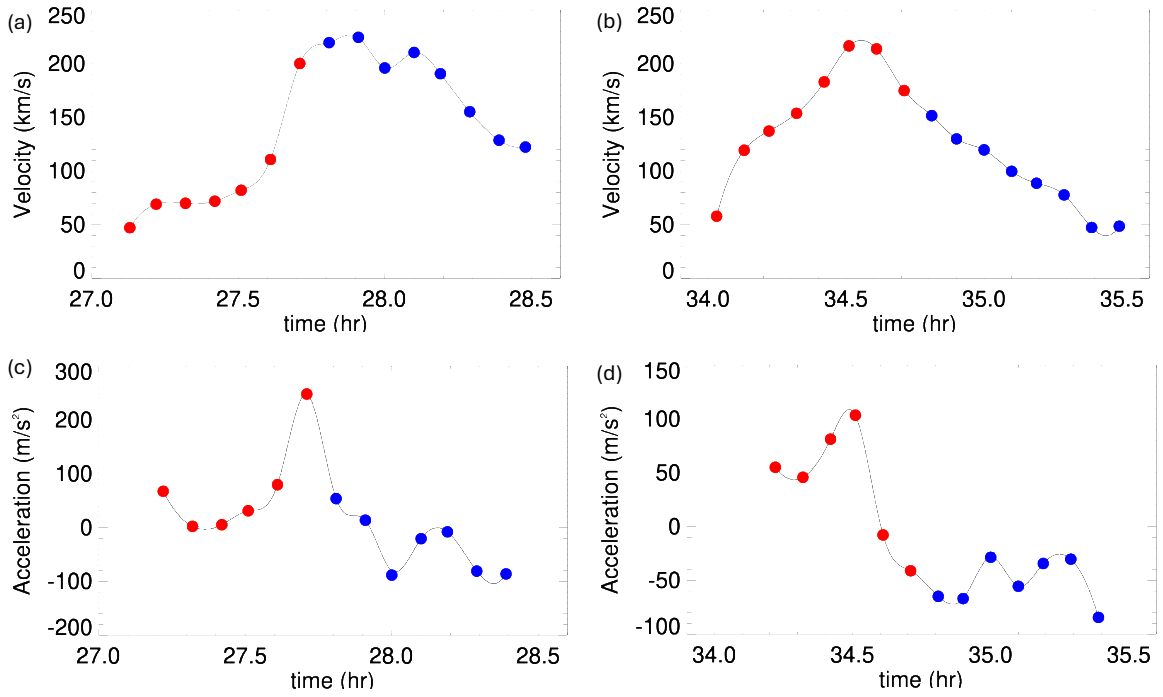

Fig. 5.6 Time evolution of velocity, (a)-(b), and acceleration, (c)-(d), for both the eruptions in the simulation. The velocity is calculated by tracking the flux rope in the central meridional plane. The smoothing is done by cubic spline. The reconnection flux is calculated by the magnetic flux passing through the footpoints of the fieldlines as well as through the current sheet shown in Fig. 5.4a. The red (blue) circles are used to represent simulation data before (after) the eruption.

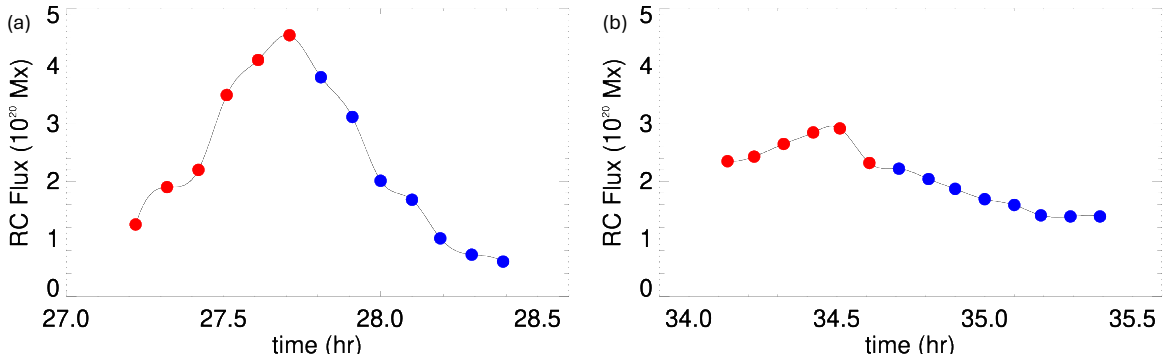

Fig. 5.7 Time evolution reconnection flux. The reconnection flux is calculated by the magnetic flux passing through the footpoints of the fieldlines as well as through the current sheet shown in Fig. 5.4a. The red (blue) circles are used to represent simulation data before (after) the eruption. The smoothing is done by cubic spline.

that emerged is such that the field line's winding about the flux rope's axis is 1.5 between anchored footpoints. This is estimated in a simple way by multiplying the total number of winds around the circular torus, i.e., 5 winds, by the fraction of the torus circumference above the solar surface. The second eruption began after we stopped the flux emergence. The helical kink instability is expected to develop in a line-tied coronal flux rope if the total windings of the field line twist around the axis exceed a critical value between the line-tied ends (Hood & Priest, 1981; Török & Kliem, 2003; Török et al., 2004). This critical value is 1.25, based on the analytical calculation of a uniformly twisted cylindrical flux tube (Hood & Priest, 1981). The animation (corresponding to Figure 5.2) clearly shows substantial writhing motion at the onset of the eruption for the second eruption but not in first eruption, indicative of the helical kink instability. Figure 5.3 illustrates the evolution of kinetic and magnetic energies for both eruptions. The time at which the kinetic energy reaches its peak is designated as the eruption time.

Furthermore, we examined whether the flux rope is also unstable to the torus instability (Bateman, 1978; Kliem & Török, 2006; Isenberg & Forbes, 2007), which is triggered by a vertical force imbalance between the upward hoop force and the downward strapping force acting on the magnetic flux rope (MFR). The external strapping field is assumed to be the potential field B_p with the same normal distribution at the lower boundary. The rate of decline with height is measured by the decay index $n = -d\ln B_h/d\ln h$. The critical decay index for a 3D line-tied arched flux rope has been calculated by Isenberg & Forbes (2007) to be close to 1.7. In this work, for a decay index of 1.7, the critical heights are 1.21 $R_\odot$ and 1.28 $R_\odot$, respectively for the two successive eruptions. The height of the apex of the axial field line of the coronal flux rope, estimating it to be 1.6 $R_\odot$ and 1.7 $R_\odot$ for the two successive CMEs at the time of eruption calculated by tracking the flux rope over the course of their evolution (see Appendix). For both eruptions, the flux rope crosses the critical threshold of height, indicating that it is also torus unstable. This indicates the fundamental role of kink instability and torus instability in triggering ejective eruptions of a 3D line-tied coronal flux rope.

The panels (a) and (b) of Figure 5.6 illustrate the radial velocity of the flux rope during both eruptions. These velocities were determined by tracking the apex of each flux rope throughout their evolution. The height-time plot is produced by tracking the dark region in the $r-\theta$ plane of the temperature profile, which represents the MFR. By following this dark region consistently, we determine the MFR's velocity during the flux rope's evolution.

The first ejection has a peak radial velocity of 224 $\mathrm{km\,s^{-1}}$, which is slightly higher than the 213 $\mathrm{km\,s^{-1}}$ velocity of the second CME respectively. This observation is understood by

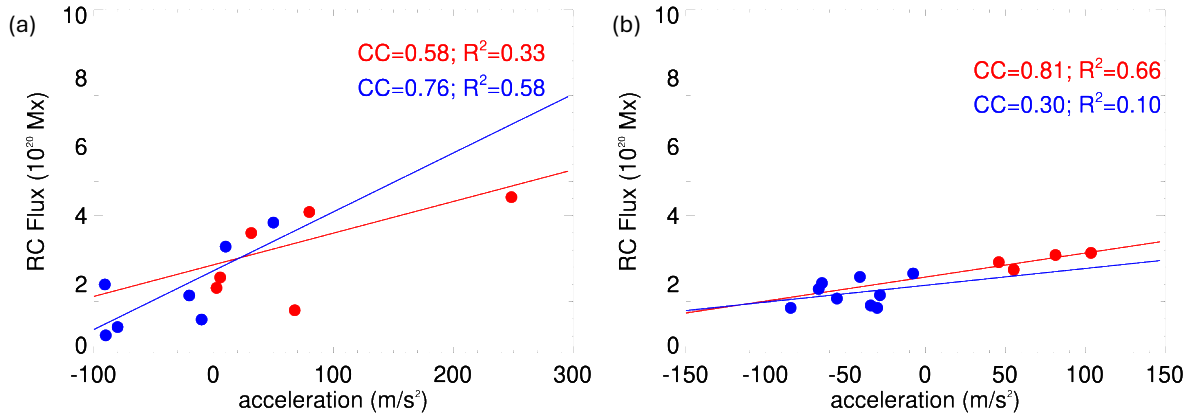

Fig. 5.8 (a) CME reconnection flux vs acceleration plot for the first eruption during the evolution. Red circles represents data before the eruption whereas the right circles represents after the eruption. The solid line is the linear fit to the points before the eruption, (b) Same as (a) but for the second eruption.

the time versus kinetic energy plot, which shows the second CME registered lower kinetic energy than its precursor. The initial eruption occurs at a radial distance of $1.9R_{\odot}$, while the second eruption takes place at $1.8R_{\odot}$. Due to the lower velocity of the second eruption, there is no interaction between the two CMEs. An interesting observation is that the velocity starts to decrease after the eruption which is also observed in observational data. This could be attributed to the absence of solar wind, which normally drives the magnetic flux rope (MFR) further into the heliosphere post-eruption. The panels (c) and (d) of Figure 5.6 depicts the acceleration for both eruptions. The first ejection has a peak acceleration of 250 $\mathrm{m\,s^{-2}}$, which is higher than the 103 $\mathrm{m\,s^{-2}}$ peak acceleration of the second CME respectively.

The panels (a) and (b) of Figure 5.6 depicts the changes in reconnection flux over time for both eruptions. We monitored the hottest region beneath the flux rope in the r-θ plane both before and after the eruption as shown in Figure 5.4). This region corresponds to the current sheet, as the current sheet typically exhibits higher temperatures compared to the surrounding areas. By tracking the same hottest region, we can effectively identify the current sheet and quantify the flux passing through it. The reconnection flux passing through the sheet is given by

$$\phi_{RC} = \int B_n \, dS = \int B_r \, dA$$

where B_n represents the magnetic flux normal to the elemental area dS of the current sheet, and B_r is the radial magnetic field in the ribbons, which are the footpoints of newly reconnected magnetic field lines at the lower boundary. The term dA denotes the elemental area of these footpoints. Thus reconnection flux is determined by calculating the magnetic flux swept by the newly formed field lines passing the lower boundary. Direct measurement of B_n and dS within the current sheet is not feasible, even in simulations, due to the intricate structure of the reconnection sheet. However, B_r and dA are relatively straightforward to calculate, even for a spherical wedge-shaped domain. Therefore, this approach provides an indirect but well-defined measure of the magnetic flux passing through the reconnection sheet. This method allows for an effective evaluation of the magnetic reconnection process by focusing on the measurable quantities at the footpoints, offering valuable insights into the dynamics of the reconnection events. Since we calculate only the newly reconnected flux for any given snapshot (taken at a cadence of 12 min), it is also called the instantaneous reconnection flux (RC). Henceforth, for brevity, we will use RC flux to imply the instantaneous reconnection flux in the rest of the thesis.

The peak reconnection flux (RC flux) for the first and second eruptions are 4.94×10^{20} Mx and 2.92×10^{20} Mx, respectively. The panels (a) and (b) of Figure 5.7 indicate that the reconnection flux decreases after reaching its peak value, with the eruptions occurring near the maximum reconnection flux. This phenomenon might be explained by the intricacies of calculating the reconnection flux. When an eruption occurs, the reconnection sheet breaks down, making it challenging to track the field lines passing through the current sheet (CS).

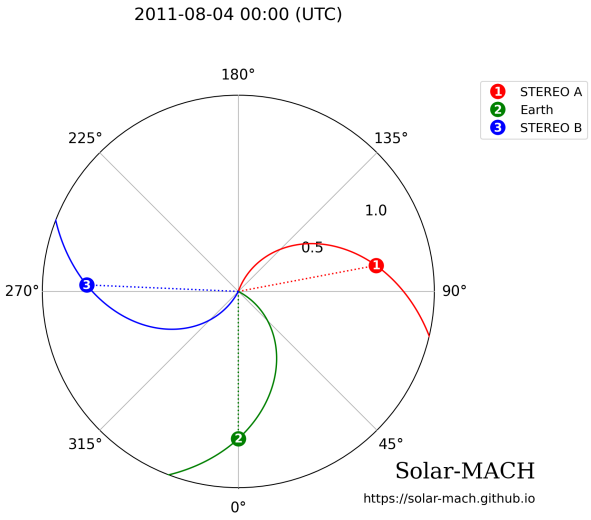

Fig. 5.9 Location of STEREO spacecraft and Earth on 2011 August 4.

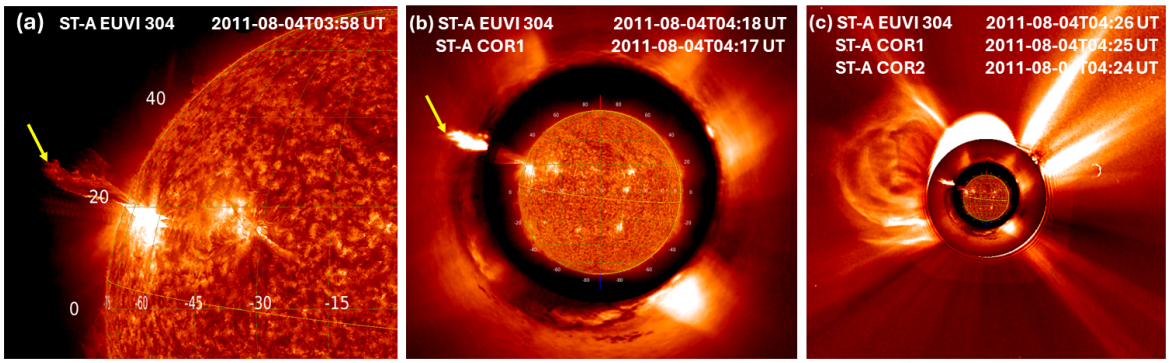

Fig. 5.10 Different phases of the filament eruption on 2011 August 04 as observed by STEREO-A. (a) Image of the Sun in STEREO-A EUVI 304 Å (b) COR1 image superimposed with STEREO-A EUVI 304 Å (c) Superimposed images of STEREO-A EUVI 304 Å , COR1 and COR2. The yellow arrows in panels (a) and (b) indicate the filament leading edge. The images are plotted using JHelioviewer (https://www.jhelioviewer.org/).

5.3.2 Observed eruption

We now focus on finding signatures of such correlation if any between reconnection flux and CME speed in solar observations. We study the temporal evolution of an M-class flare (SOL2011-SOL2011-08-04T03:41) which occurred in AR 11261 during 2011 August 4, and which had an associated CME. During this period, STEREO-A and STEREO-B were positioned at longitudinal separations of 101° and 92° (see Figure 5.9), respectively, relative to the Sun-Earth line. This positioning allowed the two spacecraft to provide near-limb views of Earth-directed CMEs. On the other hand the location of AR 11261 was close to the solar disk center (between 30°to 35° west) relative to Earth, offering reliable magnetic field data for the active region from the Heliospheric Magnetic Imager or HMI instrument (Schou et al., 2012). This provides a unique opportunity to study the co-temporal evolution of reconnection flux, estimated from on-disk SDO data, and the speed of the associated eruption, starting from the initiation height at lower corona as observed from near-limb observations by STEREO.

We analyze the kinematics of the eruption associated with the M-class flare on 2011 August 04, by tracking the filament leading-edge height as observed by STEREO-A. We use two instruments from the Sun Earth Connection Coronal and Heliospheric Investigation (SECCHI; Howard et al. (2008)) onboard STEREO-A to track the early evolution of the Earth-directed filament eruption, which was observed as prominence eruption from STEREO-A (see Figure 5.10). The instruments include the Extreme Ultraviolet Imager EUVI ($< 1.7 R_{\odot}$), Wuelser et al. (2004) and the inner coronagraph COR1 ($1.3 - 4 R_{\odot}$), Thompson et al. (2003).

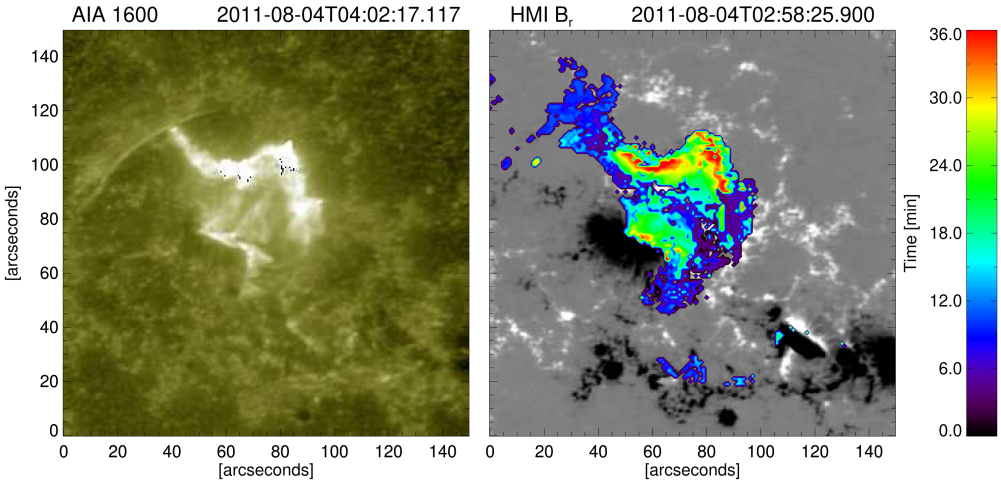

Fig. 5.11 Left panel: Flare associated brightening observed in AIA 1600 Å channel during the flare occurred in AR 11261. Right panel: The associated HMI B_r magnetic field (gray color scale with saturation value $\pm$500 Gauss) and the temporal evolution of the flare ribbons from 03:41 UT to 04:17 UT on 2011 August 04 .

We follow the method by (Kazachenko, 2023), to estimate the temporal profile of reconnecting flux. The observations of the flare ribbons are obtained from the Atmospheric Imaging Assembly (AIA; Lemen et al. (2012)) onboard SDO in 1600 Å channel. The associated full-disk magnetograms are obtained from the HMI instrument. During the recurrent eruptive M-class flare in AR 11261 on 2011 August 4, we identify the area swept out by the flare-ribbons observed in AIA 1600 Å images as shown in Figure 5.11. The half of the unsigned magnetic flux underlying the area associated with the brightening observed in AIA 1600 Å are recorded as the temporal profile of the re-connection flux. The kinematics of the filament eruption and the temporal variation in associated reconnection flux are shown in Figure 5.12.

Despite this complexity in measuring the reconnection flux from our simulation, similar patterns are observed in observational data (see panel (b) of Figure 5.12, suggesting a consistent underlying process. The observed decrease in reconnection flux post-peak might be tied to the dynamic changes within the RC sheet during an eruption. As the RC sheet disintegrates, accurately measuring and tracking the magnetic field lines through the current sheet becomes challenging. This complexity impacts the calculated values of RC flux, reflecting the real-time physical changes occurring during an eruption. Moreover, these findings align with observational data, further validating the temporal relation between the reconnection flux and the onset of eruptions (panels b-d of Figure 5.12). This highlights the importance of considering

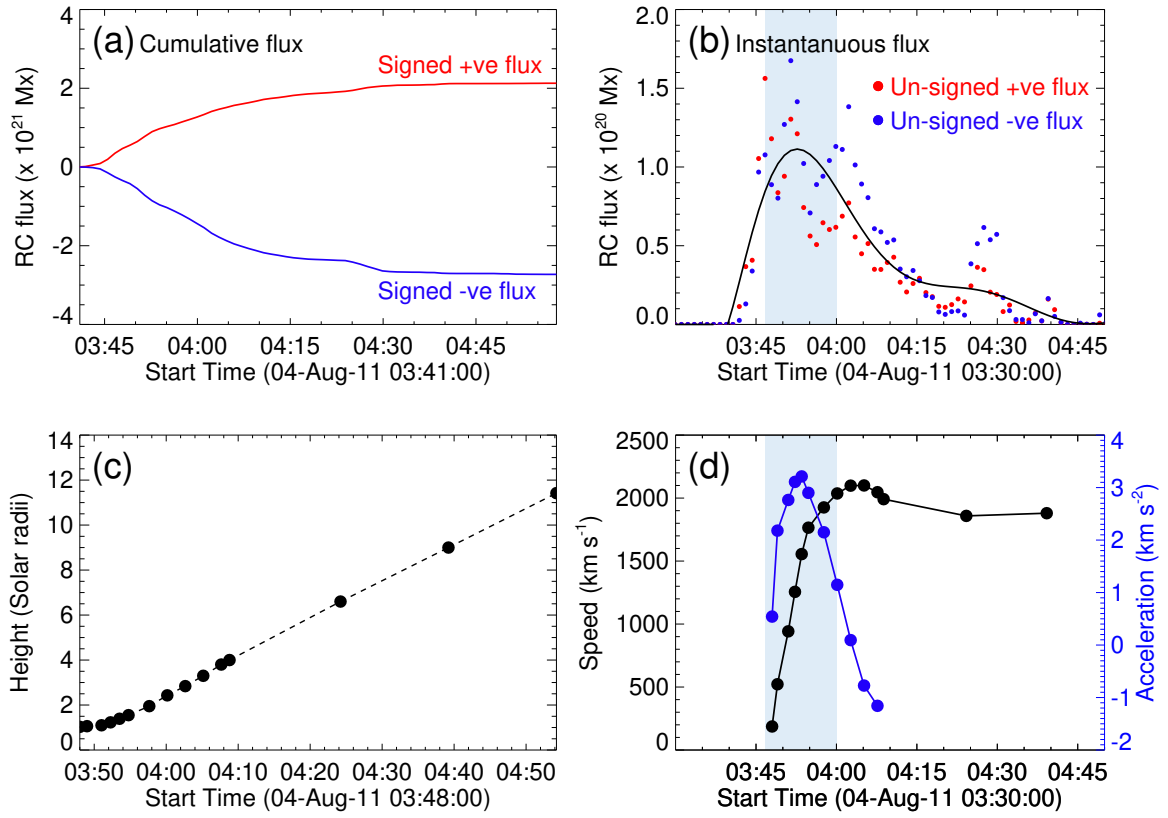

Fig. 5.12 (a) Time profile of signed cumulative reconnection flux integrated over the positive (red) and negative (blue) magnetic polarities underlying the flare ribbons. (b) Time profile of unsigned instantaneous reconnection flux integrated over the positive (red) and negative (blue) magnetic polarities underlying the flare ribbons. (c) Height time plot of the filament leading edge measured from STEREO EUVI, COR1 and COR2 for the same event as shown in Figure 5.10. (d) Velocity profile of the filament leading edge derived from Panel (c). The correlation coefficient between acceleration and instantaneous reconnection flux is 0.99 before the eruption. *by Dr. Ranadeep Sarkar.*

both the peak and the subsequent decrease in reconnection flux when studying the dynamics of solar eruptions and magnetic reconnection events.

5.3.3 Correlation between MFR acceleration and reconnection flux

The panels (a) and (b) of Figure 5.8 show scatter plots of the MFR acceleration (v_r) versus the reconnection flux (ϕ_{RC}) at different times during the evolution of the homologous synthetic

eruptions. Before the eruption, the acceleration exhibits a linear relationship with the reconnection flux for the eruptive events. Notably, the Pearson's correlation coefficients before the eruption for the two events are 0.58 and 0.81, respectively, indicating a strong correlation between the reconnection flux and the acceleration. A similar qualitative relationship is also observed in the case of observational data (see panel (d) of Figure 5.12) where the acceleration of the erupting filament and the associated reconnection flux simultaneously increase as indicated by the cyan shaded region. The correlation coefficient for this case is 0.9 and 0.98 before and after the eruption. Furthermore, note that, in the lower corona, where the influence of solar wind is negligible, our results show that the speed of the flux rope decreases following the eruption, heralding the end of the acceleration phase. The deceleration of the CME is mainly because of adiabatic expansion and resulting cooling of the magnetic cloud in a relatively large domain that we have used. This is illustrated in panels a & b of Figure 5.6 from our simulation model, which closely resembles panel d of Figure 5.12 based on our analysis of observational data. Similar findings have also been reported in Sarkar et al. (2019); Zhu et al. (2020). Due to observational constraints (limited time-cadence of STEREO EUVI), it was challenging to gather more data points during the initial acceleration phase of the eruption. The numerical analysis from our simulation complements the above-mentioned observational results, allowing us to determine the temporal evolution of the reconnection flux and acceleration and their correlation.

5.4 Summary and Discussion

Our fully compressible MHD simulation using the Pencil Code presented here produces homologous CMEs due to the repeated formation and partial eruption of unstable flux ropes during the sustained emergence of a highly twisted magnetic flux rope. Our results show that, with the continuous emergence of flux, a new current sheet (CS) forms above the same polarity inversion line (PIL) after the completion of a previous eruption, leading to a new eruption. This recurring formation and disruption of coronal current sheet, driven by the ongoing emergence of flux, results in homologous eruptions.

Our simulation began with the quasi-static emergence of a twisted flux rope at the lower boundary into a pre-existing coronal arcade. We found that the flux rope initially settles into a quasi-static rise phase, with an underlying sigmoid-shaped current layer developing beneath the flux rope. This current layer is likely the site for the formation of thin current sheets and magnetic reconnection (Titov, 2007; Aulanier et al., 2005; Savcheva et al., 2012). The

reconnection in the current layer effectively adds twisted flux to the magnetic flux rope, allowing it to rise quasi-statically before undergoing a partial eruption. Subsequent flux emergence forms a new current channel, which exhibits similar behavior and erupts after the bodily emergence stops, or $v_0 = 0$.

In both eruptions, the magnetic flux rope (MFR) undergoes the torus instability after the rope axis crosses the critical height of $\sim 1.28 R_\odot$. We estimate the twist of the field line between the line tied ends at the lower boundary before each eruption. We conclude that the first eruption remains stable to helical kink instability, while the second eruption is kink unstable. The subsequent CME, in our simulation, has a slightly lower speed and kinetic energy. Initially, the reconnection flux increases, followed by a gradual decrease, after each eruption. These trends are consistent with the observation of an eruptive event. Our simulation indicates that the reconnection process potentially influences the evolution of the magnetic flux rope. The reconnection flux shows a linear correlation with the acceleration, before the eruption. This result indicates that reconnection may play an important role in propelling the magnetic ejecta after the loss of equilibrium phase. The importance of the present work lies in performing an MHD simulation to produce homologous CMEs and thereafter finding the correlation between the reconnection flux and CME acceleration as a function of time between pre to post-eruptive stage and further validating this relation using an observed event. We choose an event that appears in the database of both STEREO (as limb event) and SDO (as on-disk event) spacecrafts so as to enable us to estimate both acceleration and reconnection flux as accurately as possible using these instruments. Despite the fact that the driving of the MHD simulation was not tailored to match the observed flare and the associated CME, the correlation between CME acceleration and reconnection flux is detected in both cases. This indicates that the correlation could be a generic property of solar eruptions.

Although our numerical simulation model does not include the solar wind, the inclusion of optically thin radiative cooling and explicit coronal heating makes it more reasonable than previously published homologous solar eruption models (Chatterjee & Fan, 2013; Bian et al., 2022). We account for localized heating due to the formation and dissipation of current sheets in the corona, as well as the redistribution of heat through field-aligned conduction. The lower boundary of our simulation domain is positioned at the coronal base rather than the photosphere, and therefore, our model does not simulate prominence formation.

Although we employ an analytical configuration of the magnetic flux rope and include various physical processes in our model, this approach may not fully represent the realistic driving conditions of the solar eruptions. To address the complexity and evolution of the

magnetic configuration in a real scenario, a detailed and accurate description of the evolving surface magnetic field is essential. Our future goal is to conduct detailed analysis of solar eruptions that are directly driven or constrained by photospheric magnetograms.

6

Discussions and future prospects

6.1 Discussions

In this thesis, we investigate the early evolution of coronal mass ejections (CMEs) in the lower corona and also emphasize the relationship between flares and associated CMEs. Using both numerical modeling and observational methods, we study these phenomena to provide a comprehensive understanding of the physics behind these energetic solar events. This dual approach addresses different perspectives of the solar eruptions, enabling us to compare our simulation results with observational data, emphasizing the crucial role of concurrent observation and simulation in understanding of solar eruptions.

The thesis starts with a concise overview of the Sun, covering its interior and atmosphere, as well as solar flares and coronal mass ejections (CMEs). We also discuss the mechanisms that initiate CMEs and their signatures in Chapter 1. Chapter 2 delves into the numerical methods

and tools, including the pencil-code, that we employed in our research. Chapter 3 provides details on the observational instruments used in various analyses throughout the thesis.

We present a study on the photospheric magnetic imprints of solar flares associated with CMEs. Solar flares often leave distinct imprints on the magnetic field at the photosphere, typically observed as abrupt and permanent changes in the downward-directed Lorentz force within localized regions of the active region. Our study aims to differentiate eruptive and confined solar flares by analyzing variations in the vertical Lorentz force. We focus on 26 eruptive and 11 confined major solar flares, all stronger than the GOES M5 class, observed between 2011 and 2017, using SHARP vector-magnetograms obtained from NASA's Helioseismic and Magnetic Imager (HMI). In addition to observational data, we incorporate data from two synthetic flares derived from a δ-sunspot simulation as reported by Chatterjee et al. 2016. Our methodology involves estimating changes in the horizontal magnetic field and the total Lorentz force integrated over areas around the polarity inversion line (PIL), which encompasses the flare locations. We developed a semi-automatic contouring algorithm to delineate the region near the PIL where the most significant magnetic changes occur.

Our study reveals that there is a rapid increase in the horizontal magnetic field along the flaring polarity inversion line (PIL), accompanied by significant changes in the downward-directed Lorentz force in the same area. A key finding is the identification of a threshold value for Lorentz force changes. We observed that all confined flares in our dataset show total Lorentz force changes of less than 1.8×10^{20} dyne, which serves as a distinguishing factor between eruptive and confined flares. Additionally, for eruptive flares where the Lorentz force change is below this threshold, we noticed a considerably larger distance between the parallel flare ribbons, usually greater than 15 Mm at the onset of the flare. This suggests a possible link between the separation of flare ribbons and the magnitude of Lorentz force change in eruptive events. Therefore, the separation between ribbons could be an additional indicator when analyzing the magnetic signatures associated with solar flares. We also applied our methodology to synthetic B & C class flare events, finding a remarkable similarity in their temporal evolution with observational data. This observation suggests that the Lorentz force propagates from the reconnection site down to the photosphere, providing valuable insights into the mechanisms that drive the upward impulse during flares, which is crucial for understanding CME dynamics. Our research improves the understanding of the magnetic and dynamic characteristics of solar flares. The ability to distinguish between eruptive and confined flares based on changes in the Lorentz force may lead to a better understanding of the relationship between sunspot topology and the occurrence of ejective flares.

In the next chapter, we explore the changes in reconnection flux during the evolution of coronal mass ejections (CMEs) from their initiation to eruption and how these changes relate to the velocity of the ejected material. CMEs are major contributors to space weather, with magnetic flux ropes (MFRs) generally recognized as their main precursors. However, the three-dimensional evolution of reconnection flux during MFRs throughout CME eruptions is still not well understood. Our comprehensive study uses a three-dimensional magnetohydrodynamic (MHD) model to investigate the temporal evolution of reconnection flux during MFR development. We combine numerical simulations with observational data for our analysis.

We start with an initial coronal setup featuring an isothermal atmosphere and a potential arcade magnetic field, with an MFR emerging at the lower boundary. Our model includes radiative cooling, a coronal heating function, and field-aligned Spitzer thermal conduction, but it does not consider the solar wind. As the MFR ascends, it stretches and compresses the overlying magnetic field, forming a current sheet and triggering magnetic reconnection. This process intensifies, leading to the impulsive expulsion of the flux rope.

Our simulation produces two homologous CME eruptions, each marked by a sharp rise in kinetic energy and a corresponding release of magnetic energy. The peak velocities of the core of the MFR of the simulated CMEs are approximately 224 $\mathrm{km\,s^{-1}}$ and 213 $\mathrm{km\,s^{-1}}$. In the first eruption, the magnetic flux rope exhibits torus instability alone, while in the second eruption, it shows both torus and kink instabilities. We examine the temporal evolution of reconnection fluxes during these two successive MFR eruptions, with twisted flux continuously emerging through the lower boundary. To complement our simulations, we also analyze observational data from NASA's Helioseismic and Magnetic Imager (HMI), the Atmospheric Imaging Assembly (AIA), and the Solar TErrestrial RElations Observatory (STEREO-A) spacecraft for a specific eruptive event.

Our results show that changes in reconnection flux significantly influence CME speeds. We find a linear correlation between CME speed and the amount of reconnection flux, underscoring the critical role of reconnection dynamics in the initiation and propagation of CMEs. This simulation provides valuable insights into the complex dynamics of CME initiation and evolution. By modeling and understanding the three-dimensional temporal evolution of reconnection flux, we gain a more precise and comprehensive understanding of the mechanisms driving CMEs, enhancing our knowledge of how reconnection flux changes during solar eruption processes.

By combining observational data with modeling, this thesis lays a strong foundation for enhancing models and methods related to the lower corona. It broadens the scope of research on solar eruptions and provides a deeper understanding of their role in solar physics.

6.2 Future prospects

Our research lays a foundation for future investigations into the origins and development of coronal mass ejections (CMEs). Moving forward, we intend to utilize our lower coronal simulation code to explore three primary areas (a) parametric study with different twist factors, (b) heliospheric simulation for lower coronal MFR to study its geo-effectiveness and (c) data constrained simulation for lower coronal model. A brief idea is given below.

Parametric study using different twist factors

In our investigation of homologous eruptions, we used a fixed twist value of the injecting torus within our coronal domain. Future studies will involve injecting a series of twist factors to analyze the statistical behavior of eruptions. We have already observed that varying relative helicity can lead to both eruptive and confined eruptions(Fan, 2012). It is possible that under certain conditions, specific twists may result in confined eruptions. We aim to determine if and how eruption velocity and acceleration correlate with the degree of twist. We'll examine how other dynamic properties, such as reconnection flux and domain temperature, change with different twist factors. This comprehensive approach will provide deeper insights into the relationship between magnetic twist and the characteristics of solar eruptions, potentially improving our understanding of the mechanisms driving coronal mass ejections.

Heliospheric simulation with lower coronal MFR to study its geo-effectiveness

We plan to expand the scope of our research to bridge the gap between lower coronal dynamics and interplanetary space weather effects. Our strategy involves to extend our current lower coronal model use as a input for heliospheric code for ICME simulations. This extension will provide crucial magnetic field data at the inner boundary of heliospheric code. We're considering coupling our extended model with heliospheric codes, particularly MS-FLUKSS

(Multi-Scale Fluid Kinetic Simulation Suite) by Pogorelov et al. 2011. This code simulate coronal mass ejection (CME) events from 10 $R_\odot$ to 1 AU. Our lower coronal code will generate seed data and define boundary conditions at 10 $R_\odot$. Then MK-FLUKSS will use this seed data as initial input and extrapolate it to 10 $R_\odot$ to simulate CME propagation through interplanetary space. This integrated approach will allow us to track the evolution of CMEs from their origins in the lower corona to their potential impact on Earth. We'll be able to study how lower coronal MFRs evolve into interplanetary CMEs (ICMEs) and influence space weather.

Data constrained simulation for lower coronal model

In previous projects, we used analytical flux ropes and ambient field structures. In this workplan, however, we are more focused on using actual magnetic field data from the Sun. We differentiate between data-constrained and data-driven approaches by not directly inputting the actual magnetogram into the simulation. Instead, we use parameters derived from the actual magnetogram, such as twist and decay index, and incorporate these into our code. The twist is calculated using the nonlinear force-free field (NLFFF) method (Wiegelmann, 2008), while the decay index is derived from the potential field source surface (PFSS) model (Wang & Sheeley, 1992) using data prior to the eruption. We can then use different field strength as well as foot point distance of the arcade to mimic the actual decay index as seen by the PFSS model. Although this approach makes it challenging to accurately replicate real scenarios, it sheds light on how a simple model can reproduce physics similar to data-driven simulations without excessive complexity.

References

Afanasyev A. N., Fan Y., Kazachenko M. D., Cheung M. C. M., 2023, *Astrophys. J.* , 952, 136

Amari T., Luciani J. F., Mikic Z., Linker J., 2000, *Astrophys. J. Lett.* , 529, L49

Amari T., Luciani J. F., Aly J. J., Mikic Z., Linker J., 2003, *Astrophys. J.* , 585, 1073

Andrews M. D., 2003, *Solar Phys.* , 218, 261

Antiochos S. K., DeVore C. R., Klimchuk J. A., 1999, *Astrophys. J.* , 510, 485

Archontis V., Hood A. W., 2008, *Astrophys. J. Lett.* , 674, L113

Archontis V., Hood A. W., Savcheva A., Golub L., Deluca E., 2009, *Astrophys. J.* , 691, 1276

Aschwanden M. J., 2004, Physics of the Solar Corona. An Introduction

Attrill G. D. R., Harra L. K., van Driel-Gesztelyi L., Wills-Davey M. J., 2010, *Solar Phys.* , 264, 119

Aulanier G., 2014, in Schmieder B., Malherbe J.-M., Wu S. T., eds, Vol. 300, Nature of Prominences and their Role in Space Weather. pp 184–196 (arXiv:1309.7329), doi:10.1017/S1743921313010958

Aulanier G., 2016, Nature Physics, 12, 998

Aulanier G., DeLuca E. E., Antiochos S. K., McMullen R. A., Golub L., 2000, *Astrophys. J.* , 540, 1126

Aulanier G., Pariat E., Démoulin P., 2005, *Astron. Astrophys.* , 444, 961

Aulanier G., Török T., Démoulin P., DeLuca E. E., 2010, *Astrophys. J.* , 708, 314

Bahcall J. N., Huebner W. F., Lubow S. H., Parker P. D., Ulrich R. K., 1982, Reviews of Modern Physics, 54, 767

Baker D. N., Daly E., Daglis I., Kappenman J. G., Panasyuk M., 2004, Space Weather, 2, S02004

Ballai I., Forgács-Dajka E., Marcu A., 2007, Astronomische Nachrichten, 328, 734

Barczynski K., Aulanier G., Masson S., Wheatland M. S., 2019, *Astrophys. J.* , 877, 67

Bateman G., 1978, MHD instabilities

Beck C., Bellot Rubio L. R., Schlichenmaier R., Sütterlin P., 2007, *Astron. Astrophys.* , 472, 607

Bein B. M., Berkebile-Stoiser S., Veronig A. M., Temmer M., Vršnak B., 2012, *Astrophys. J.* , 755, 44

Bemporad A., Mancuso S., 2010, *Astrophys. J.* , 720, 130

Benz A. O., 2008, Living Reviews in Solar Physics, 5, 1

Berger T. E., Title A. M., 2001, *Astrophys. J.* , 553, 449

Bethe H. A., 1939, Physical Review, 55, 103

Bian X., Jiang C., Feng X., Zuo P., Wang Y., 2022, *Astrophys. J. Lett.* , 925, L7

Biesecker D. A., Myers D. C., Thompson B. J., Hammer D. M., Vourlidas A., 2002, *Astrophys. J.* , 569, 1009

Borrero J. M., Tomczyk S., Kubo M., Socas-Navarro H., Schou J., Couvidat S., Bogart R., 2011, *Solar Phys.* , 273, 267

Braginskii S. I., 1965, Reviews of Plasma Physics, 1, 205

Brandenburg A., et al., 2020, arXiv e-prints, p. arXiv:2009.08231

Buneman O., 1964, Physics of Fluids, 7, S3

Burgess A., 1964, *Astrophys. J.* , 139, 776

Canfield R. C., Hudson H. S., McKenzie D. E., 1999, *Geophys. Res. Lett.* , 26, 627

Carmichael H., 1964, in , Vol. 50, NASA Special Publication. p. 451

Carroll B. W., Ostlie D. A., 1996, An Introduction to Modern Astrophysics

Castellanos Durán J. S., Kleint L., Calvo-Mozo B., 2018, *Astrophys. J.* , 852, 25

Chatterjee P., 2020, Geophysical and Astrophysical Fluid Dynamics, 114, 213

Chatterjee P., Fan Y., 2013, *Astrophys. J. Lett.* , 778, L8

Chatterjee P., Hansteen V., Carlsson M., 2016, *Phys. Rev. Lett.* , 116, 101101

Chen J., 1989, *Astrophys. J.* , 338, 453

Chen P. F., 2011, Living Reviews in Solar Physics, 8, 1

Chen J., 2017, Physics of Plasmas, 24, 090501

Chen P. F., Shibata K., 2000, *Astrophys. J.* , 545, 524

Chen H., Zhang J., Ma S., Yang S., Li L., Huang X., Xiao J., 2015, *Astrophys. J. Lett.* , 808, L24

Cheng C. Z., Ren Y., Choe G. S., Moon Y. J., 2003, *Astrophys. J.* , 596, 1341

Cheng X., Zhang J., Liu Y., Ding M. D., 2011, *Astrophys. J. Lett.* , 732, L25

Cheng X., Guo Y., Ding M., 2017, Science China Earth Sciences, 60, 1383

Ciaravella A., et al., 2000, *Astrophys. J.* , 529, 575

Cook J. W., Cheng C. C., Jacobs V. L., Antiochos S. K., 1989, *Astrophys. J.* , 338, 1176

DeVore C. R., Antiochos S. K., 2008, *Astrophys. J.* , 680, 740

Dedner A., Kemm F., Kröner D., Munz C. D., Schnitzer T., Wesenberg M., 2002, Journal of Computational Physics, 175, 645

Demastus H. L., Wagner W. J., Robinson R. D., 1973, *Solar Phys.* , 31, 449

Deng M., Welsch B. T., 2017, *Solar Phys.* , 292, 17

Dissauer K., Veronig A. M., Temmer M., Podladchikova T., Vanninathan K., 2018, *Astrophys. J.* , 863, 169

Domingo V., Fleck B., Poland A. I., 1995, *Solar Phys.* , 162, 1

Doschek G. A., Warren H. P., 2005, AGU Spring Meeting Abstracts,

Duan A., Jiang C., He W., Feng X., Zou P., Cui J., 2019, *Astrophys. J.* , 884, 73

Dun J., Kurokawa H., Ishii T. T., Liu Y., Zhang H., 2007, *Astrophys. J.* , 657, 577

Emslie A. G., et al., 2004, Journal of Geophysical Research (Space Physics), 109, A10104

Falconer D. A., Moore R. L., Gary G. A., 2002, *Astrophys. J.* , 569, 1016

Fan Y., 2001, *Astrophys. J. Lett.* , 554, L111

Fan Y., 2009, *Astrophys. J.* , 697, 1529

Fan Y., 2010, *Astrophys. J.* , 719, 728

Fan Y., 2012, *Astrophys. J.* , 758, 60

Fan Y., 2017, *Astrophys. J.* , 844, 26

Fan Y., Gibson S. E., 2007, *Astrophys. J.* , 668, 1232

Fisher R. R., Poland A. I., 1981, *Astrophys. J.* , 246, 1004

Fisher G. H., Bercik D. J., Welsch B. T., Hudson H. S., 2012, *Solar Phys.* , 277, 59

Fletcher L., Hudson H. S., 2008, *Astrophys. J.* , 675, 1645

Forbes T. G., 2000, *J. Geophys. Res.* , 105, 23153

Forbes T. G., Isenberg P. A., 1991, *Astrophys. J.* , 373, 294

Forbes T. G., Priest E. R., 1984, *Solar Phys.* , 94, 315

Forbes T. G., et al., 2006, *Space Sci. Rev.* , 123, 251

Gaizauskas V., 2008, *Astrophys. J.* , 686, 1432

Gibson S. E., Fan Y., 2006, Journal of Geophysical Research (Space Physics), 111, A12103

Gibson S. E., Low B. C., 2000, *J. Geophys. Res.* , 105, 18187

Gold T., Hoyle F., 1960, *Mon. Not. Roy. Astron. Soc.* , 120, 89

Gombosi T. I., Tóth G., De Zeeuw D. L., Hansen K. C., Kabin K., Powell K. G., 2002, Journal of Computational Physics, 177, 176

Gonzalez W. D., Tsurutani B. T., Clúa de Gonzalez A. L., 1999, *Space Sci. Rev.* , 88, 529

Gopalswamy N., 2004, in Poletto G., Suess S. T., eds, Astrophysics and Space Science Library Vol. 317, The Sun and the Heliosphere as an Integrated System. p. 201, doi:10.1007/978-1-4020-2831-9_8

Gopalswamy N., Shimojo M., Lu W., Yashiro S., Shibasaki K., Howard R. A., 2003, *Astrophys. J.* , 586, 562

Gopalswamy N., Yashiro S., Akiyama S., 2007, Journal of Geophysical Research (Space Physics), 112, A06112

Gopalswamy N., Akiyama S., Yashiro S., Michalek G., Lepping R. P., 2008, Journal of Atmospheric and Solar-Terrestrial Physics, 70, 245

Gopalswamy N., Yashiro S., Michalek G., Xie H., Mäkelä P., Vourlidas A., Howard R. A., 2010a, Sun and Geosphere, 5, 7

Gopalswamy N., Akiyama S., Yashiro S., Mäkelä P., 2010b, in Magnetic Coupling between the Interior and Atmosphere of the Sun. pp 289–307 (arXiv:0903.1087), doi:10.1007/978-3-642-02859-5_24

Gopalswamy N., Yashiro S., Akiyama S., Xie H., 2017, *Solar Phys.* , 292, 65

Gopalswamy N., Akiyama S., Yashiro S., Xie H., 2018, Journal of Atmospheric and Solar-Terrestrial Physics, 180, 35

Gosain S., 2012, *Astrophys. J.* , 749, 85

Gosling J. T., 1993, *J. Geophys. Res.* , 98, 18937

Gosling J. T., Hildner E., MacQueen R. M., Munro R. H., Poland A. I., Ross C. L., 1974, *J. Geophys. Res.* , 79, 4581

Gosling J. T., Hildner E., MacQueen R. M., Munro R. H., Poland A. I., Ross C. L., 1976, *Solar Phys.* , 48, 389

Green L. M., Török T., Vršnak B., Manchester W., Veronig A., 2018, *Space Sci. Rev.* , 214, 46

Harra L. K., Sterling A. C., 2001, *Astrophys. J. Lett.* , 561, L215

Harrison R. A., 1990, *Solar Phys.* , 126, 185

Harrison R. A., 2003, Advances in Space Research, 32, 2425

Hewish A., Scott P. F., Wills D., 1964, *Nature* , 203, 1214

Hildner E., Gosling J. T., MacQueen R. M., Munro R. H., Poland A. I., Ross C. L., 1976, *Solar Phys.* , 48, 127

Hirayama T., 1974, *Solar Phys.* , 34, 323

Hirayama T., Nakagomi Y., 1974, *Pub. Astron. Soc. Japan* , 26, 53

Hood A. W., Priest E. R., 1979, *Solar Phys.* , 64, 303

Hood A. W., Priest E. R., 1981, Geophysical and Astrophysical Fluid Dynamics, 17, 297

Howard T., 2011, Coronal Mass Ejections: An Introduction. Vol. 376, doi:10.1007/978-1-4419-8789-1,

Howard R. A., Sheeley N. R. J., Michels D. J., Koomen M. J., 1985, *J. Geophys. Res.* , 90, 8173

Howard R. A., et al., 2008, *Space Sci. Rev.* , 136, 67

Howard T. A., DeForest C. E., Schneck U. G., Alden C. R., 2017, *Astrophys. J.* , 834, 86

Hoyng P., et al., 1981, *Astrophys. J. Lett.* , 246, L155

Hu Q., 2017, Science China Earth Sciences, 60, 1466

Hudson H. S., 1991, *Solar Phys.* , 133, 357

Hudson H. S., 2000, *Astrophys. J. Lett.* , 531, L75

Hudson H., Haisch B., Strong K. T., 1995, *J. Geophys. Res.* , 100, 3473

Hudson H. S., Lemen J. R., St. Cyr O. C., Sterling A. C., Webb D. F., 1998, *Geophys. Res. Lett.* , 25, 2481

Hudson H. S., Fisher G. H., Welsch B. T., 2008, in Howe R., Komm R. W., Balasubramaniam K. S., Petrie G. J. D., eds, Astronomical Society of the Pacific Conference Series Vol. 383, Subsurface and Atmospheric Influences on Solar Activity. p. 221

Hundhausen A. J., 1993, *J. Geophys. Res.* , 98, 13177

Hundhausen A., 1999, in Strong K. T., Saba J. L. R., Haisch B. M., Schmelz J. T., eds, The many faces of the sun: a summary of the results from NASA's Solar Maximum Mission.. p. 143

Hundhausen A. J., Burkepile J. T., St. Cyr O. C., 1994, *J. Geophys. Res.* , 99, 6543

Huttunen K. E. J., Schwenn R., Bothmer V., Koskinen H. E. J., 2005, Annales Geophysicae, 23, 625

Illing R. M. E., Hundhausen A. J., 1985, *J. Geophys. Res.* , 90, 275

Isenberg P. A., Forbes T. G., 2007, *Astrophys. J.* , 670, 1453

Janvier M., Aulanier G., Démoulin P., 2015, *Solar Phys.* , 290, 3425

Jiang Y., Ji H., Wang H., Chen H., 2003, *Astrophys. J. Lett.* , 597, L161

Jing J., Liu C., Lee J., Ji H., Liu N., Xu Y., Wang H., 2018, *Astrophys. J.* , 864, 138

Kahler S., 1977, *Astrophys. J.* , 214, 891

Kaiser M. L., Kucera T. A., Davila J. M., St. Cyr O. C., Guhathakurta M., Christian E., 2008, *Space Sci. Rev.* , 136, 5

Kazachenko M. D., 2023, arXiv e-prints, p. arXiv:2310.02878

Kazachenko M. D., Lynch B. J., Welsch B. T., Sun X., 2017, *Astrophys. J.* , 845, 49

Kazachenko M. D., Albelo-Corchado M. F., Tamburri C. A., Welsch B. T., 2022, *Solar Phys.* , 297, 59

Kleint L., 2017, *Astrophys. J.* , 834, 26

Kliem B., Török T., 2006, *Phys. Rev. Lett.* , 96, 255002

Koomen M., Howard R., Hansen R., Hansen S., 1974, *Solar Phys.* , 34, 447

Kopp R. A., Pneuman G. W., 1976, *Solar Phys.* , 50, 85

Kopp R. A., Poletto G., 1986, in Marsden R. G., Fisk L. A., eds, Vol. 123, The Sun and the Heliosphere in Three Dimensions. p. 65, doi:10.1007/978-94-009-4612-5_8

Korsós M. B., Ludmány A., Erdélyi R., Baranyi T., 2015, *Astrophys. J. Lett.* , 802, L21

Korsós M. B., Chatterjee P., Erdélyi R., 2018, *Astrophys. J.* , 857, 103

Kumar H., Kumar B., 2020, *Mon. Not. Roy. Astron. Soc.* , 497, 976

Leibacher J. W., Noyes R. W., Toomre J., Ulrich R. K., 1985, Scientific American, 253, 48

Leighton R. B., Noyes R. W., Simon G. W., 1962, *Astrophys. J.* , 135, 474

Leka K. D., Barnes G., Crouch A., 2009, in Lites B., Cheung M., Magara T., Mariska J., Reeves K., eds, CS-Astron. Soc. Pacific, San Francisco Vol. 415, The Second Hinode Science Meeting: Beyond Discovery-Toward Understanding. p. 365

Lemen J. R., et al., 2012, *Solar Phys.* , 275, 17

Li Y., Lynch B. J., Welsch B. T., Stenborg G. A., Luhmann J. G., Fisher G. H., Liu Y., Nightingale R. W., 2010, *Solar Phys.* , 264, 149

Li Y., Jing J., Fan Y., Wang H., 2011, *Astrophys. J. Lett.* , 727, L19

Lin J., Forbes T., 2000, Journal of Geophysical Research: Space Physics, 105, 2375

Lin J., Raymond J. C., van Ballegooijen A. A., 2004, *Astrophys. J.* , 602, 422

Liu R., 2020, Research in Astronomy and Astrophysics, 20, 165

Liu L., Zhou Z., Wang Y., Sun X., Wang G., 2022, *Astrophys. J. Lett.* , 934, L33

Livi S. H. B., Martin S., Wang H., Ai G., 1989, *Solar Phys.* , 121, 197

Low B. C., 1981, *Astrophys. J.* , 251, 352

Lynch B. J., Antiochos S. K., MacNeice P. J., Zurbuchen T. H., Fisk L. A., 2004, *Astrophys. J.* , 617, 589

Lynch B. J., Antiochos S. K., DeVore C. R., Luhmann J. G., Zurbuchen T. H., 2008, *Astrophys. J.* , 683, 1192

Lyot B., 1939, *Mon. Not. Roy. Astron. Soc.* , 99, 580

Magara T., 2004, *Astrophys. J.* , 605, 480

Mandrini C. H., Nakwacki M. S., Attrill G., van Driel-Gesztelyi L., Démoulin P., Dasso S., Elliott H., 2007, *Solar Phys.* , 244, 25

Martin S. F., 1998, *Solar Phys.* , 182, 107

Martin S. F., Livi S. H. B., Wang J., 1985, Australian Journal of Physics, 38, 929

Martínez-Sykora J., Hansteen V., Carlsson M., 2008, *Astrophys. J.* , 679, 871

Martínez-Sykora J., Hansteen V., Pontieu B. D., Carlsson M., 2009, *Astrophys. J.* , 701, 1569

Metcalf T. R., 1994, *Solar Phys.* , 155, 235

Michalek G., Yashiro S., 2013, Advances in Space Research, 52, 521

Mitalas R., Sills K. R., 1992, *Astrophys. J.* , 401, 759

Moore R. L., Roumeliotis G., 1992, in Svestka Z., Jackson B. V., Machado M. E., eds, , Vol. 399, IAU Colloq. 133: Eruptive Solar Flares. p. 69, doi:10.1007/3-540-55246-4_79

Moore R. L., Sterling A. C., Hudson H. S., Lemen J. R., 2001, *Astrophys. J.* , 552, 833

Munro R. H., Gosling J. T., Hildner E., MacQueen R. M., Poland A. I., Ross C. L., 1979, *Solar Phys.* , 61, 201

Myers C. E., Yamada M., Ji H., Yoo J., Fox W., Jara-Almonte J., Savcheva A., Deluca E. E., 2015, *Nature* , 528, 526

Nitta N. V., Hudson H. S., 2001, *Geophys. Res. Lett.* , 28, 3801

Nordlund Å., Stein R. F., Asplund M., 2009, Living Reviews in Solar Physics, 6, 2

Orta J. A., Huerta M. A., Boynton G. C., 2003, *Astrophys. J.* , 596, 646

Pal S., Nandy D., Srivastava N., Gopalswamy N., Panda S., 2018, *Astrophys. J.* , 865, 4

Parker E. N., 1958, *Astrophys. J.* , 128, 664

Patsourakos S., Vourlidas A., Stenborg G., 2013, *Astrophys. J.* , 764, 125

Patsourakos S., et al., 2020, *Space Sci. Rev.* , 216, 131

Pencil Code Collaboration et al., 2021, The Journal of Open Source Software, 6, 2807

Pereira T. M. D., et al., 2014, *Astrophys. J. Lett.* , 792, L15

Pesnell W. D., Thompson B. J., Chamberlin P. C., 2012, *Solar Phys.* , 275, 3

Petrie G. J. D., 2012, *Astrophys. J.* , 759, 50

Petrie G. J. D., 2019, *Astrophysical Journal Supplement Series*, 240, 11

Petrie G. J. D., Sudol J. J., 2010, *Astrophys. J.* , 724, 1218

Petschek H. E., 1958, Reviews of Modern Physics, 30, 966

Plunkett S. P., Thompson B. J., Howard R. A., Michels D. J., St. Cyr O. C., Tappin S. J., Schwenn R., Lamy P. L., 1998, *Geophys. Res. Lett.* , 25, 2477

Pogorelov N. V., Borovikov S. N., Heerikhuisen J., Kim T., Kryukov I. A., Zank G. P., 2011, in Pogorelov N. V., Audit E., Zank G. P., eds, Astronomical Society of the Pacific Conference Series Vol. 444, 5th International Conference of Numerical Modeling of Space Plasma Flows (ASTRONUM 2010). p. 130

Powell K. G., 1994, Approximate Riemann solver for magnetohydrodynamics (that works in more than one dimension)

Priest E., 2014, Magnetohydrodynamics of the Sun, doi:10.1017/CBO9781139020732.

Priest E. R., Forbes T. G., 2002, *Astron. Astrophys. Rev.* , 10, 313

Pulkkinen T., 2007, Living Reviews in Solar Physics, 4, 1

Qiu J., Yurchyshyn V. B., 2005, *Astrophys. J. Lett.* , 634, L121

Qiu J., Wang H., Cheng C. Z., Gary D. E., 2004, *Astrophys. J.* , 604, 900

Rachmeler L. A., Gibson S. E., Dove J. B., DeVore C. R., Fan Y., 2013, *Solar Phys.* , 288, 617

Ranns N. D. R., Harra L. K., Matthews S. A., Culhane J. L., 2000, *Astron. Astrophys.* , 360, 1163

Rast M. P., 2003, *Astrophys. J.* , 597, 1200

Reep J. W., Toriumi S., 2017, *Astrophys. J.* , 851, 4

Régnier S., Canfield R. C., 2006, *Astron. Astrophys.* , 451, 319

Reinard A. A., Biesecker D. A., 2008, *Astrophys. J.* , 674, 576

Rempel M., 2016, *Astrophys. J.* , 834, 10

Rieutord M., Rincon F., 2010, Living Reviews in Solar Physics, 7, 2

Romano P., et al., 2015, *Astron. Astrophys.* , 582, A55

Romano P., Elmhamdi A., Falco M., Costa P., Kordi A. S., Al-Trabulsy H. A., Al-Shammari R. M., 2018, *Astrophys. J. Lett.* , 852, L10

Rust D. M., Hildner E., 1976, *Solar Phys.* , 48, 381

Rust D. M., Kumar A., 1996, *Astrophys. J. Lett.* , 464, L199

Rutten R. J., Kostik R. I., 1982, *Astron. Astrophys.* , 115, 104

Sakurai T., 1976, *Pub. Astron. Soc. Japan* , 28, 177

Sammis I., Tang F., Zirin H., 2000, *Astrophys. J.* , 540, 583

Sarkar R., Srivastava N., 2018, *Solar Phys.* , 293, 16

Sarkar R., Srivastava N., Veronig A. M., 2019, The Astrophysical Journal Letters, 885, L17

Savcheva A., Pariat E., van Ballegooijen A., Aulanier G., DeLuca E., 2012, *Astrophys. J.* , 750, 15

Schmahl E. J., 1979, in Jensen E., Maltby P., Orrall F. Q., eds, IAU Colloq. 44: Physics of Solar Prominences. pp 102–120

Schmieder B., Démoulin P., Aulanier G., 2013, Advances in Space Research, 51, 1967

Schou J., et al., 2012, *Solar Phys.* , 275, 229

Schwenn R., 2006, Living Reviews in Solar Physics, 3, 2

Sheeley N. R. J., Howard R. A., Koomen M. J., Michels D. J., 1983, *Astrophys. J.* , 272, 349

Shibata K., Magara T., 2011, Living Reviews in Solar Physics, 8, 6

Shibata K., Masuda S., Shimojo M., Hara H., Yokoyama T., Tsuneta S., Kosugi T., Ogawara Y., 1995, *Astrophys. J. Lett.* , 451, L83

Sinha S., Srivastava N., Nandy D., 2019, *Astrophys. J.* , 880, 84

Siscoe G., 2000, Journal of Atmospheric and Solar-Terrestrial Physics, 62, 1223

Solanki S. K., 2003, *Astron. Astrophys. Rev.* , 11, 153

Solanki S. K., Stenflo J. O., 1984, *Astron. Astrophys.* , 140, 185

Spitzer L., 1962, Physics of Fully Ionized Gases

Srivastava N., Venkatakrishnan P., 2002, *Geophys. Res. Lett.* , 29, 1287

St. Cyr O. C., et al., 2000, *J. Geophys. Res.* , 105, 18169

Sterling A. C., Moore R. L., 2001, *J. Geophys. Res.* , 106, 25227

Sterling A. C., Hudson H. S., Thompson B. J., Zarro D. M., 2000, *Astrophys. J.* , 532, 628

Sturrock P. A., 1966, *Nature* , 211, 695

Subramanian P., Dere K. P., 2001, *Astrophys. J.* , 561, 372

Sudol J. J., Harvey J. W., 2005, *Astrophys. J.* , 635, 647

Sui L., Holman G. D., 2003, *Astrophys. J. Lett.* , 596, L251

Sun X., Hoeksema J. T., Liu Y., Wiegelmann T., Hayashi K., Chen Q., Thalmann J., 2012, *Astrophys. J.* , 748, 77

Sun X., et al., 2015, *Astrophys. J. Lett.* , 804, L28

Sun X., Hoeksema J. T., Liu Y., Kazachenko M., Chen R., 2017, *Astrophys. J.* , 839, 67

Thompson B. J., Plunkett S. P., Gurman J. B., Newmark J. S., St. Cyr O. C., Michels D. J., 1998, *Geophys. Res. Lett.* , 25, 2465

Thompson B. J., et al., 1999, *Astrophys. J. Lett.* , 517, L151

Thompson B. J., Reynolds B., Aurass H., Gopalswamy N., Gurman J. B., Hudson H. S., Martin S. F., St. Cyr O. C., 2000, *Solar Phys.* , 193, 161

Thompson W. T., et al., 2003, in Keil S. L., Avakyan S. V., eds, Society of Photo-Optical Instrumentation Engineers (SPIE) Conference Series Vol. 4853, Innovative Telescopes and Instrumentation for Solar Astrophysics. pp 1–11, doi:10.1117/12.460267

Titov V. S., 2007, *Astrophys. J.* , 660, 863

Titov V. S., Démoulin P., 1999, *Astron. Astrophys.* , 351, 707

Toriumi S., Wang H., 2019, Living Reviews in Solar Physics, 16, 3

Toriumi S., Schrijver C. J., Harra L. K., Hudson H., Nagashima K., 2017, *Astrophys. J.* , 834, 56

Török T., Kliem B., 2003, *Astron. Astrophys.* , 406, 1043

Török T., Kliem B., Titov V. S., 2004, *Astron. Astrophys.* , 413, L27

Tousey R., et al., 1973, *Solar Phys.* , 33, 265

Tousey R., Howard R. A., Koomen M. J., 1974, in Bulletin of the American Astronomical Society. p. 295

Tripathi D., Bothmer V., Cremades H., 2004, *Astron. Astrophys.* , 422, 337

Tsurutani B. T., Gonzalez W. D., Tang F., Akasofu S. I., Smith E. J., 1988, *J. Geophys. Res.* , 93, 8519

Turmon M., Jones H. P., Malanushenko O. V., Pap J. M., 2010a, *Solar Phys.* , 262, 277

Turmon M., Jones H. P., Malanushenko O. V., Pap J. M., 2010b, *Solar Phys.* , 262, 277

Ulrich R. K., 1970, *Astrophys. J.* , 162, 993

Vaiana G. S., Krieger A. S., Timothy A. F., 1973, Solar Physics, 32, 81

Vasantharaju N., Vemareddy P., Ravindra B., Doddamani V. H., 2022, *Astrophys. J.* , 927, 86

Vlasov V. I., 1981, Geomagnetism and Aeronomy, 21, 441

Vourlidas A., Lynch B. J., Howard R. A., Li Y., 2013, *Solar Phys.* , 284, 179

Waldmeier M., 1970, *Solar Phys.* , 15, 167

Wang H., 2006, *Astrophys. J.* , 649, 490

Wang H., Liu C., 2015, Research in Astronomy and Astrophysics, 15, 145

Wang Y. M., Muglach K., 2007, *Astrophys. J.* , 666, 1284

Wang Y. M., Sheeley N. R. J., 1992, *Astrophys. J.* , 392, 310

Wang S., Liu C., Liu R., Deng N., Liu Y., Wang H., 2012a, *Astrophys. J. Lett.* , 745, L17

Wang S., Liu C., Wang H., 2012b, *Astrophys. J. Lett.* , 757, L5

Wang Y., Zhuang B., Hu Q., Liu R., Shen C., Chi Y., 2016, Journal of Geophysical Research (Space Physics), 121, 9316

Warnecke J., Bingert S., 2020, Geophysical and Astrophysical Fluid Dynamics, 114, 261

Webb D. F., 2002, in Wilson A., ed., ESA Special Publication Vol. 508, From Solar Min to Max: Half a Solar Cycle with SOHO. pp 409–419

Webb D. F., Howard R. A., 1994, *J. Geophys. Res.* , 99, 4201

Webb D. F., Howard T. A., 2012, Living Reviews in Solar Physics, 9, 3

Wheatland M. S., Melrose D. B., Mastrano A., 2018, *Astrophys. J.* , 864, 159

Wiegelmann T., 2008, Journal of Geophysical Research (Space Physics), 113, A03S02

Wiegelmann T., Thalmann J. K., Solanki S. K., 2014, *Astron. Astrophys. Rev.* , 22, 78

Williamson J. H., 1980, Journal of Computational Physics, 35, 48

Withbroe G. L., Noyes R. W., 1977, *Ann. Rev. of Astron. Astrophys.*, 15, 363

Wöger F., Rimmele T., Ferayorni A., Beard A., Gregory B. S., Sekulic P., Hegwer S. L., 2021, *Solar Phys.* , 296, 145

Woods T. N., et al., 2012, *Solar Phys.* , 275, 115

Wuelser J.-P., et al., 2004, in Fineschi S., Gummin M. A., eds, Society of Photo-Optical Instrumentation Engineers (SPIE) Conference Series Vol. 5171, Telescopes and Instrumentation for Solar Astrophysics. pp 111–122, doi:10.1117/12.506877

Wyper P. F., Antiochos S. K., DeVore C. R., 2017, *Nature* , 544, 452

Xu Z., Yang K., Guo Y., Zhao J., Zhao Z. J., Kashapova L., 2017, *Astrophys. J.* , 851, 30

Yadav R., Kazachenko M. D., 2023, *Astrophys. J.* , 944, 215

Yang Y.-H., Hsieh M.-S., Yu H.-S., Chen P. F., 2017, *Astrophys. J.* , 834, 150

Yashiro S., Gopalswamy N., 2009, in Gopalswamy N., Webb D. F., eds, Vol. 257, Universal Heliophysical Processes. pp 233–243, doi:10.1017/S1743921309029342

Yashiro S., Gopalswamy N., Michalek G., St. Cyr O. C., Plunkett S. P., Rich N. B., Howard R. A., 2004, Journal of Geophysical Research (Space Physics), 109, A07105

Yashiro S., Gopalswamy N., Akiyama S., Michalek G., Howard R. A., 2005, Journal of Geophysical Research (Space Physics), 110, A12S05

Youssef M., 2012, NRIAG Journal of Astronomy and Geophysics, 1, 172

Yurchyshyn V., Yashiro S., Abramenko V., Wang H., Gopalswamy N., 2005, *Astrophys. J.* , 619, 599

Zel'dovich Y. B., Raizer Y. P., 1967, Physics of shock waves and high-temperature hydrodynamic phenomena

Zhang J., Wang J., 2002, *Astrophys. J. Lett.* , 566, L117

Zhang J., Dere K. P., Howard R. A., Kundu M. R., White S. M., 2001, *Astrophys. J.* , 559, 452

Zhang Y., Liu J., Zhang H., 2008, *Solar Phys.* , 247, 39

Zhu C., Qiu J., Liewer P., Vourlidas A., Spiegel M., Hu Q., 2020, *Astrophys. J.* , 893, 141

Zhukov A. N., Auchère F., 2004, *Astron. Astrophys.* , 427, 705

Zirin H., 1988, Astrophysics of the sun

Zirin H., Liggett M. A., 1987, *Solar Phys.* , 113, 267

van Ballegooijen A. A., Martens P. C. H., 1989, *Astrophys. J.* , 343, 971